5-2013

New Effects of Aging and Lattice Intercalation on Surface Properties of Titanate Nanobelts

Roger Williams
University of Arkansas, Fayetteville

New Effects of Aging and Lattice Intercalation on Surface Properties of Titanate Nanobelts

New Effects of Aging and Lattice Intercalation on Surface Properties of Titanate Nanobelts

A dissertation submitted in partial fulfillment
of the requirement for the degree of
Doctor of Philosophy in Chemistry

By

Roger Williams
Bachelor of Science in Biochemistry, 2008
Eastern New Mexico University

May 2013
University of Arkansas

ABSTRACT

Titanate nanobelts (NBs) have structural characteristics beyond that of clays. Due to a negatively charged lattice matrix of edge-shared TiO_6-octahedra, the location of intercalated cations within the interlayer space may dictate the charge-conductions. This environment may in turn govern the lattice-framework's stability and surface properties, based upon our preliminary data.

On that basis, these nanomaterials have been found in our lab to possess superb biological compatibility that is closely related to the types of the intercalated cations. In addition, a prolonged agitation was proven to enable us to manipulate the titanate NBs' length. In a parallel study, a ripening was observed in the post-synthesis aging process at room temperature (RT). This process implied, for the first time, a new way of changing the NBs' aspect ratio in nanosynthesis.

This novel post-synthesis manipulation of aspect ratio has enabled us to successfully improve our yield of the NB-membrane by four folds, which is significant in scale-up fabrication of the NB-entangled membranes, which have shown interest as a proton exchange membrane (PEM) in fuel cells (PEMFC) and gas sensing capabilities.

PEMFCs provide the highest power density in comparison with all other fuel cell types currently available. In order to improve the fuel cells efficiency, further advancements into enhancing the thermal stability while maintaining adequate hydration levels of the PEM membrane is continually sought after. Unfortunately, the polymer structure of Nafion© membranes structural stability and water retention falls short at elevated temperatures. However,

based on our preliminary data, intercalated titanate NBs/Nafion© composites may hold the key to overcoming these technological drawbacks.

Lastly, aging and surface modification of titanate materials has been used to attain the high selectivity and sensitivity in electrochemical sensing when applied to an electrode surface. Our initial findings suggest that the intercalated titanate NBs is ideal for use on an interdigitated electrode surface for direct sensing of relative humidity at different percentages.

This dissertation is approved for recommendation
to the Graduate Council.

Dissertation Director:

_____
Dr. Z. Ryan Tian

Dissertation Committee:

_____
Dr. Neil Allison

_____
Dr. Dan Davis

_____
Dr. Bill Durham

DISSERTATION DUPLICATION RELEASE

I hereby authorize the University of Arkansas Libraries to duplicate this dissertation when needed for research and/or scholarship.

Agreed _____
Roger Williams

Refused _____
Roger Williams

ACKNOWLEDGEMENTS

First and foremost, I would like to thank my wife, Leah. I cannot express how much I would be lost without her love, guidance, and endless patience in my life. Thank you very much for putting up with me.

To my mom, I greatly appreciate all the sacrifices you have made to make me the man I am today. You are one of the greatest role models in my life. To the rest of my family and friends, I am grateful for all the aid in keeping me tethered in the "real" world.

To my PhD advisor, Dr. Z. Ryan Tian, I truly appreciate your ever-present support, guidance, and mentorship through my years here at the University of Arkansas.

To all my committee members, Dr. Neil Allison, Dr. Dan Davis, and Dr. Bill Durham, thank you for always having an open door policy if I needed further guidance on a project I was working on.

To all my past and present group members and collaborators, I cannot express how much I valued all your help. To Dr. Andrew Zhou, thanks for always lending a helping hand whenever I needed one. To Subbu, I really appreciated all your advice and guidance on the gas sensing work. Victoria Haines and Dr. Daniel Fologea, I am very grateful for your all your hard work on the prelim ion conductivity study. I am much obliged to Tom Cannon for his continued help with the fuel cell membrane project.

To the graduate school support staff, Leslie Johnson, thank you for always having a sympathetic ear for all those constant headaches (both literal and figurative) the past 5 years have given me. To Dr. Bob Gawley, without your help and guidance during (and especially after) the

undergrad research project, I would not have even considered entering into graduate school in the first place.

I am very thankful for the goading (fmr) A1C Philip "Duke" Hazard gave me into a having a "CLEP" race with him. Which surprisingly enough enabled me to finish the Community College of the Air Force degree in less than two months. Without his push, I wouldn't have been earmarked by the upper echelons and transferred into a different command wing whose efforts towards furthering my own education wouldn't have been possible.

To all of the leadership personnel of Detachment 9 of AETC Command Wing of Cannon Air Force Base, I really appreciated not only allowing me extra personal time to further my education, but also bestowing me with the skills to be an effective listener, communicator, and instructor.

To my undergraduate advisor, Dr. Juchao Yan, you inspired me to continue my research efforts in graduate school of which I am ever grateful. To Dr. Robert Long, thanks for teaching me to appreciate the "puzzle qualities" chemistry had to offer. To Dr. Manuel Varela, your "Journal Club" analytical eye has become an invaluable tool in my graduate studies that I will carry with me always.

Last but not least, I humbly appreciate the efforts of my iPod for bringing me Chris Hardwick, Matt Mira, and Jonah Ray of the "Nerdist" podcast, Kumail Nanjiani and Emily V. Gordon of the "Indoor Kids" podcast, the countless hours of audio books, and Netflix Instant Streaming. Thanks for keeping me: awake, company, entertained, and (most importantly) sane during the many long nights and weekends or graduate school has bestowed me.

TABLE OF CONTENTS

LIST OF FIGURES

LIST OF TABLES

LIST OF ABBREVIATIONS

0D	Zero-Dimensional
1D	One-Dimensional
2D	Two-Dimensional
C	Ionic Concentrations
CdSe	Cadmium Selenide
CHEMFET	Chemically Sensitive Field-Effect Transistors
CNT	Carbon Nanotube
CNTs	Carbon Nanotubes
Cu	Copper
d	Interplanar Spacing
D	Distance
D	Diffusion Coefficient
dc/dx	Concentration Gradient
DDW	Distilled Deionized Water
E	Potential Difference
EDX	Energy-dispersive X-ray Spectroscopy
ELISA	Enzyme-Linked Immunosorbent Assay
F	Faraday's Constant
FESEM	Field Emission Scanning Electron Microscopy
HEPES	4-(2-Hydroxyethyl)-1-Piperazineethanesulfonic Acid
i	Current
IDE	Interdigitated Electrode
IEC	Ion Exchange Capacity
IS	Impedance Spectroscopy
Kα	Copper Emitted Radiation
LSV	Linear Sweep Voltammetry
MO	Metal Oxide
MWNT	Multi Walled Nanotube
MWNTs	Multi Walled Nanotubes
n	Interger
NB	Nanobelt
NBs	Nanobelts
NP	Nanoparticle
NPs	Nanoparticles
PEM	Proton Exchange Membrane
PEMFC	Proton Exchange Membrane Fuel Cell
PEMFCs	Proton Exchange Membrane Fuel Cells
PEMs	Proton Exchange Membranes
QD	Quantum Dot
QDs	Quantum Dots

R	Universal Gas Constant
RH	Relative Humidity
SEM	Scanning Electron Microscopy
SWNT	Single Walled Nanotube
SWNTs	Single Walled Nanotubes
T	Temperature
TEM	Transmission Electron Microscopy
TGA	Thermogravimetric Analysis
TiO_2	Titanium Dioxide
V	Voltage
V_m	Transmembrane Voltage
Wt%	Weight Percent
$WU_{(\%)}$	Water Uptake
XRD	X-ray Diffraction
Γ^{lV}	Liquid/Surface Free Energy
Γ^{sl}	Solid /Liquid Free Energy
Γ^{sV}	Solid Surface Free Energy
ΔA	Change in Cross sectional Area
Δt	Change in Time
θ	Diffraction Angle
λ	Wavelength

CHAPTER 1

INTRODUCTION

1.1. Why Go "Nano"?

Ever since the discovery of carbon nanotubes by Iijima in 1991, nanomaterials have become the forefront of innovation in science and technology[1-8]. In particular, new technologies have been shifting toward the miniaturizing of devices through the use of nanomaterials [7, 8]. One of the main reasons for this technological push towards the "nano" realm is largely because materials at this length scale offer a larger surface-to-volume ratio. Hence, nanomaterials possess maximized surface areas and in turn surface reactivity, making them ideal for use in the fields of sensors[3, 4, 7, 8] and catalysis.[9, 10] In comparison with the bulk counterpart, nanomaterials can widely varying primary properties e.g. color, magnetization[10], flexibility[11], melting point[12, 14], and thermal stability.[15]

1.2. Nanomaterials' Overview

Nanomaterials are typically composed of ceramics, metals, and composites. These materials are classified into three primary morphological types:

(i) Zero Dimensional (0D) – e.g. semiconductive nanocrystals (also called quantum dots, or QDs), clusters, etc.

(ii) One Dimensional (1D) – e.g. nanotubes, nanorods, nanobelts, nanowires, etc.

(iii) Two Dimensional (2D) – e.g. nanofilms, nanosheets, nanoplatelets, etc.

1.2.1. Zero Dimensional Nanoparticles (0D-NPs)

This is the simplest type among the above three, with diameters less than 100 nm. Two fascinating aspects of size dependency arise from the utilization of the 0D NPs: quantum effects[13], highly reactive surface, and low melting points.[14]

Semiconductive nanocrystals in the 0D form, also called quantum dots or QDs, possess quantized energy levels that similar to that of electrons in an atom. To date, research in this field has confirmed that this quantization characteristic is dependent upon the NP's size. In essence, as the size of QDs decreases, the quantum effect increases[13], which can be clearly observed in the absorption spectra of cadmium selenide (CdSe) QDs. For example, the maxima in the absorbtion band of CdSe shift to a higher energy as the size of the QD is reduced; therby, creating a tunable band gap.[13] In addition, 0D-NPs in general show an intriguing difference in melting point when compared to the bulk. For instance, utilizing a range of tin nanoparticles (26 to 85 nm in diameter) and a differential scanning calorimeter, Jiang et al observed that decreasing particle size also decreases the melting point.[14]

1.2.2. One Dimensional (1D)

Commonly, 1D nanostructures have diameters similar to that of the 0D NPs; however, lengths can be greater than one micron. In contrast to the bulk counterpart, 1D nanomaterials are usually imbued with superior mechanical properties, e.g. tensile strength and flexibility. For example, people have employed carbon-based 1D nanomaterials as a substrate in the creation of printable batteries.[11] In addition, 1D nanomaterials can be stable at high temperatures. For example, researchers at the Virginia Commonwealth University have reported the utilization of 1D zinc oxide nanobelts to improve thermal stability of gold and platinum catalysts[15], which implies an unusual potential for the 1D-nanomaterials in catalysis.

1.2.3. Two Dimensional (2D)

Most recently, promising work done by Cornell University has shown that by utilizing a template via colloidal suspension, a single layer of CdSe can be made.[17] Though this process was focused on CdSe, further research into adapting this work into other single layer 2D nanosheets (e.g. graphene) may soon be within our reach.

Noteworthy researchers at the Max-Planck-Institute fur Polymerforshung reported an unusually high receptive electronic mobility on 2D graphene sheets.[16] On this basis, they postulated that this functionality alone would allow this 2D nanomaterial to act as an excellent current collector. In this way, the high mobility may allow for a faster diffusion of ions, making the graphene sheet a perfect ion-conductor for improving rechargeable battery.[16] However the high cost and the low yield in mass production jeopardizes this technology's translation to the industrial application in a near future.

1.3. Pros and Cons in Top Down and Botton Up Nanofabrications

Nowadays, nanomaterials can be fabricated via two fundamentally different methodologies: top down and bottom up. The top down method involves the break-down of the bulk materials into the minute size through mechanical means (e.g. cutting[18], milling, and layer-by-layer coating). The bottom-up route (e.g. molecular[19, 20], colloidal[21], or polymer chemistries[22]) fabricates nanomaterials using single atoms or molecules. Currently, engineering efforts in top down nanofabrication rely on photo- and electron-lithography and laser ablation in order to create the same materials under the size restrictions.[18]

There exist some longstanding problems in bottom up nanofabrication of, for instance, 0D-NPs. During the fabrication of 0D-NPs, researchers have observed that the NPs can

randomly aggregate, making the discrete NPs too expensive to be mass-produced in an industrial scale.[13, 19] By taking the advantage of the nano-aggregation on the other hand, materials scientists are developing new self-assembly[24] methodologies to fulfill the nanofabrication. Self-assemblies based on both static and chemical forces are spontaneous processes in which ordered patterns or aggregates form from chaotically scattered components without the need of any extra outside control, besides the help of template and entropy-minimization principle. Due to the huge promise in materials science, this particular protocol has attracted much attention lately. Pioneering research in self-assembly by Whitesides' group postulates that the self-assembly crystallization is highly doable from nm- to mm-scales [24]. Therefore, it's widely believed that the self-assembly can quickly shift paradigm in fabrication of microelectronic devices[25] in the near future.

Some 1D nanomaterials that are truly translational to industrial and clinical applications, such as titanate nanobelts (NBs) [26], have been seldom studied in the basic synthetic chemistry for enabling a scalable production at low-cost. In order to determine how best to translate these novel properties into meeting some long-unmet challenges in basic materials chemistry, a systematic study on the syntheses, chemical composition, crystal lattice, surface chemistry and applications of a well-defined 1D-nanomaterial system should be important and encouraged.

1.4. The Demand for Nontoxic and Low-cost 1D Nanomaterials

1D nanomaterials are expected to greatly advance a wide myriad of important applications, ranging from energy conversion and storage (e.g. lithium-ion batteries[27], solar cells[28], and photocatalytic applications[29]) to medical diagnosis and therapeutics [30-33]. However, the promise of these materials should never overshadow the detriment from usage. Considerably

high cost, for instance, comes from the challenges of scale-up fabrication not to mention the financial burden for cleaning them up if they are hazardous to our health and carelessly discharged into our environment.[35]

1.4.1. Concerns and Reduction of 1D Nanomaterials' Toxicity

The growing concern of 1D nanomaterials' toxicity stemmed from possession of similarities to carcinogenic asbestos micro fibers in morphology and biopersistence. However, unlike asbestos micro fibers, 1D nanomaterials may have a greater toxicity. The potentially increased toxicity is due to the inherent cellular entry mechanism. By having a minimal structural dimensionality, 1D nanomaterials are allowed to penetrate animal cell walls directly without the necessity of endocytosis. Once crossing the cell membrane, they start to disrupt the organelle functionality within the cell. Through this cellular perturbation, the interred nanomaterials may cause severe tissue inflammation, abnormal cell functions including abnormal apoptosis.

For example, studies of lung pathologies from animals with prolonged exposure of 1D carbon-nanotubes (CNTs) have shown a significant interstitial penetration of the CNT in the inflammatory cells, causing emphysema and several types of alveolar exudation.[34] However, extensive studies indicated that a simple surface functionalization can reduce the inherent toxicity of the 1D nanomaterials, making them practically useful in biomedical science. For instance, surface functionalized CNTs have been proven to be able to enhance the efficacy of a drug-delivery.[37]

1.4.2. Unmet Challenges in Economical Farbrication of 1D Nanomaterials

Some 1D nanomaterials, e.g. CNTs[34-37], require not only sophisticated equipment in synthesis but also costly processes in purification, in order to yield an industry-viable product

with a precisely targeted property or functionality. Thus, a suitable candidate is a necessity to fully understand the effects of 1D-nanomaterial's synthesis chemistry on chemical composition, lattice structure, surface properties, and future applications. An extensive literature survey suggests that titanate1D nanomaterials can be such an ideal candidate.

1.5. 1D Titanate Nanomaterials

1.5.1. The Clay-like Layered Lattice Structure of Titanate

The discovery of photocatalytic water-splitting on powdery titanium dioxide (TiO_2), by Fujishima and Honda in 1972[38], has catalyzed the development of new photocatalysts[39-41], large band gap semiconductors[42], and sensors.[43] The use of TiO_2 in these applications is due to the excellent photooxidation power and chemical inertness. The past few years have witnessed a considerable growth of number in the publications on new syntheses, surface modifications, and applications of TiO_2-based nanomaterials that are ultra-low in toxicity and cost but extremely high in surface-to-volume ratio and chemical stability.

As an increasingly visible member in the family of TiO_2-based nanomaterials, the titanate-based nanostructures' unique lattice structure has been extensively examined.[44-50] Based on crystallographic data from scanning electron microscopy (SEM), transmission electron microscopy (TEM), and X-ray diffraction (XRD) studies, the lattice structure of the titanate consists of clay-like layers, each as a negatively charged matrix made of edge- and corner-shared TiO_6-octahedra. In between every two adjacent layers, there sits a layer of counter cations (e.g. H^+, or Na^+, etc) in order to keep the neutrality in charge throughout the entire lattice. The layered titanate lattice structure is simply depicted in the Figure 1.1.

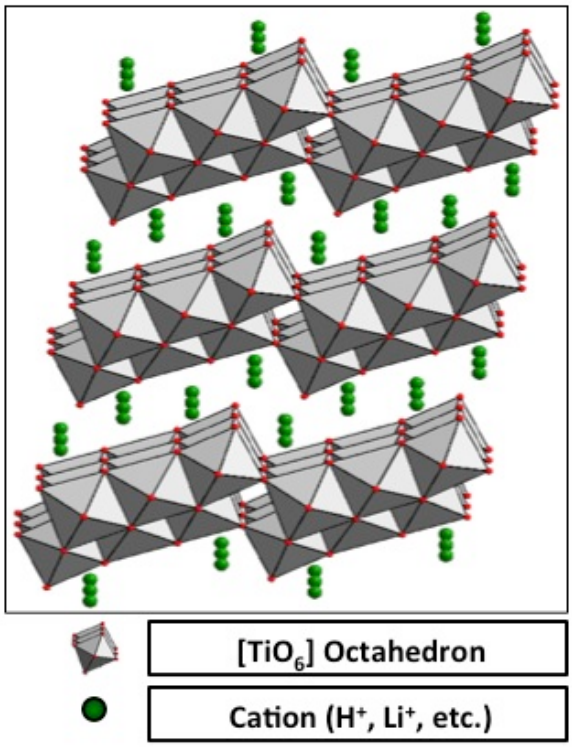

Figure 1.1: Layered Matrix of Titanate Nanomaterials

1.5.2. Synthesis of Titanate Nanomaterials

The development of a successful bottom-up nanofabrication relies heavily on an effective control over not only the reproducible growth but also the minimized agglomeration of the nanomaterials. In order to address these issues, methods for fabricating 1D titania-based nanomaterials have been studied through the use of sol-gel templates[51-52], emulsion[53], and solvothermal processes[54]. One setback in these nanofabrications arises from the longstanding challenge of effective removal of the most (if not all) impurities (including unreacted species) from the growth media. In addition, many of these fabrication methods rarely yield high crystallinity and uniform morphologies for the 1D nanomaterials. Often, a further calcination at an elevated temperature is adapted, in order to improve the crystallinity and morphological purity. However, the extra heating causes unwanted changes in the lattice, surface, size, and aggregation of these nanomaterials.

To facilitate a better control over the size of 1D titania-based nanomaterials, electrospinning techniques have been developed alternatively. This method is often combined with sol-gel processing in order to fabricate various forms of nanofibers. [55] The electrospinning set-up consists of a high voltage power source, a needle tip spout, and collector. The titania suspension (containing a polymer resin as the binder) is loaded into a syringe. The feed-rate output is under computer control in order to maintain electro-spun fibers with uniform diameter. When a high voltage is applied to the needle, the titania is extruded from the needle in an electrified form. The oppositely charged electrostatic force on the collector directs the flow of the extruded materials, forming a nonwoven mat. The pH of the titania suspension (much like a sol-gel) can alter the resulting diameter of the 1D nanomaterial. [55]

Usually, this electrospinning technique yields impure forms of 1D nanomaterial, not to mention the built-in drawback of slow processing. The mat-like composites from the electrospinning have the physical and chemical properties that vary depending on the polymer binder's content. In order to obtain a consistent control of the overall crystallinity and phase purity of the 1D nanomaterial, other synthetic methods were actively sought out. The most commonly used fabrication method is the 'one-pot" alkaline hydrothermal synthesis. Utilizing this technique, the control over the large-scale morphological uniformity can be reproducibly achieved .[56]

In the "one-pot" synthesis, raw titanium dioxide (TiO_2) powder is first mixed with a water solution of high alkalinity (10 M sodium hydroxide). The mixture is placed in a pressurized digestion bomb that is then sealed and heated. The "one-pot" hydrothermal synthesis involves simultaneously (i) the dissolution of the TiO_2 in the sodium hydroxide (i.e. NaOH), (ii) combining the TiO_6-octahedra with the counter-cations such as Na^+ to form the sodium titanate

layered lattice, and (iii) the growth of the single-crystalline 1D titanate nanostructures (e.g. nanotubes, nanobelts, etc).

The final morphology (i.e. length and width) of the 1D nanostructure of titanate is fine-tunable, depending on not only the hydrothermal reaction's time and temperature (e.g. < 150°C) but also the loading and size of the reaction vessel. For instance, heating at a lower temperature (e.g. > 160°C) can result in titanate nanotube; while at a higher temperature only non-hollow 1D nanostructures (e.g. nanorods, nanowires, nanobelts) can be formed. Such new knowledge naturally calls for a further systematic study for understanding the effect of systematic intercalation (i.e. ion exchange) of different interlayer counter-cations on the lattice, surface, and properties and applications of the titanate 1D nanomaterials.[57-61]

1.5.3. Intercalation of 1D Titanate Nanomaterials: Advantages & New Challenges

The intercalation of 1D titanate nanomaterials is the process in which a cation in between the interlayer space is replaced by another one in solution without affecting the lattice's type. In order to timely complete the ion exchange, a constant agitation and heating are usually applied, which is easily maintained in an open-container like a beaker[61] but may be hard to accomplish with a sealed pressurized vessel.[61] Topologically, the intercalation for the 1D titanate nanotubes is slow due to the limited accessibility for the cations in solution to the interlayer cations deep inside the nanobelt's lattice matrix (as depicted in figure 1.2).

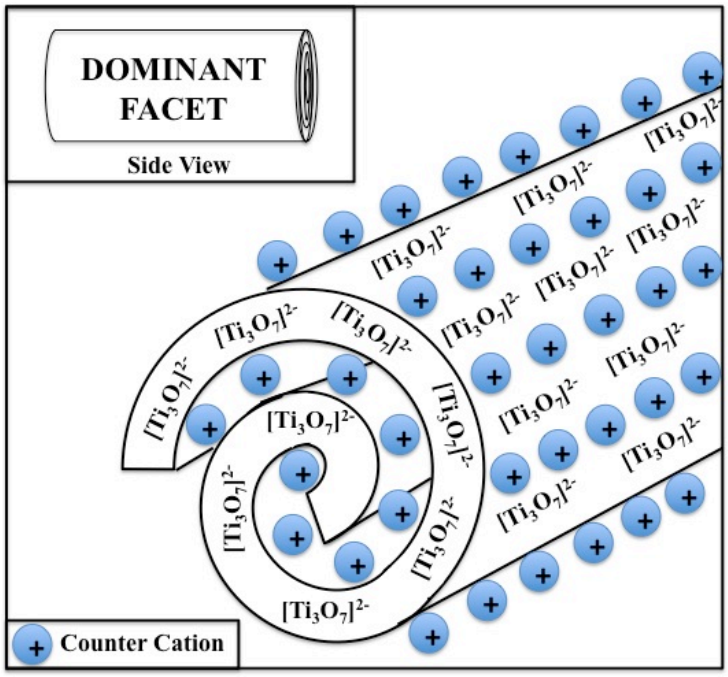

Figure 1.2: Titanate Nanotube Schematic

As depicted in figure 1.2, the titanate nanotube has a sheet-fold edge along the longitudinal axis by which ion exchange primarily happens. The ion exchange of the host cations residing within the tube's lattice matrix requires extra time and energy.

Hence, quenching the intercalation process prematurely should result in a significantly reduced ion-exchange.[62] Whereas, prolonging the ion exchange process can destabilize the nanotube's structure[63] due to penetration through the tube's multilayers, resulting in defects on the nanotube surface. When the concentration of the defects increases along the longitudinal surface and in turn the mechanical strains, the aspect ratio of the 1D nanotube is reduced.

It has been recently reported by Margez et al that increased surface defects increases the bio-toxicity of 1D titanate nanomaterials.[64] As the number of defects increases, the reactive sites on the longitudinal surface increases, thereby promoting the toxicity of the nanomaterial. On the other hand, the increased defects should be highly helpful in surface charge-conduction and catalysis. As a result, the cation exchange should behave differently for a differently structured

titanate nanomaterials (e.g. nanobelts), which was seldom reported in literature in especially a systematic manner.

1.6. 1D Titanate Nanobelts (NBs): Unique Structure, Synthesis, and Intercalation

1.6.1. Widely Tunable Structures and Properties

Titanate NBs ($Na_{2n-2}H_nTi_3O_7$) have attracted a great attention owing possessing unique properties including a large surface area[65], excellent chemical stability[66], catalytic properties[66], and ability for ion exchange.[61-67] Titanate NBs is regarded as an ideal replacement for CNTs due to the reduced toxicity to biological systems, ease and low-cost of synthesis, high thermal stability[66], biocompatibility[68, 69], and the high sensitivity in sensor applications. As depicted in the simplified lattice structure of figure 1.3, titanate NB structure possesses two distinct and comparable facet surfaces, which is different than the nanotube form.

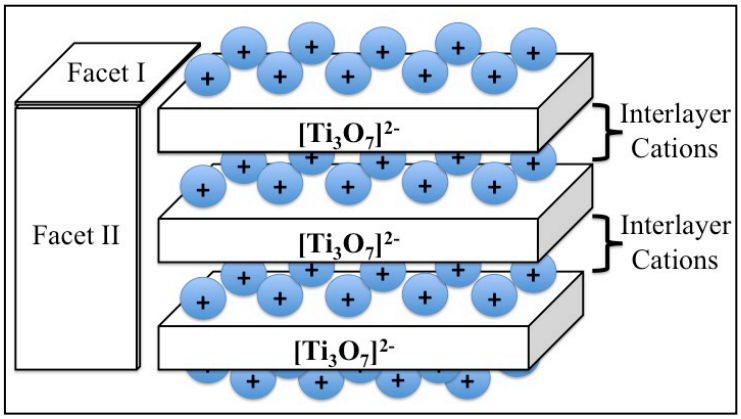

Figure 1.3: Titanate Nanobelts (NBs) Lattice Matrix Schematic

1.6.2. Facile Synthesis and Unique Aging

Small-scale synthesis of the titanate NBs has been studied extensively.[61-69] Most production protocols follow a more-or-less similar procedure described in the Section 1.5.2. The main distinction is the temperature and time at which the autoclave treatment takes place (e.g. 240 °C and 72 hours). Contrarily, large-scale synthesis has been much less reported. In fact,

only small amounts of the titanium dioxide were translated into the NB form in the typical small-scale synthesis, leaving significant amounts of unreacted material wasted. This fact prompted us to explore the role of room-temperature (RT) aging for the raw product.

It has been observed that the titanate nanotube formation may continue to grow in an extremely basic medium[70-72]. This is because the hydrothermal treatment converts TiO2 into titanate solute in the highly basic aqueous solution of 10M NaOH, under the elevated temperature and pressure. The dissolved titanate, each as an octahedron [TiO_6], may further crystalize after being cooled to RT and allowed to age over the time. In this end, the role of the dissolution of the nanocrystallites and that of the crystallization of the dissolved titanate in the 10M NaOH were seldom discussed in literature, especially in the nanosynthesis of 1D nanomaterials.

1.6.3. Unique Intercalation

As shown in figure 1.3, the two dominant facets belonging to the NB structure allow for fast ion-exchange especially under a constant agitation (e.g. stirring, sonication, etc.). The ionic radii, hydration capability, and locality of the interlayer counter-cations are what largely dictate the entire lattice's properties such as charge-conduction.[72]

Because the basic unit of the edge-shared TiO_6-octahedron is negatively charged, the interlayer space may accommodate cations in different sizes and oxidation-states (e.g. H^+, Na^+, Ca^{2+}, etc). [73-76] Thus, the cation-exchange through the Facet-2 should be slower and more energy-taking than that on the Facet-1, although each is tunable by varying the time, temperature, and concentration of the intercalating cations in the solution. Further, the NB interlayer space can be "tuned" to a wide range of specific values, based on the ionic radii of the intercalating guest-cation's dehydrated and hydrated forms. As a result, the intercalation of the NB structure may

yield a tunable conductivity, an improved mechanical strength, and a reduced toxicity due to the decreased amount of surface defects.

1.6.4. Importance in Basic & Applied Nanosciences

1D nanostructures have become a focus in the nanoresearch for a decade.[23-33] Amongst all the 1D nanostructures being studied to date, the titanate NBs with the low toxicity, ease of synthesis, and high temperature stability should deserve more attention. In particular, further investigations into the post-synthetic ripening may help retain the NBs' aspect ratio during the intercalation processes. Thus-tuned thermal stability, charge-conduction and catalysis of the titanate NBs should enable us to tackle some longstanding problems in, for instance, fuel cells and gas sensing.

1.7. Important Potential Applications of Titanate NBs. Part I: Fuel Cells

According to the Department of Transportation[77], there were 244,778,179 automobiles registered in the United States in 2012. As CO_2 emissions and oil prices continue to rise, powering automobiles using clean and renewable energy sources has been increasingly demanded over the past few decades.[78, 79] A vehicle's internal combustion engine lies at the core of the problem, and a suitable power replacement is required to assuage the economic and reduction of pollution challenges of our county. Fuel cells are regarded as a potential solution to solving this problem, due to the inherent energy-efficiency and minimal pollution to the environment.

Amongst all types of fuel-cells, research efforts made by the Department of Energy has been in the field of hydrogen fuel cells.[78] Hydrogen-based fuel cells are ideal, because the two by-products from electrical conversion is only heat and water. The potential of fuel cells in high-

power use may largely change the landscape of energy-related science, technology, and policy for our country by drastically reducing the greenhouse gases and smog-type of air pollutants. Although there are no true moving parts within the fuel cell to create energy, it does have several unmet challenges in, for instance, improving the overall cell efficiency.

1.7.1. Proton Exchange Membrane Fuel Cell (PEMFC) Operation[79]

The operation and the function of a PEMFC's units are schematically depicted in figure 1.4.

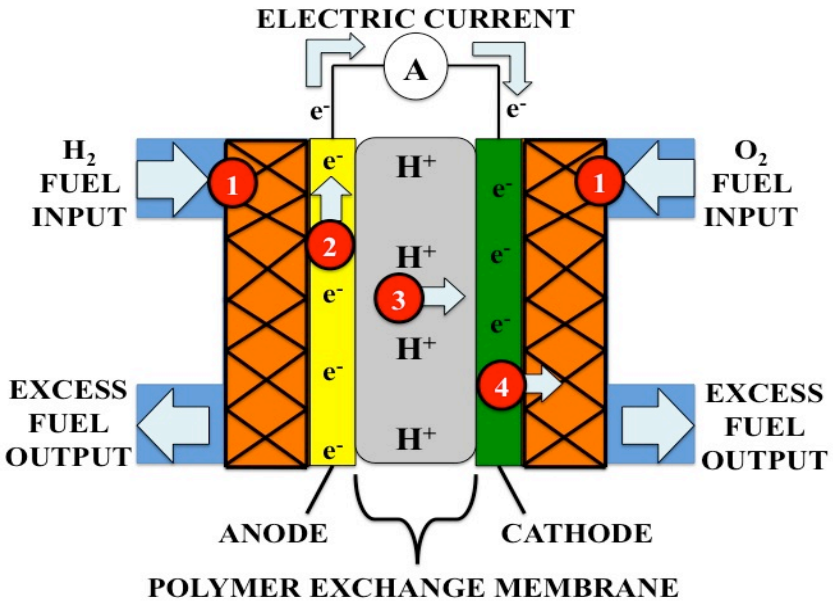

Figure 1.4: Proton Exchange Membrane Fuel Cell (PEMFC) Schematic Diagram

(1) Pure hydrogen gas as fuel is introduced to the anode through the input chamber valve. Any unreacted hydrogen gas is cycled through the exit valve. As this continues, the oxidant (e.g. oxygen gas) is pumped into the cathodic side of the cell. Both gases are diffused through a gas diffusion matrix to be in contact with electrode surfaces.

(2) Once the hydrogen gas reaches the anode, a catalyst (normally platinum based[78]) causes the hydrogen gas to spit into hydrogen ions (e.g. H^+) and electrons. The electrons go via an external circuit to generate a current for the cell.

A net reaction at the anode: $H_2 \rightarrow 2H^+ + 2e^-$

(3) The polymer exchange membrane (PEM) enables the passage of the protons only to the cathodic side of the cell.

(4) The electrons pass through the load circuit while at the same time the protons diffuse across the PEM, both then arriving at the cathode. They then react with the input oxidizer and the cathodic surface, forming water (e.g. H_2O) that immediately thereafter flows out of the fuel cell assembly with any unreacted oxygen gas.

At the cathode: $½ O_2 + 2H^+ + 2e^- \rightarrow H_2O$

Overall reaction: $H_2 + ½ O_2 \rightarrow H_2O$

1.7.2. Polymer Exchange Membrane (PEM)

- **1.7.2.1. PEM Functional Responsibilities**

At the core of each such PEMFC stack resides a polymer exchange membrane (PEM). The PEM has three key functions: (1) Facilitating the transport of protons to the cathodic side of the cell while maintaining sufficient hydration.[80-82] (2) Blocking the passage of electrons and any gas and water crossover.[83-85] (3) Support the PEMFC's functioning in the harsh operating thermal environment.[80, 86-88]

- **1.7.2.2. Nafion© Structure**

Commercially, only one polymer exchange membrane (PEM) contender currently available is the Nafion©. The Nafion© structure, as depicted in figure 1.5, consists of a copolymer with dispersed terminating sulfonated tetrafluorethylene linkages.

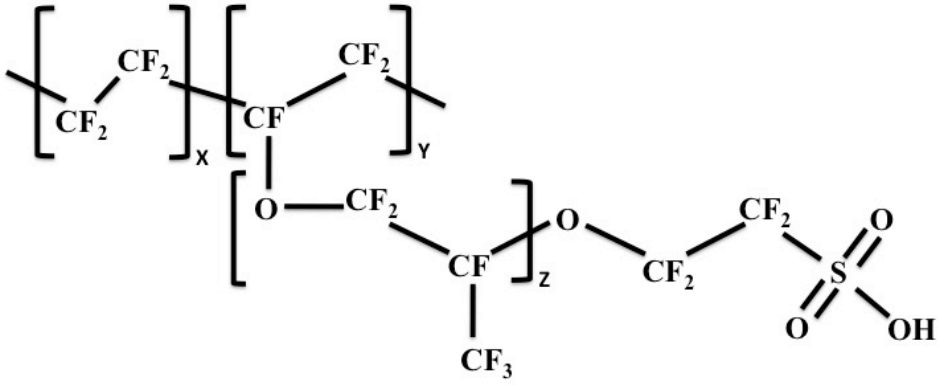

Figure 1.5: Protanated Nafion© Structure

The fluorinates on the PEM polymer's backbone offers a great tensile-strength and resistance to the harsh redox environments, while the sulfonic group uses the prontanated moiety to offer a sufficient ionic conductivity. However, the concentration of the interspaced sulfonic groups along the PEM polymeric backbone is relative low, since too many of such functional groups can reduce the overall mechanical stability of the membrane.[89]

Chemically, Nafion© polymer consists of both hydrophobic and hydrophilic moieties.[80, 83, 87-89] The hydrophobicity comes from the tetrafluoroethylene backbone; whereas, the hydrophilicity is a result of the sulfonic acid group's widely and reversibly chargeable hydration level. Largely, these sulfonic groups in the polymer matrix resemble an inverse micelle. The ionic conduction across the membrane is closely associated with a sufficient water uptake.

- **1.7.2.3. Nafion© Ion Conductivity Model**

To date, much of the chemistry research into the sulfonic groups seems to support the proton-conduction model developed originally by Hsu and Gierke.[90, 91] According to this charge-transfer mechanism (see figure 1.6), a proton travels through the polymer matrix via the "hopping" mechanism through the protonating sulfonate substituents that are adjacent to each other.

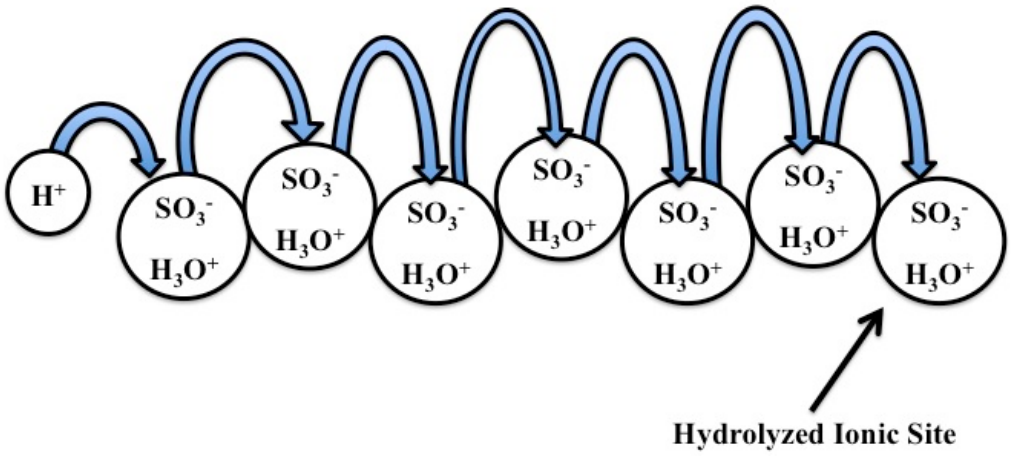

Figure 1.6: The Schematic of A Proton's "Hopping"

In Hsu's and Gierke's reports, the typical spacing in between the sulfonate/sulfonic acid groups is approximately 5.0 nm, based on XRD analyses.[90, 91] This interval can shrink or expand, dependent upon the hydration level. When fully hydrated, the gap is reduced, increasing the proton conductivity. Unfortunately, when the hydration level is improperly maintained, two key issues emerge. (1) The overall mechanical strength of the matrix is drastically reduced, due to cracks from an over-dehydration.[81, 89, 92] (2) A significant water-crossover the PEM from an over-hydration, which floods the electrode.[82, 89]

Often, the balancing in hydration is complicated by the temperature restriction. A high hydrothermal stability is essential to PEMs, because the highly exothermic reaction of water formation ($2H_2 + O_2 \rightarrow 2H_2O$) is constantly occurring within the fuel cell.[79,87] When the PEMs' environment reaches temperature levels greater than approximately 95°C, a severe dissociation of the sulfonic groups occurs.[87,89] This leads to (i) the PEM's degradation and (ii) the proton conductivity's reduction, which concludes the most common causes of the PEM destruction from the poor water-management and thermal overload. Thus, in the development of a PEMFC with the required durability and lifespan, it has been a grand challenge to make a quality PEM that can possess a proper hydration level and a high thermal stability.

- **1.7.2.4. Unmet Challenges of Nafion© Membranes**

Unfortunately, Nafion©'s thermal limitations have stymied advances in developing efficient PEMs for years.[79-91] In parallel, enormous efforts have been put on increasing the cell's power efficiency through improving catalysis at the electrode surface. For example, investigations into imbuing Nafion© surface with platinum/carbon form of catalyst by Wilson and Gottesfeld has proven useful. In doing so, they optimized the catalytic properties using the PEM as the support matrix.[93] Furthermore, this work showed not only that fabrication of Nafion© composites were possible, but also filler material may imbue much needed alterations to properties inherent to Nafion©.

Unfortunately, instead of systematically addressing these issues in parallel, many groups have tried to put their efforts in a single limitation alone. Of these, Costamagna's group at Princeton University has found how to improve the thermal stability of catalyst particles of zirconium phosphate.[94] Their group reported that using either commercial grade N115 or the casted form of Nafion©, an impregnation of the zirconium phosphate has slightly improved the PEMFC's performance at an elevated temperatures (1500 mA/cm^2 in 130°C).[94] In comparison with the commercial grade Nafion© under the same thermal condition, the performance improvements were only slight (1000 mA/cm^2)[94].

However, Costamanga reported a maximum load of 23-wt% of filler into the PEM polymer, without causing the severe membrane degradation and increased gas crossover. The higher the load, the higher the thermal stability, but the poorer the water retention and the proton-conductivity.[94] In compositing the filler into the polymer, how to remove the solvent before annealing the composite was found to be critical.

For improving the PEM's thermal stability, other researchers has tried to manage the hydration level, using inorganic metal oxides as fillers in Nafion© composite membranes.[95, 96] For example, Antonucci's group reported a success in making the Nafion© composite membrane by controlling a silica-filler's hygroscopicity.[95] In parallel, Watanabe's group reported similar results, by emphasizing silica's role in retaining a higher level of water in the polymer medium.[96]

Not until recently, the low load filler composites have never reached the maximal nano-blending within the polymer matrix. Due to this lack of homogeneity, the resultant PEMs' thermal stability has not been markedly improved. However, using the montomorillonite (a clay, with ion-exchangeable parallel sheets of silicate tetrahedra[97, 100]) as the filler, Felice's group developed new Nafion© composite membranes that finally address the homogeneity issue. Felice et al reports an improved thermal stability, a balanced hydration-level,[97-99] and a reduced hydrogen fuel crossover.[98] However, Felice et al also demonstrated the composites possessed a poor ionic conductivity when compared to the pure Nafion© polymer due to a poor hydration within the nanocomposite matrix.[98]

Thereafter, a research performed by Beauger et al has shown that sepiolite may be a real contender.[101] Sepiolite clay was chosen owing to two key features: (1) It possesses a distinct acicular (i.e. needle-like) form, which may help improve the mechanical strength of the membrane.[101] (2) It retains a hygroscopic feature that may address the lack of adequate water uptake in hydration which was commonly seen in using other clays. However, the discontinuity of layered sepiolite material was not helpful to conducting protons. To overcome this drawback, the surface hydroxyl groups were sulfonically functionalized based on Fernandez-Carretero's work,[102] through successive condensation reactions. Then, the sulfonated modified sepiolite (-SO_3Na) was ion-exchanged to form a protonated surface (-SO_3H), which is ideal to facilitate the

ion hopping transfer (see figure 1.6). Beauger et al's research revealed further that sepiolite's layered lattice were converted to nanochannels throughout the Nafion© matrix,[101] and the composite material imbued the Nafion© matrix with high thermal stability and durability under a low relative humidity.

Unfortunately, Beager et al's methodology may not be scalable. The disadvantages were three fold. First, the composite membrane fabrication possesses an overly complex functionalization protocol. Secondly, the final grinding procedure did not yield reproducible aspect ratios and did not reduce the gas-crossover sought after. Lastly, the composite membrane lowered the proton conductivity despite the surface functionalization.[101]

Surprisingly, recent investigations using inorganic oxides have shown that improving the thermal stability and hydration management may finally be well at hand. Under diminished levels of humidity, Nafion© composite membranes that employ titanium dioxide (i.e. TiO_2[103, 105]) and silicon dioxide (i.e. SiO_2[104]) as guest fillers have successfully withstood hostile thermal environments of PEMFCs. Furthermore, the use of these inorganic oxides has demonstrated the importance of homogeneity and interfacial properties. However, these bulk materials did not add a better mechanical strength to the composite membranes.

To this end, 1D titanate nanomaterials started to show a particular promise, as discussed previously in Beauger et al's work.[101] Lately, the research by Matos' group[106] has demonstrated that 1D titanate nanotubes have a distinct fabrication edge over clays in forming the Nafion© composites, based on Kasuga et al's[48] "one pot" synthesis. In that work, aspect ratios of the titanate 1D nanomaterials can be easily controlled and maintained throughout the process. Unfortunately, Matos's group attained the weight percentage of the load near 20%[106], resulting in an ion conductivity lower than that of the Nafion© but similar to that of Costamanga's.[94]

Although Mato's research has indicated that their composite membrane survived at high temperatures (e.g. 130°C), the unmet challenge of reduced ionic conduction was still present. They in addition reported that the 1D titanate nanotubes possess a limited interaction between Nafion© sulfonic maxtrix and the dominant surface facet (see figure 1.2).

In the scope of all the work published in literature to date, it has become apparent that new methodologies for making the composite PEM using new nanomaterials need to be developed. On that basis, it was proposed by this thesis research that the highly protonated titanate NBs may hold the promise to improving the PEM.

The 1D titanate NBs can be an ideal filler for Nafion© composite membrane, due to the reproducible synthesis (e.g. Kasuga et al[48]) and ease of ion-exchange (see the Section 1.6.). Furthermore, our lab's preliminary results implied that titanate NBs can be simply fabricated into Nafion© composite at loading levels vastly greater than the previously attained 20% (i.e. 50% to 200%, possibly); which demand a systematic exploration for this thesis work. Further study on improving the thermal stability, hydration control, and ionic conductivity of these protonated titanate nanobelt/Nafion© composites may yield new nanotechnologies highly viable to industry in the fuel cell sector.

1.8. Important Potential Applications of Titanate NBs. Part II: Gas Sensors

Surface and interfacial chemistry in the "nano" realm has become the research forefront in areas of detection, identification and quantification of biological and chemical species.[107-111] These new areas have been proven highly promising in especially developing industry-viable new methods and devices for early diagnosis of diseases, such as enzyme-linked immunosorbent assays (ELISA) [107,] chemically sensitive field-effect transistors (CHEMFET) [108, 109], and gas

sensors.[110, 111] Scientifically however, developing user-friendly gas-sensors has long faced tough challenges in controlling the mass-transport, surface adsorption/desorption, and signal transduction at the interface between the gaseous species and the sensory material's surface.[110, 111]

In order to evaluate these interfacial chemistry challenges, modeling for gases in response to equivalent circuits was then developed.[112, 113] Utilization of impedance spectroscopic techniques in sensing relative humidity (RH) was extensively studied,[112-115] to meet new needs in a variety of fields ranging from building smart houses[116] to biomedical industry.[117-119] Typically, RH is a measure of the percentage of water vapor's partial pressure in ambient air environment with respect to the water's saturated state.[112] RH sensors reflect that ratio through the detection of adsorbed water concentration condensed on the surface of a sensory material.

Many commercial RH sensors utilize an interdigitated electrode (IDE) array as the monitoring surface. The IDEs have been widely implemented in sensing devices, including surface acoustic wave detection[120] and capacitive sensing,[121] due to a rapid response in impedance spectroscopy (IS). The IS allows a representation of gas to solid interactivity through the use of equivalent circuits.[122] However, it has been a longstanding challenge to manipulate the interfacial properties on the IDE, often at the nanometer scale, while under the constraints of an IDE's minute substrate.

1.8.1. IDE Gas Sensor Structure

A general interdigitated electrode (IDE) array is shown in figure 1.7.

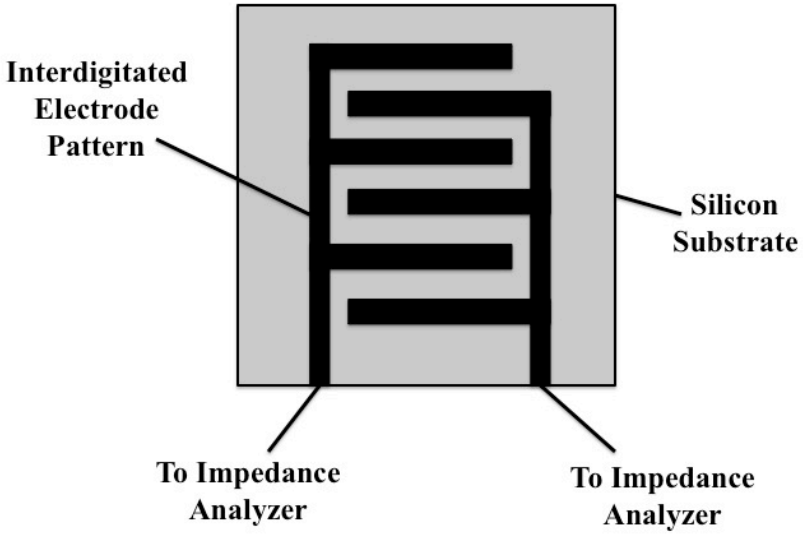

Figure 1.7: The Schematic of A Typical Planar Interdigitated Electrode (IDE) Array

The selection of the micropatterned interdigitated electrodes is very important to ensure a higher sensitivity and selectivity. Typically, the electrode materials (e.g. platinum[123], gold[124], carbon[125], etc) are deposited onto substrate surface through the use of photolithographic techniques.[126]

1.8.2. IDE: Operational Guidelines

The affects of the IDE have been widely studied in electrochemical chemistry.[126] Most are distinguished through electrostatic or charge transfer interactions. Interdigitation of these electrodes allows for sensitive quantification of redox reactions, usually. The typical IDE array responsive to the redox process is further depicted in figure 1.8.

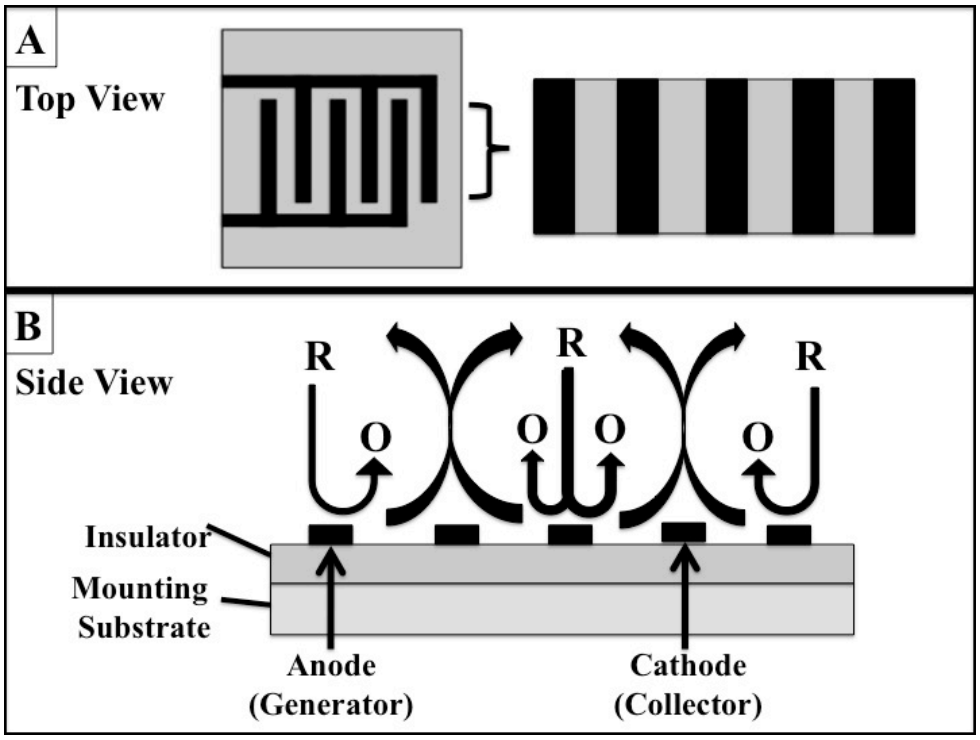

Figure 1.8: An Illustration of An IDE Array's Operation

In the Figure 1.8, "R" represents the reduced form which becomes oxidized to the "O" form at the generator (anodic plate), and then the "O" recycles to the "R" form at the cathodes. Each of the anodic and cathodic plates is alternating within the interdigitated array.

1.8.3. IDE RH Sensors: An Overview and Unmet Challenges

These array types used in RH determinations examine the interfacial interactions between the IDE electrode substrate and the concentration of the adsorbed water amount. The resistance continues to vary, as the content of water molecules increases (e.g. under higher levels of relative humidity or RH). Unfortunately, IDE-based amperometric humidity sensors have a low detection limit at higher RHs.[127-129] This is due to the electric field generated is not well confined on the electrode-surface's dielectric constant. As a fact, once the water is adsorbed on the IDE's planar surface, it produces an electrical shunt that decreases the detection limits as well as degrades the array's lifetime.[127] In order to tackle this issue, a suite of more resistive coatings

that have been examined include carbon nanotubes[130-133], inorganic oxides[134-139], and inorganic oxide 1D nanostructures.[140-143]

To this end, the research reported by Li's group[131] at NASA's Ames Research Center has demonstrated a dip-coating technique for homogeneously dispersing SWCNTs on an IDE array. This work has not only shed light on overcoming the contact resistance between nanomaterial and IDE surface, but also demonstrated the importance of interconnectivity and coating thickness to the sensor's sensitivity. In particular, Li's group photolithographically produced an IDE with a gap size around 8 μm.[131] Although the SWCNTs' length was not sufficient to cross the gap, the coating method did create a network mesh. This methodology reveals that employing a thicker coating did increase the IDE-fingers' interconnectivity; thereby, allowing efficient contact between the electrodes' surface thus increasing the sensitivity.[131,132] In addition, the increased interconnectivity helped tune the interfacial properties of the nanomaterial for meeting specific needs in sensing different gases. Although, carbon nanomaterials may not be ideal in humidity sensing in household due to the toxicity (see the Section 1.4.1) and cost (see the Section 1.4.2) concerns, the lessons learned from this study has implied the importance of using safer sensing materials, e.g. inorganic oxides.

In sub-nm scale, water-adsorption on an oxide surface should result in significant changes to the charge transfer properties on the oxide's surface.[134] The reaction mechanisms[134, 135] are summarized in Figure 1.9. (A) - (D).

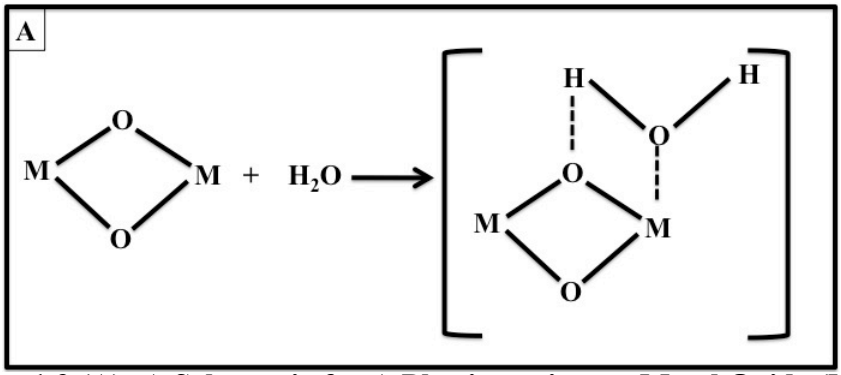

Figure 1.9 (A): A Schematic for A Physisorption on Metal Oxide (MO)

Figure 1.9 (A) depicts the physisorption of water molecules on the metal oxide (MO) surface forming the oxide complex through a hydrogen bonding.

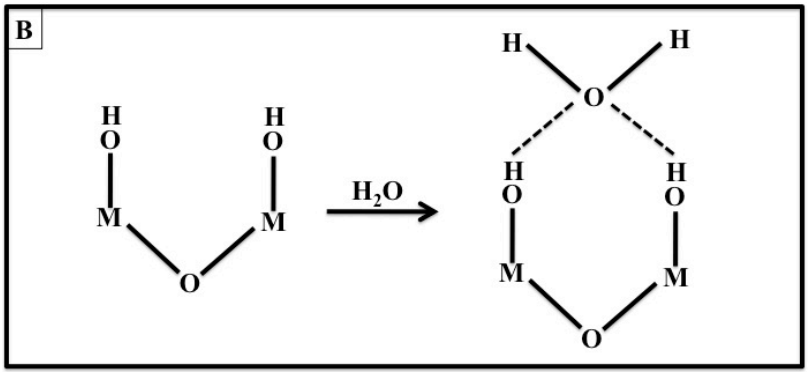

Figure 1.9 (B): A Schematic for A Complex on Metal Oxide (MO)

Figure 1.9 (B) shows the dissociative mechanism in which two resulting hydroxides are formed, and (C) depicts MO surface on the IDE.

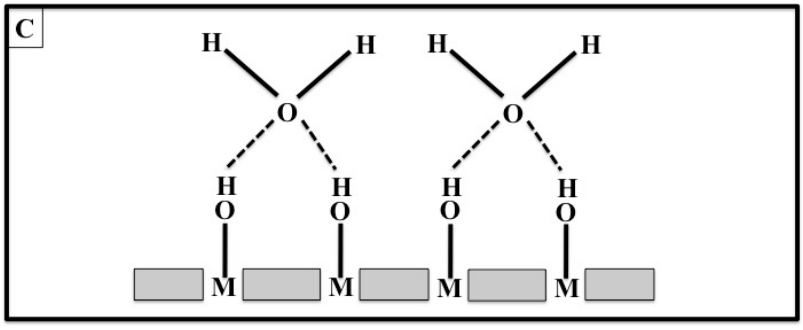

Figure 1.9 (C): A Schematic of Metal Oxide (MO) Surface

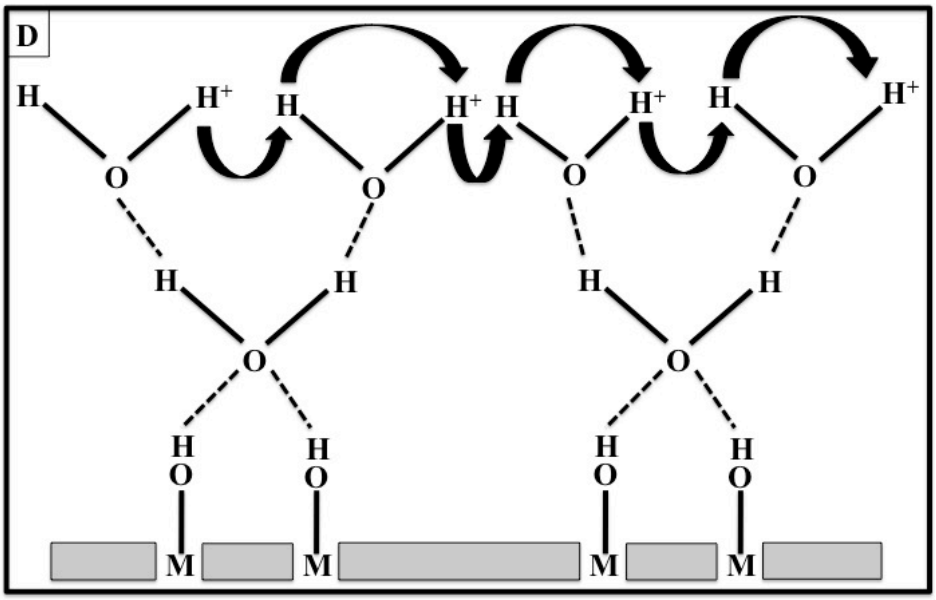

Figure 1.9 (D): Proton Conduction's Hopping Mechanism

Schematic 1.9 (D) illustrates that as water molecule concentrations increase (e.g. higher relative humidity), the proton reacts with the adjacent oxygen group to form a second hydroxyl group. Once the chemisorption water layer is formed, it is unaffected by the addition of more water molecules.

As the second adsorption layer forms, singly bonded water molecules instill the formation of dipole moments, thereby increasing the dielectric constant on the oxide material. In doing so, the protonic hopping (e.g. ion conduction) continues along the oxide surface. In essence, the passage of protons increases with humidity level. Thus, the direct interactivity between water and the metal oxides surface becomes ideal for sensing especially the high RHs.

In the rather complex RH sensing, several factors must be taken into consideration when choosing proper inorganic sensory materials. They first of all must possess controlled structure uniformity and porosity as well as surface active sites.[134] Examples include tin dioxide (SnO_2), molybdenum oxide (MoO_3), indium oxide (In_2O_3), and titanium dioxide (TiO_2) nanoparticles that are good in humidity sensing, with each possessing a desired crystallinity.[136-140] For example,

SnO_2 nanoparticles has been successfully made to have a morphological uniformity of around 20 nm from a flame-spray synthesis.[136] Among many types of oxide nanoparticles being tried,[136, 137] Liu's group has reported a synthetic success in making SnO_2 nanoparticles of 30 nm in diameter, via a chemical vapor deposition, to improve the gas sensitivities.[137]

In gas sensing, the necessity of a large active surface area has been confirmed in the cases of MoO_3[138], TiO_2[139-141], and In_2O_3.[141] Ultimately, high cost may become the determining factor in limiting the use of sensory 1D nanomaterials (e.g. barium titanate[142], tin oxide[143], and titanate form[144]).

As an alternative, electrospinning fabrication techniques (refer to the Section 1.5.2) have been rapidly developed in the application of barium titanate nanofibers[142] and tin oxide nanowires.[143] For instance, He's group reported a successful synthesis of a impedance-based humidity sensor using barium titanate nanofibers.[142] However, the electrospun nanofibers have two built-in drawbacks. The huge number of grain-boundaries (in between adjacent nanoparticles) across the entire length of the nanowire severely reduces charge conduction and the mechanical strength, not to mention the poor control over the structure and properties of the carbonaceous residue from the polymer resin, both of which in turn weakens the overall device sensitivity.

In hopes of optimizing the electrode-nanoparticle interface chemistry, promising work has been performed by Francisoso's group at the CNR-IMM Institute in Italy.[144] They reported a template synthetic regime in which well aligned single crystalline titanate nanowires grew directly onto the electrode surface via a template method. In order to maximize the direct interactivity, isotropic etching and further calcination requirements of 500°C were applied.[144] Unfortunately, template-directed nanogrowth yielded two core disadvantages: (1) The technique

did not yield enhanced sensitivities, due to that the limited length of the thus-formed nanowires did not sufficiently cross the gap (approximately 100 μm[144]) between the biased microelectrodes. (2) Ultra-violet photolithography is too complex and too expensive to be translated into large-scale production. Thus, if another inorganic oxide 1D nanostructure (e.g. titanate NBs) were used, a significant step forward in this field would be certainly within the reach.

Our group in the past made various forms of intercalated titanate NBs available and at low-cost. As discussed in the Section 1.6, the titanate NBs possess: a uniform higher crystalline via a simplistic regime (offered by Kasunga's group[48]), biocompatible, and tunable surface properties from intercalation.[57-61] Moreover, by mimicking Li's strategy to improve the interconnectivity in RH sensitivities,[131, 132] we designed and studied how to improve the reactivity on the NB surface. As the result, our preliminary data have all concluded that using a specified coating technique onto an IDE substrate provides an increased sensitivity to RH heralding the potential for a humidity sensor.

CHAPTER 2

METHODOLOGY

2.1. Materials

2.1.1. Reagents: Synthesis & Intercalation of Titanate NBs

The chemicals from Alfa Aesar include sodium hydroxide (NaOH, solid pellet form-CAS: 1310-73-2), sodium chloride (NaCl, solid form-CAS: 7647-14-5), strontium chloride hexahydrate ($SrCl_2*6H_2O$, solid form-CAS: 10025-70-4), and barium chloride dihydrate ($BaCl_2*2H_2O$, solid form-CAS: 10326-27-9). Those from EMD are hydrochloric acid (HCl, liquid form-CAS: 7647-01-0), potassium chloride (KCl, liquid form-CAS: 7447-40-7), and calcium chloride dihydrate ($CaCl_2*2H_2O$, solid form-CAS: 10035-04-8). The lithium chloride (LiCl) in solid form was from MP Biomedical, LLC (CAS: 7447-41-8), while magnesium chloride hexahydrate ($MgCl_2*6H_2O$) was purchased from Malinckrodt (CAS: 7791-18-6). Titanium dioxide (TiO_2) powder was purchased through Degussa (P25) (CAS: 13463-67-7). The P25 form indicates that particle size is approximately 25 nm in diameter, and contains both the anatase (80%) and rutile (20%) forms of titanium dioxide. All these compounds were used as received, without further purification.

2.1.2. Reagents: Titanate NBs Membrane Surface Functionalization

The chemicals were all purchased from Alfa Aesar. They are (3-chloropropyl) trimethoxysilane (CAS: 2530-87-2), isobutyltrimethoxysilane (CAS: 18395-30-7). In addition,

ethyl Alcohol (200 Proof absolute, anhydrous) was obtained from Pharmco-Aaper (CAS: 64-17-5). No further purification was performed with any of these compounds, before use.

2.1.3. Reagents: Nafion©/Intercalated Titanate NBs Composite

250 mL of Nafion® solution, DE102-10wt.%, was obtained from the Fuel Cell Store. Hydrogen peroxide (H_2O_2, CAS: 7722-84-1) in liquid form was acquired through Alfa Aesar. Sulfuric acid (H_2SO_4, CAS: 7664-93-9) in concentrated form was purchased through RICCA Chemical. No further purification was required.

2.1.4. Reagents: Relative Humidity Study

The following was purchased from Alfa Aesar in analytical grade: hydrochloric acid (HCl, liquid form-CAS: 7647-01-0), magnesium chloride hexahydrate ($MgCl_2*6H_2O$, CAS: 7791-18-6), magnesium nitrate hexahydrate ($Mg(NO_3)_2$, CAS: 13446-18-9), sodium chloride (NaCl, CAS: 7647-14-5), ammonium sulfate ($(NH_4)_2SO_2$, CAS: 7783-20-2), and potassium nitrate (KNO_3, CAS: 7757-79-1).

2.2. Set-ups for the NB-Synthesis

The magnetic stirring and low temperature heating was accomplished via a VWR Hot Plate/Stirrer. The sonication was done by aBranson: Ultrasonic Cleaner (Model: 5510) Sonicator. The high temperature synthesis was accomplished using the Acid Digestion Bomb (Parr Instruments: Model number: 302AC-T304-19503) and a VWR International Economy Oven (Model: 1350FM).

The samples were processed using VWR 50 mL centrifuge tubes with screw caps. The principle washing was completed employing either a vortexer (VWR International Analog Mini-Vortexer: VM-3000) and centrifuge (Precision: Durafuge 100) or a large-scale water filtration

regime through a large Büchner funnel and water trap. The samples were prepared for viewing with the scanning electron microscope by utilizing the Quarum Technologies: Polaron Range: SC7620 Sputter Coater having a gold based target system.

Gas sensors were fabricated using an adjustable wire stripper (able to strip small gauge wire), insulated 30 gauge wire, 0.022"-diameter high tech silver bearing solder, and soldering equipment (fine tipped).

2.3. Preparation and Characterization of Samples

2.3.1. X-ray Diffraction (XRD)

The XRD used was a RIGAKU Miniflex X-ray Diffractometer using a Cu Kα radiation source (λ = 1.5405Å). The 2θ range was set to 5 to 70° with a 0.02° step and time of 1.25 seconds. Sample plates were prepared by cutting a silicon wafer disc (111) to have 2.54 cm x 5.08 cm dimensions. These discs were mounted to a standard glass microslide via double sided tape. Once completed, the sample being tested was drop coated onto the sample plate. Enough material was used to ensure an even coat to expand to a surface area of approximately 1.61 cm^2. The slide was allowed to dry in a 100°C oven for 1 hour.

2.3.2. Scanning Electron Microscopy (SEM)

The SEM used was a Philips model ESEM XL30. All SEM samples were prepared by placing a small piece of carbon tape onto an aluminum stubs. After doing so, the sample being examined was diluted and drop coated onto the carbon tape surface and allowed to dry at room temperature. Once dried, the samples were then gold (Au) coated using the Quarum Technologies: Polaron Range: SC7620 Sputter Coater having an Au based target system.

2.3.3. Thermogravimetric Analysis (TGA)

The TGA analysis was carried out using a STA 409 PC LuXX®. The prepared samples (approximately 0.5 to 3.0 mg) were dried at 110°C for 4 hours before TGA analysis. The temperature range evaluated was between room temperature and 500 °C and ramped at a heating exchange rate at 10 °C per minute.

2.4. Syntheses of Titanate Nanobelts (NBs)

2.4.1. Synthesis of Sodium Titanate NBs ($Na_2Ti_3O_7$)

TiO_2 (1.00 g) was added to an aqueous NaOH solution (10M, 40 mL) inside of a Teflon container. The solution was mixed using a Teflon stir rod for 3 minutes. The container was then stirred (via magnetic stir bar) for 10 minutes. The stir bar was removed, and then the Teflon vessel was sonicated for 20 minutes. At the close of the mixing process, the Teflon vessel was sealed inside a stainless steel autoclave container and heated at 240 °C for 72 hours. The autoclave container used is shown in figure 2.1. The resulting white suspension (approximately 1.00 g of titanate NBs $Na_{2n-2}H_nTi_3O_7$) was transferred from the Teflon container to a 50 mL centrifuge tube.

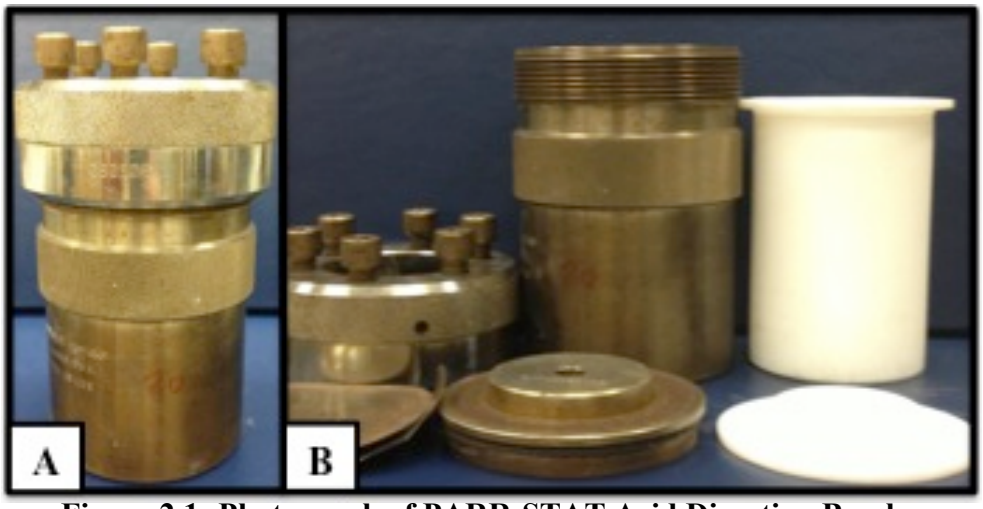

Figure 2.1: Photograph of PARR-STAT Acid Digestion Bomb (A)Fully Assembled & (B) Disassembled

2.4.2. Aging Process Utilizing $Na_2Ti_3O_7$ Forms of Titanate NBs

Titanate NBs (approximately 1.00 g) were sequestered in a centrifuge tube at room temperature for a specific amount of time to allow for further ripening. The tubes are placed horizontally in a storage drawer. The time for the aging process was set to 0, 7, and 30 days. Once the allotted time had elapsed, the titanate NBs were then developed through the ionic exchange process.

2.4.3. Preliminary Post Synthetic Washing Protocol

0.5 g of titanate NBs ($Na_{2n-2}H_nTi_3O_7$) was washed using either using deionized distilled water (DDW) or 0.1 M HCl. Washing was done using a sequence of vortexing for 30 seconds and centrifugation at 3600 rpm for 3 minutes. This protocol was repeated until a pH of approximately 7 was achieved.

2.4.4. Updated Post Synthetic Washing Protocol

2.0 g of titanate NBs ($Na_{2n-2}H_nTi_3O_7$) was placed in a large bottom based porcelain Büchner funnel with a water filtration set-up. The NBs were then washed using 1M NaCl until the filtrate was a pH of approximately 7 was reached. The NBs were removed from the filtration set-up and placed in a 250 mL beaker filled with 150 mL of 1M NaCl and covered with parafilm wax. The beaker was allowed to stir under medium setting overnight. The homogenous solution was rewashed in the same large bottom diameter porcelain Büchner funnel filtration method using 1M NaCl until the pH of approximately 7 was achieved. The NB material was removed and sealed in a Petri dish for drying under room temperature conditions.

2.5. Ion-exchange of the Titanate NBs

2.5.1. Preparation of Monovalent Cation-Exchanged Titanate NBs

2.0 g of titanate NBs ($Na_{2n-2}H_nTi_3O_7$) was washed through filtration using a large Büchner funnel. The NBs were washed using 1M sodium chloride solution until a pH of 7.0 was reached. Once completed, the NBs were removed from the funnel and transferred to a beaker containing 250 mL of 1 M sodium chloride to where it was stirred overnight. Once this material was completed stirring, the resulting pH had risen back to approximately 9.0. Thus, the NB material was then removed and filtered again using deionized distilled water ensuring a pH of 7.0 was achieved.

Once completed, the titanate NBs are transferred to a beaker and 1 M of a monovalent salt selected for intercalation. Each ion is described in Table 2.1.

Intercalation Salt	Monovalent Ion
Hydrochloric Acid (HCl)	H^+
Lithium Chloride (LiCl)	Li^+
Sodium Chloride (NaCl)	Na^+
Potassium Chloride (KCl)	K^+

Table 2.1: Monovalent Salts Intercalated

This beaker was allowed to stir for 3 days under low stirring at room temperature. Once completed, the material was filtered and rinsed with 100 mL of deionized distilled water until a pH of approximately 7.0 was achieved. The intercalated titanate NB material was finally transferred to a Petri dish for drying and storage.

2.5.2. Preparation of Divalent Cation-Exchanged Titanate NBs

Approximately 2.0 g of titanate NBs ($Na_{2n-2}H_nTi_3O_7$) was washed through filtration using a large Büchner funnel. The NBs were washed using 1M sodium chloride solution until a pH of 7.0 was reached. Once completed, the NBs were removed from the funnel and transferred to a beaker containing 250 mL of 1 M sodium chloride to where it was stirred overnight. Once this material was completed stirring, the pH had risen back to approximately 9.0. Thus, the NB

material was then removed and filtered again using deionized distilled water ensuring a pH of 7.0 was achieved.

Once completed, the titanate NBs are transferred to a beaker and 1 M of a divalent salt selected for intercalation. Each ion is described in Table 2.2.

Intercalation Salt	Divalent Ion
Magnesium Chloride ($MgCl_2$)	Mg^{2+}
Calcium Chloride ($CaCl_2$)	Ca^{2+}
Barium Chloride ($BaCl_2$)	Ba^{2+}
Strontium Chloride ($SrCl_2$)	Sr^{2+}

Table 2.2: Divalent Salts Intercalated

This beaker was allowed to stir for 3 days under low stirring under mild heating (40°C). Once completed, the material was filtered and rinsed with 100 mL of deionized distilled water until a pH of approximately 7.0 was achieved. The intercalated titanate NB material was finally transferred to a Petri dish for drying and storage.

2.6. 100% Conversion of the Titanate NBs to Freestanding Membranes

2.6.1. Fabrication of Titanate NB Membrane

- **2.6.1.1. Fabrication of Small Size Membranes (182.41 cm^2)**

Porcelain Büchner funnel with fixed perforated plate (having a 7.62 cm internal diameter) was used in water pumped vacuum filtration. The funnel was positioned over a 250 mL filter flask using a rubber O-ring to maintain constant suction. A filter paper (VWR, Qualitative, 415: Cat. No. 28320-085) was cut to fit and placed inside the funnel.

Once the funnel apparatus was constructed, approximately 0.20 g of intercalated titanate was added to a beaker containing 75 mL of deionized distilled water. This solution was allowed to stir for 10 minutes on a stir plate to allow the NBs in the solution to evenly disperse.

The solution, now the consistency of a heavy cream, was poured into the beaker in the following fashion. Starting from the center of the funnel the solution was slowly poured in a counterclockwise direction working it to the outside edge. This was done to allow for an even distribution of the NBs.

The vacuum suction was slowly applied to the apparatus to remove most of the water present in the funnel. Once completed, the suction was turned off, and the filter paper was carefully removed. A clean glass plate is used to deposit both filter paper and NBs directly onto the surface. This is done carefully to inhibit the formation of any air bubbles that may form between NBs and glass surface and not disturbing the NBs. Once the filter paper is face down allowing full contact between NBs and glass surface, paper towels can be gently used to wick away any remaining moisture from the filter paper, being careful not to disturb the filter paper or NBs.

This was allowed to dry in air at room temperature over the next 24 to 48 hours. The time range is dictated by how much water remains after the wicking is completed. During this time, the nanobelt membrane created will separate from the glass surface. To fully separate the product from the filter paper backing, the filter paper can be easily removed through peeling.

- **2.6.1.2. Fabrication of Large Size Membranes (613.12 cm^2)**

To facilitate the large-size fabrication, a modified Rubbermaid© 9 Cup Easy Find Lid Container having an internal lid depth of 0.25 inches (0.635 cm) was used (refer to Figure 2.2). Standard coffee filters (100 g/m^2) were used to create the necessary covered area. Nine layers of individual filters were applied one at a time using deionized distilled water to situate the filter properly to the apparatus surface. The test set up is shown in figure 2.2.

Figure 2.2: Photograph of Large Size Homemade Membrane Fabrication Device

Once the apparatus was fully set up, 1.50 g of intercalated titanate NBs were washed in accordance to the directions previously indicated. This amount was poured into a 200 mL beaker. Deionized distilled water was added to increase the volume to 150 mL (maximum), and a magnetic stir bar was then added. This solution was allowed to stir for 20 minutes on a stir plate to allow the NBs in the solution to evenly disperse. The remaining preparation is the same as described in the small-size membrane synthesis.

After the wicking process is completed, six paper towels are layered directly on top of the filter paper. This is done to continue wicking water away from the membrane. A clean glass plate is situated directly on top of the paper towels sandwiching the two plates together. A weight of approximately 4.0 kg is placed on top to expedite this process. This is allowed to dry in this manner over the next 48 hours. During the 48-hour drying time, the paper towels are removed and replaced every 12 hours.

At the close of the 48 hours, the weight and paper towels are removed. Then the glass plates are sandwiched together holding only the nanobelt membrane and single filter paper. The

plates are placed in a 100 °C for 24 hours. At the close of the drying time, the nanobelt membrane can be recovered in the same method as previously described.

- **2.6.1.3. Fabrication of Pressed Titanate NB Membrane**

Two presses were constructed, small scale and large scale depicted. The small-scale press is depicted in 2.3 (A). The construction description is in 2.3 (B). The purpose of the membrane presses are to be used to form two sizes of tightly packed membranes. All pieces are slip fit, stainless steel

Figure 2.3 (A): Photograph of Small Membrane Press: Stainless Steel (Scale Bar: cm)

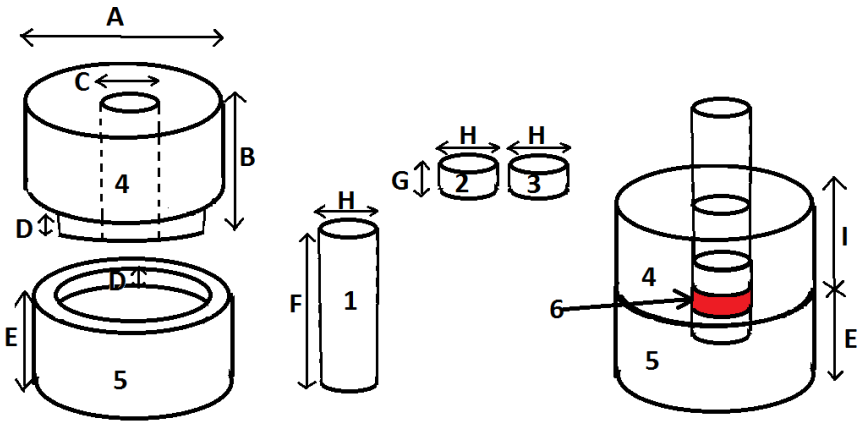

Figure 2.3 (B): Press Construction – Stainless Steel: 1) Press Rod, 2) Upper Press Disc, 3) Lower Press Disc, 4) Upper Register, 5) Lower Register, 6) Sample Press Area

The following describes each component of press designated in figure 2.3.

A) Diameter: (Small Press=50.83 mm, Large Press=89.80)

B) Upper Register Length: (Small Press=41.21 mm, Large Press=63.88 mm)

C) Internal Diameter: (Small Press=12.7 mm, Large Press=40.1)

D) Internal Ridge Secure Mount (Small Press=6.35 mm, Large Press=6.35 mm)

E) Lower Register (Small Press=30.8 mm, Large Press=50.62 mm)

F) Rod Length (Small Press=34.79 mm, Large Press=56.90 mm)

G) Press Disks Length (Small Press=6.39 mm, Large Press=9.55 mm)

H) Internal Diameter: (Small Press=12.71 mm, Large Press=40.10 mm)

I) Upper Register (Small Press=30.8 mm, Large Press=50.62 mm)

So as to check the effectiveness for forming tightly packed layers of the titanate, the press was used by layering ten circular sections (12.7 mm diameter) of titanate into the device and pressed at five thousand pounds per square inch for five minutes. The resulting thickness of the pressed material is approximately 1.5 mm. This process is further depicted in figure 2.3(C).

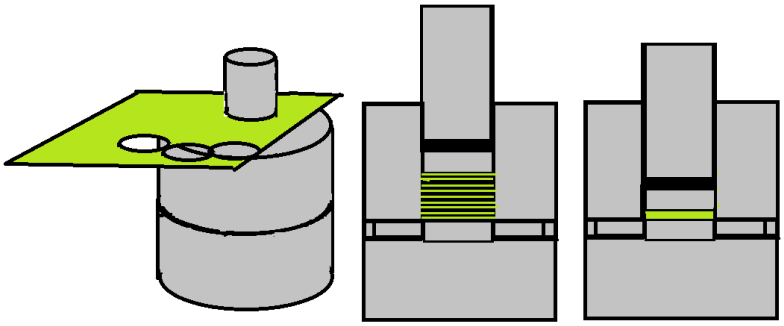

Figure 2.3 (C): Membrane Press – Further Fabrication Process

- ***2.6.1.4. Titanate Membrane Surface Functionalization***

In order to identify the best fabrication methodology, two separate trials were used to ensure complete and prolonged hydrophobicity was ensured in samples. Each is fully described below:

Trial One: Utilizing the sodium and protonated titanate membranes previously created, two 2.25 inch X 2.25 inch squares were cut of each membrane and placed into separate 150 mL beakers. Into two beakers, one containing the Na^+ intercalated titanate NB membrane sample and the other containing the H^+ membrane sample ethyl alcohol (10 mL) and isobutyltrimethoxysilane (5 mL) was added. Into the remaining two beakers, set up similarly using a sodium and protonated form titanate NB membrane, ethyl alcohol (10 mL) and (3-Chloropropyl) trimethoxysilane (5 mL) were added. These solutions were allowed to sit covered and undisturbed at room temperature for 12 hours. The resulting material was then removed and thoroughly rinsed with DDW and dried at 40°C overnight under vacuum.

Trial Two: Utilizing the protonated intercalated titanate membrane, two 2.25 inch X 2.25 inch squares were cut and placed into separate 150 mL beakers. Ethyl alcohol (10 mL) and (3-Chloropropyl) trimethoxysilane (5 mL) were added to each beaker and heated to 60˚C for 12 hours. The resulting material was then removed and thoroughly rinsed with DDW and dried at 40°C overnight under vacuum.

Once the correct trial was identified, further processing was completed. In order to ensure the titanate NB membrane withstands the aqueous environment within the testing chamber, the edges are functionalized creating a hydrophobic surface.

2.7. The Development of NB-Surface Functionalization Chamber

The functionalization chamber was constructed in the following manner. Items required: a tall screw lid thin layer chromatography jar, a 3/8" hexbolt, a compression spring, two 3/8" washers, a ¼" nut, a screw lid 20 mL vial, inert adhesive, and 2 tempered rubber stoppers of the same diameter (3/4"). Three holes are placed in the lid of the chromatography jar (3/8" hole on the outermost region, 3/8" hole in the center, and 1/16" hole on the opposite side). The 3/8" hexbolt and 3/8" washer is placed through the top of the lid of the chromatography jar. The compression spring this then sleeved over the hexbolt and is capped by the other 3/8" washer. A 3/8" hole is placed in the center of the lid of the 20 mL vial. Through this lid the bolt is fed through. The ¼" nut is then affixed keeping the bolt in place. Figure 2.4 further depicts the lid breakdown.

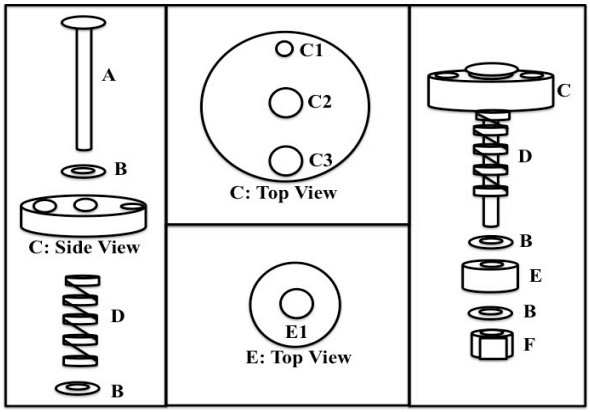

Figure 2.4: Functionalization Chamber Lid Breakdown: A) 3/8" Hex bolt. B) 3/8" Washer C) Chromatography Jar Lid. E) 20 mL Vial Lid. C1, C2, and E1) 3/8" Hole. C3) 1/16" Hole. D) Compression Spring. F) ¼" Hex Nut

A small piece of duct tape is placed around the nut as to keep it from accidently cracking the 20 mL vial. The tempered rubber stoppers are positioned on the bottom of the chromatography jar and 20 mL vial and affixed in place with the adhesive. This will be allowed to cure with all components screwed in place for 48 hours. Figure 2.5 (A) through 2.4 (B) depicts final set up of the functionalization chamber.

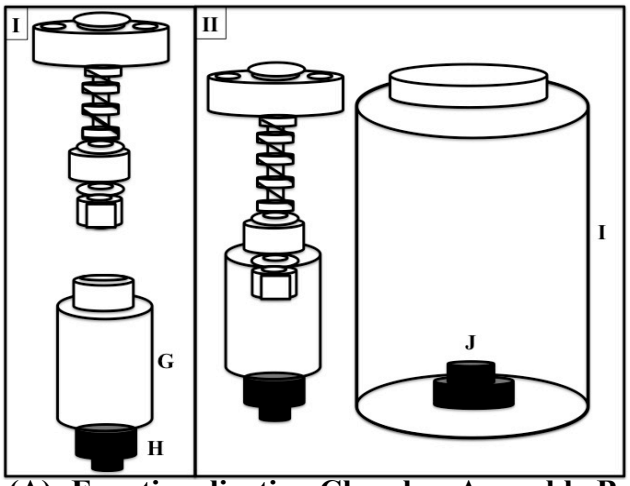

Figure 2.5 (A): Functionalization Chamber Assembly Breakdown G) 20 mL Vial, H & J) Tempered Rubber Stoppers, and I) Chromatography Jar

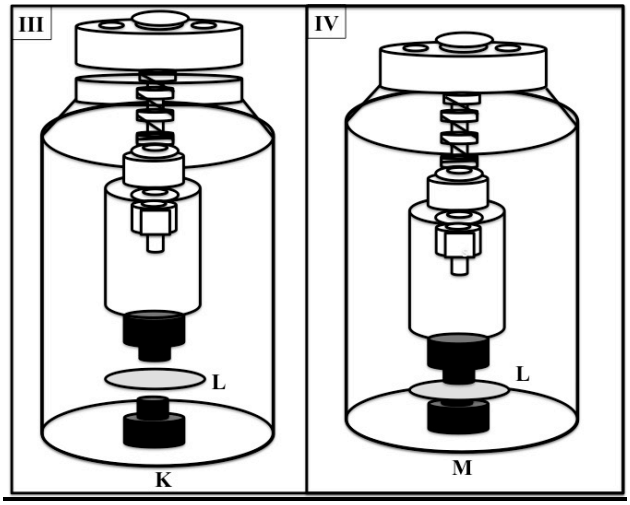

Figure 2.5 (B): Functionalization Chamber Assembly Breakdown L) Titanate NB Membrane, K) Positive Lid Placement, M) Fully Assembled Modification Chamber

In order to utilize the chamber, a small piece (1.5” in diameter) of nanobelt membrane will be centered in the device allowing the chamber spring to hold it in place. The chamber is then slowly filled through the 3/8” hole (via a rod/funnel) with the solution material needed for functionalization, (3-Chloropropyl) trimethoxysilane, the chamber holes are sealed, and placed in a monitored hot water bath for 2 hours.

At the close of which the solution for functionalization is decanted out through the hole it was introduced. The membrane will retain position within the chamber until fully dried (over the next 6 hours). This process is depicted in figures 2.6 and 2.7. The membrane will be then retrieved and the experiment previously described will then proceed.

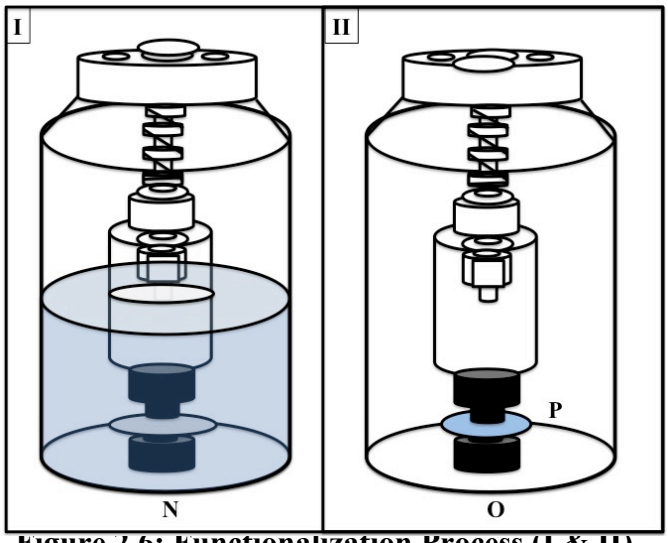

Figure 2.6: Functionalization Process (I & II)
N) Chromatography Jar filled with functionalization solution (shaded area).
O) Functionalization on Titanate Membrane (P) has occurred

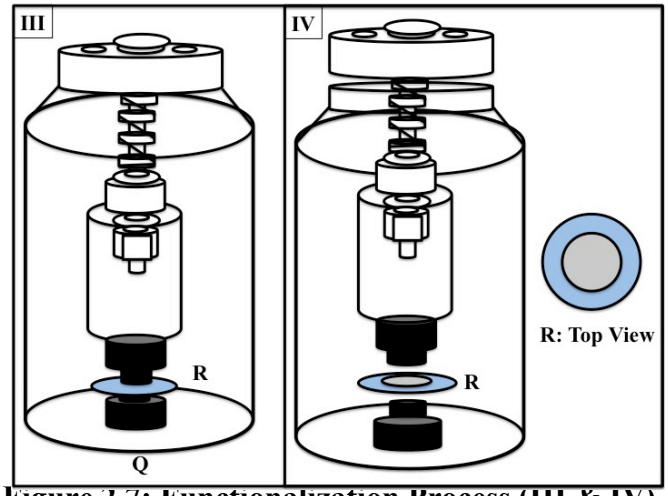

Figure 2.7: Functionalization Process (III & IV)
Q) The functionalization solution is removed. Functionalized area is allowed to dry. R) After drying, the functionalized area (blue) is present in a preselected area. The inner area (gray) is the non-functionalized titanate membrane material

2.8. Fabrication of Nafion©/Titanate NB Composite Membrane

2.8.1. Laminated Composite Membrane

Using a fabricated proton intercalated titanate membrane; a small piece of the membrane was cut to the 12.32 mm X 12.32 mm having a thickness of 0.06 mm. A thoroughly cleaned VWR slide was then prepared using a thin layer of 10% wt Nafion© liquid solution via the doctor blade method. The fabricated material was then placed directly in the center of the Nafion© liquid material. The VWR slide was then placed in an oven at 70°C for 25 minutes in order to remove all solvents still present. The slide was then removed from the oven to cool until reaching room temperature.

After cooling the slide to room temperature, another doctor blade method was employed to coat the sample again, "laminating" the titanate within the Nafion© material. The sample was returned to the 70° C oven to remove all solvents for another 25 minutes. Afterwards, it was removed, cooled to room temperature, all materials used to perform doctor blade was removed,

and then placed in a 165°C oven to anneal the sample for one hour. After cooling to room temperature, the material was further processed using the standard regime (see section 2.6.4.3.).

2.8.2. Blended Composite Membrane

A composite of both dried proton intercalated material and Nafion© was prepared in the following manner. A weight of various weights of intercalated titanate NBs to engage a multitude of different composite percentages, 3 mL of ethanol, and 1 mL of 10% was combined and stirred overnight until homogeneous. This material was then used in the doctor blade technique following a similar methodology as previously stated in the "laminated" method. The material was doctor bladed onto a standard VWR slide, and placed in a 70°C in order to remove any excess solvent for 1 hour. The sample was then removed, cooled to room temperature, then all tape was removed. The slide was placed in a 165°C oven to anneal. After removal and allowing cooling to room temperature, the sample then followed the standard regime (see 2.6.4.3.).

2.8.3. Standard Regime Final Processing of Composites

Final synthetic procedures follow those given for a standard Nafion© membrane preparation for use. First, the sample was boiled in a 3% hydrogen peroxide solution for 1 hour in order to oxidize any remaining organic impurities in the liquid Nafion©. This step also enables the sample to cleanly peel away from the glass substrate. Second, the sample was relocated to a boiling water bath for 1 hour for rinsing. Third, the sample was moved to a 0.5 M sulfuric acid solution for 1 hour in order to remove any ionic impurities in the material. Lastly, the sample was transferred to a boiling water bath for 1 hour in order to rinse any surplus acid remaining. Once completed, the samples are transferred to a Teflon board and covered for drying for 8 hours at room temperature.

2.8.4. Ionic Conductivity Study

Ionic transport across the intercalated titanate membranes (pure form: pressed vs. unpressed and Nafion©/Titanate NBs composites) will be examined. Each membrane sample will be evaluated in the cell depicted in figure 2.8.

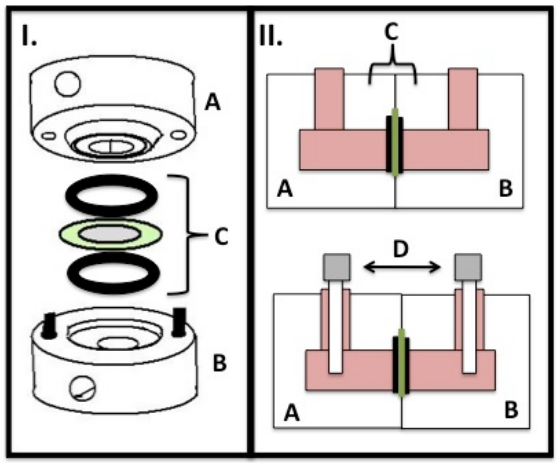

Figure 2.8: Ionic Conductivity Chamber

(I.) The cell consists of Teflon outer chambers (A & B), a separation system through a pair of grommets and membrane to allow the transfer of ions (C), and a set of electrodes (D). Typically, the electrodes are placed to enable an interface where a transfer of charge can occur and be measured. (II.) The cell also indicates (in pink shading) that the internal cavity has a known volume.

This concentration cell will be electrochemically tested via two Ag/AgCl electrodes in a solution of a testing solution. 50 mM HEPES Buffer/50 mM KCl will act as an equilibration solution. The concentration of one chamber will be altered incrementally through the addition of 10 to 20 µL of 1M KCl. Once added, the testing apparatus will be immediately connected to a source of voltage. A voltage limit of -100 mV and +100 mV will be applied to the cell in 10 mV increments. The resulting micro amps (µA) will be evaluated at 30 seconds. This data is plotted

on a current versus voltage graph to indicate where the saturation current resides for each concentration of ion.

2.8.5. Water Uptake ($WU_{\%}$) Evaluation[144]

Each Nafion©/titanate NB composite membrane was tested for hydration level via the following method: Each membrane will be vacuum dried at 110°C for 4 hours and removed and weighed at room temperature (m_{dry}). The membranes are then placed in boiling water for 1 hour. The water saturated membrane samples are removed and carefully blot dried with pH neutral tissue paper. Once the samples reached room temperature, the membranes are reweighed (m_{wet}). The mass-based water uptake (WU) is calculated using the following formula:

$$\mathbf{WU_{(\%)} = [(m_{wet} - m_{dry})/m_{dry}] \times 100\%}$$

2.9. Development of Titanate NBs-based Gas Sensor

2.9.1. Fabrication of Gas Sensor

The overall size of each electrode is 4x4 mm (metal-edge-to-metal-edge). The large pad on each side of the cell is 1x4 mm. Each finger is 25 microns wide; there are 25 microns between them. Each finger is 1.975 mm long, which leaves a 25-micron gap between it and the contact pad. The interdigitated electrode (IDE) is further shown in figure 2.9.

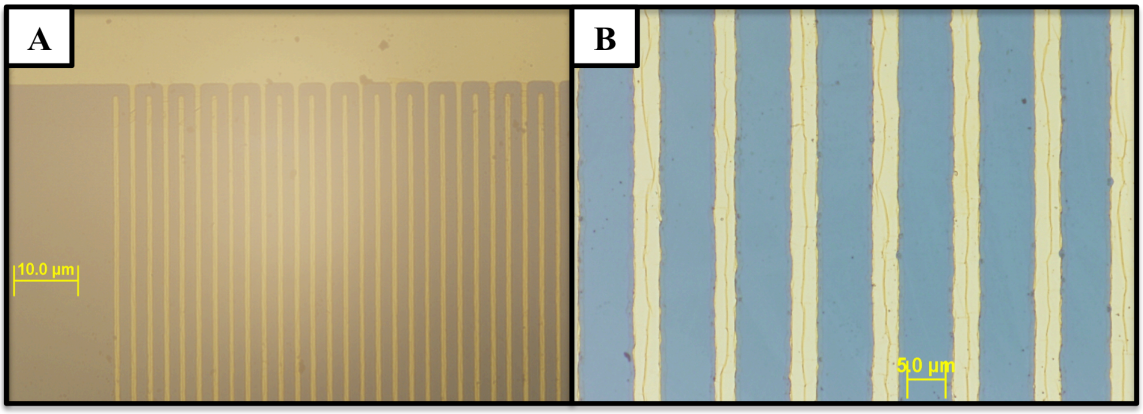

Figure 2.9: Blank Interdigitated Electrode (IDE) Pad Surface:
(A) Pattern View (Scale-Bar: 10 µm), (B) Close-up View (Scale-Bar: 5 µm)

Two 30 gauge wires were cut to a length of 3 inches (7.62 cm). The ends of these wires were stripped to a length of 0.25 inches (0.635 cm). The ends of the wire were tinned using the silver solder, and these ends were soldered to the corners of the interdigitated electrode. The exposed solder connection was then covered with an inert material (Silicone1*(Standard Waterproof Caulk) GE©) to add in to the insulation. This covering was then allowed to cure over the next 24 hours, as per manufacturer specifications.

2.9.2. Coating Methodology

Utilizing the intercalated processed titanate, a 1% wt solution of each sample was prepared in a 2 mL centrifuge tube. The solution was vortexed for 30 seconds to allow the solution to achieve homogeneity. Once completed, a 30-µL sample of this solution was removed and dropped coated in the center of the interdigitated electrode. This amount was chosen to allow for maximum diameter to coat entire sensor probe. The prepared electrode was placed in the oven at 60˚C for 45 minutes to ensure delaminating of coating does not occur. The construction and coating process is further depicted in figure 2.10.

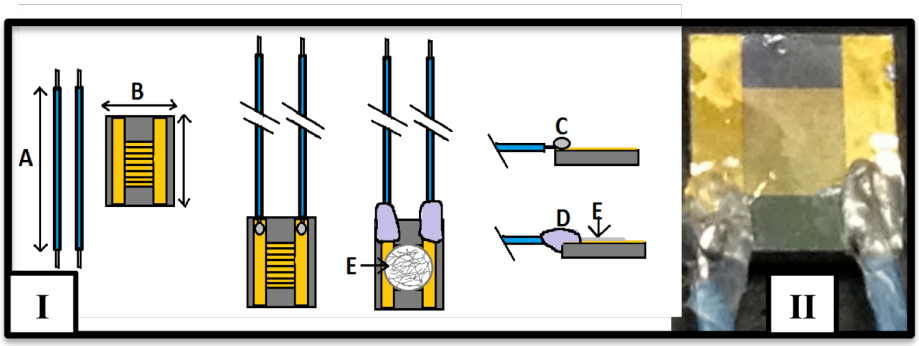

Figure 2.10: Gas Sensor Fabrication & Coating Process:
I. A) Two 30-gage wires cut 7.62 cm each. B) IDE dimensions: 6.35 mm X 6.35 mm
C) Solder joint D) Silicone1*Standard waterproof caulking
E) Intercalated titanate NB coating
II. Finalized fabricated gas sensor

2.9.3. Development of Relative-Humidity Chamber

Using capped 20 mL vials; two 1/8" holes were drilled into each lid to allow sufficient clearance of the 30-guage sensor wires. The wires were extended to allow the sensor to be centered in the vial's headspace. Once the sensor was properly situated, parafilm was used to secure the sensor in place and to allow the lid to be airtight in the vial containing the relative humidity solutions. Each vial contained saturated concentrations of the following compounds [146, 147]: Magnesium chloride hexahydrate (RH = 33%), magnesium nitrate hexahydrate (RH = 53%), sodium chloride (RH = 75%), ammonium sulfate (RH = 81%), potassium nitrate (RH = 92%), and deionized distilled water (RH = 100%). The vials were then sealed trapping the probe inside. This process is further explained in figure 2.11.

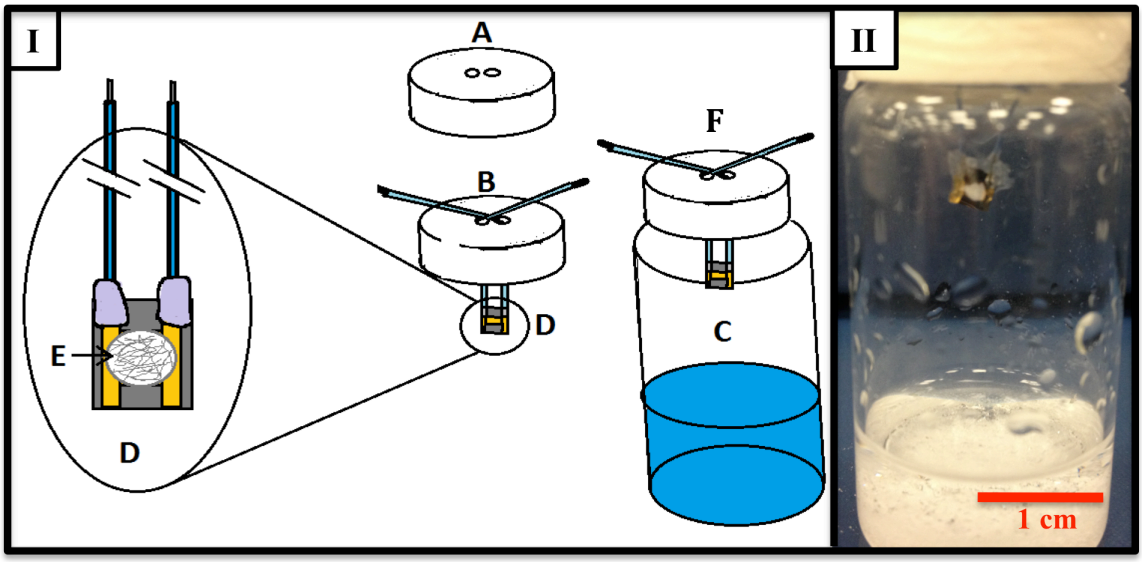

Figure 2.11: Sensor Test Chamber Breakdown:

(I) **A) Lid with 1/16 holes for wire feed through. B) Wires fed through the lid of chamber-allowing the probe to extend one inch into the chamber area. C) Fully assembled chamber. Blue shaded area=relative humidity control substance. D) Expanded sensor E) Intercalated titanate NB coating. F) Test Chamber.**

(II) **Test Chamber with probe (Scale Bar: 1 cm)**

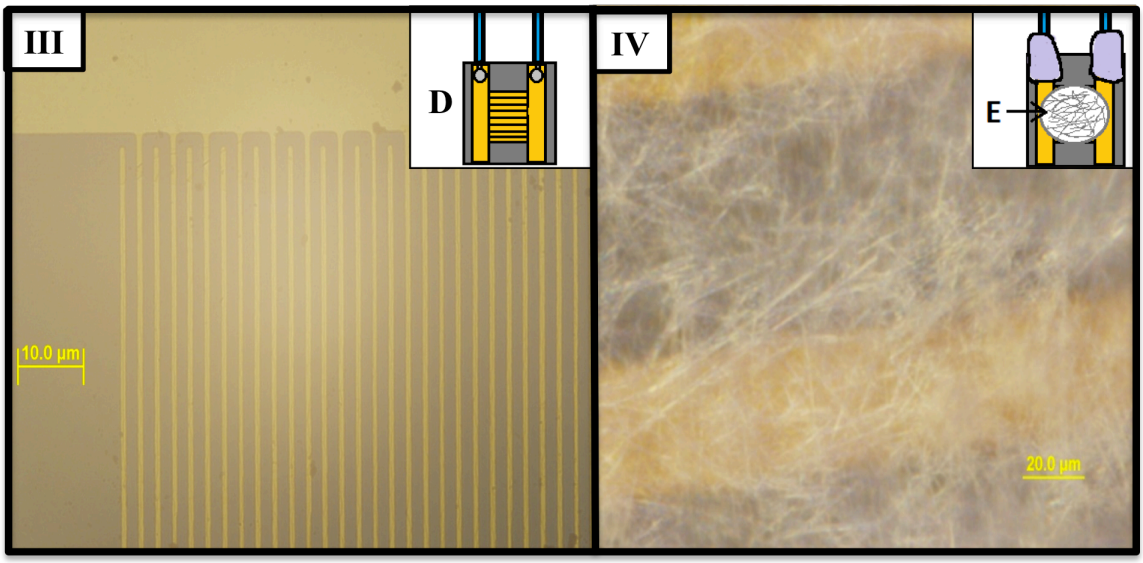

Figure 2.11: Sensor Test Chamber Breakdown:

(III) Blank Interdigitated (IDE) Array (Scale-Bar: 10 µm), Inset: (D) Blank IDE Array (Scale Bar: 10 µm)

(IV) Intercalated Titanate Coated IDE Array (Scale-Bar: 20 µm), Inset: (E) Coated IDE Array. (Scale Bar: 20 µm)

CHAPTER 3

RESULTS & DISCUSSION

3.1. Unique Ion-exchange for the Titanate Nanobelts (NBs)

3.1.1. Aging Effect –I. The Criticality of the First Step of Washing

In previous work accomplished by our group, only ~30% of the titanate NBs was useful in construction of nanobelt (NB) membrane. This issue was left mystery until three years ago when the thesis work started systematically.

One part of the leftover issue was that in the previous work, only the top part of the product floating in the supernatant with the cotton-like appearance was utilized for membrane construction. As a result, a large portion of the product was wasted, and if using 100% product then the diameter of the freestanding and flexible membranes was small. It was found that in the synthetic process of the titanate NBs, another step that should be added is the extra stirring before internment in the autoclave container, probably for increasing the dispersion homogeneity hence the reactivity of the TiO_2 (P25) in the 10 M NaOH solution. It has become apparent that the extra stirring for 10 minutes has improved the growth yield in this process.

Another part of the issue was that even with the addition of the stirring has enabled more workable product, the amount of the product was not enough to facilitate a high quality membrane in a large size (~ 6”). Hence, an additional room-temperature aging (or RT-ripening) in the basic environment was proposed, and found workable to improve the yield.

This new role of the RT-aging has rarely been discussed in literature. As a start, after the autoclaved raw product (e.g. sodium titanate NBs) was transferred from the autoclave liner to a plastic storage vial and cooled to room temperature, it was observed with a surprise that the titanate NBs seemingly continues to grow in the high-basicity supernatant.

After several weeks, what was repeatedly confirmed upon visual inspection of the storage vials is that large titante NB-mass, which typically clusters and accumulates at the bottom of the centrifuge tube, had begun to fill the tube with a cotton-like appearance (depicted in figure 3.1 (A)). Upon a closer study in a systematic manner, as shown in figure 3.1 (B) and (C), the titanate NBs were found to be able to form polymeric dendrimers during the aging process, which is exciting. This reveals an advantageous and exciting benefit of the RT-aging that may play a critical role in nanosynthesis in general, which may even be a new chapter to both the nanosynthesis and the solution-based self-assembly.

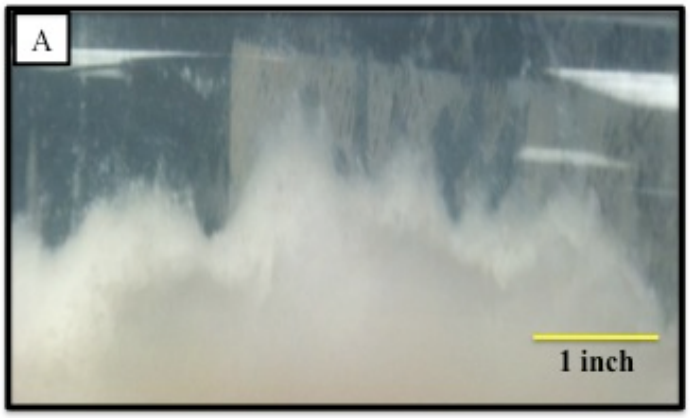

Figure 3.1 (A) Raw titanate NB sample after being aged for 14 days in a 50 mL centrifuge tube

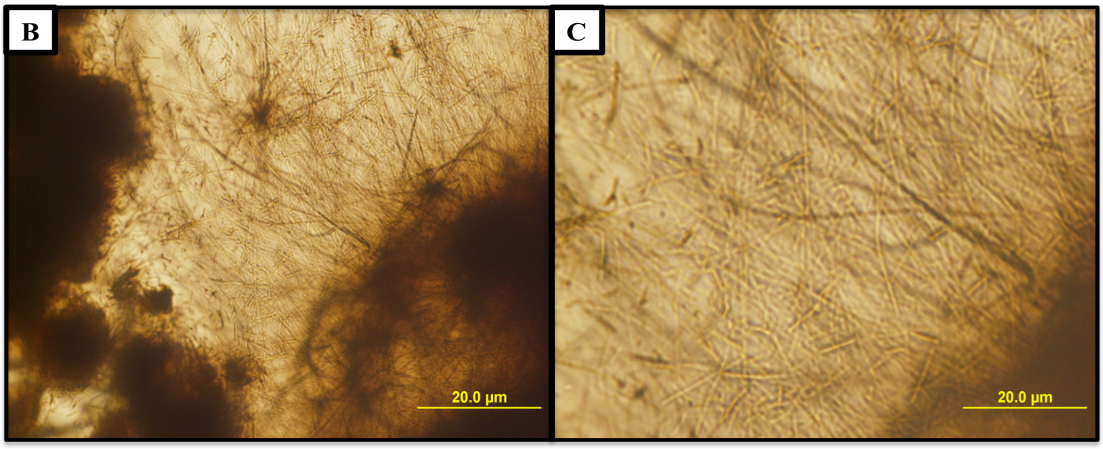

Figure 3.1 (B) & (C) Optical photo of dendritic titanate NB formation – Aged 14 Days (Scale Bar: 20 µm)

Accordingly, a video clip was recorded for the titanate NBs after the RT-aging in the basic supernatant only after 14 days, and uploaded to YouTube (http://youtu.be/2XskE0bx574), which shows the cotton-like appearance.

To analyze the RT-aging polymerization (or self-assembly) observed in the stored vials, the samples were allowed to continue to age undisturbed in a plastic tube over a variety of time spans (day 0 = "A", day 7 = "B", and day 30 = "C"). Figure 3.2 depicts the SEM results of the thus aged or self-assembled titanate NBs. The titanate NBs were taken directly from the 10M NaOH without further processing.

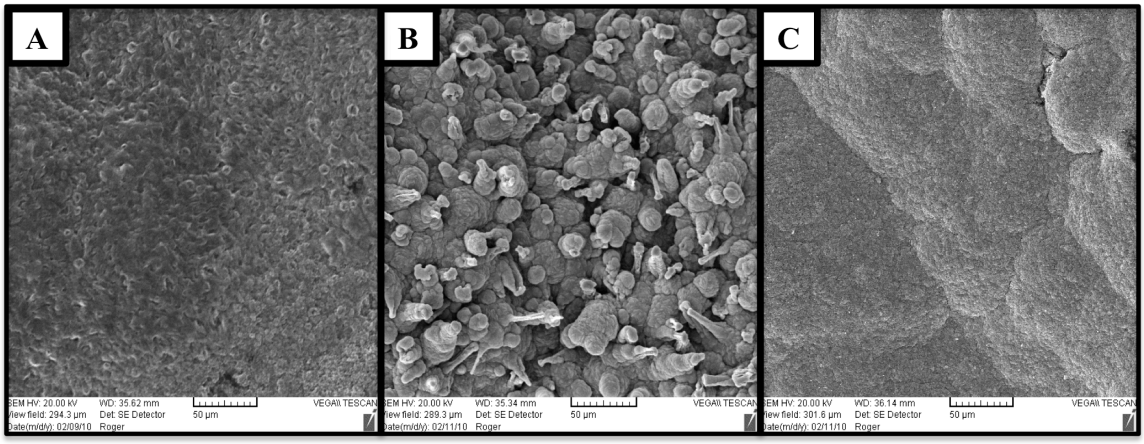

Figure 3.2: SEM Images of Aged (Unwashed Raw) Titanate NBs (Scale Bar: 50 µm): (A) Day-0, (B) Day-7, (C) Day-30

However, the cotton-like assembly does not indicate as such in figure 3.2, they do show a distinct structural difference as the time progresses in the supernatant as observed in figure 3.1 (B) and (C). These results indicate the necessity of further washing procedures. Furthermore, an interesting feature is represented in Figures 3.3 through 3.4. These indicate a significant change in structural dimensions displayed after different post synthetic washing techniques described in section 2.4.3 (deionized distilled water (i.e. DDW), and hydrochloric acid (i.e. HCl) were employed during the titanate synthesis.

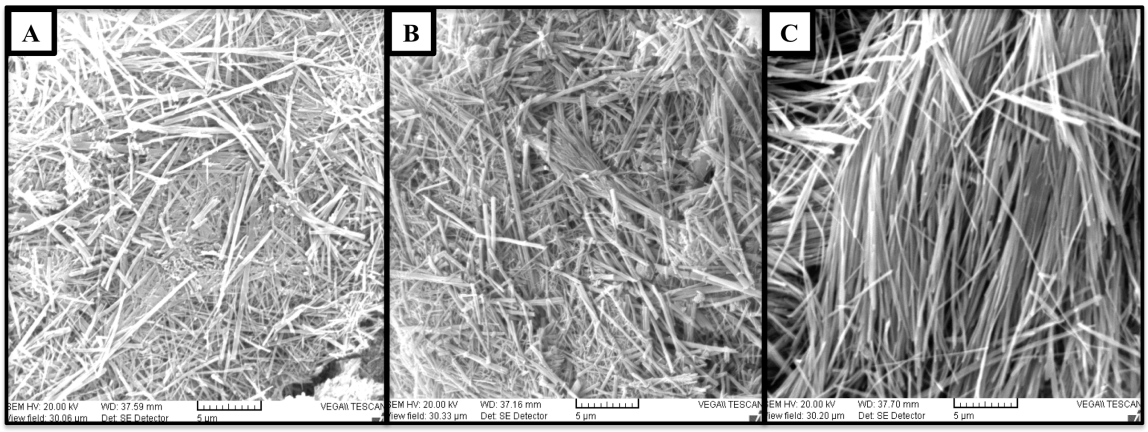

Figure 3.3: SEM Images of Aged Titanate NBs Post Deionized Distilled Water (DDW) Washing (Scale Bar: 5 µm): (A) Day-0, (B) Day-7, (C) Day-30

In figure 3.3, as the post synthetic DDW washing was applied to aged form titanate NBs, the structure retained width dimension and lengthened. Although this is only slightly noticeable, between day 0 (Figure 3.3 (A)) and 7 (Figure 3.3 (B)) it becomes more pronounced at the day 30 mark (Figure 3.3 (C)).

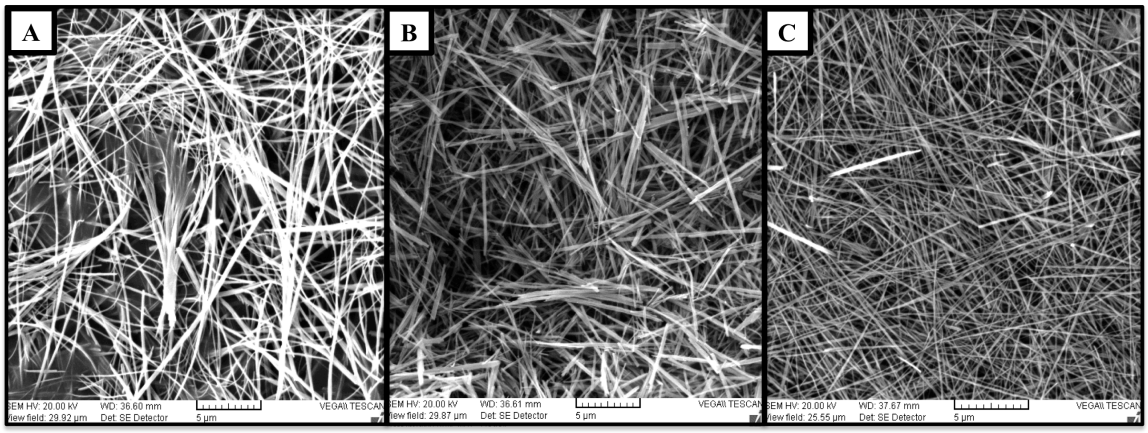

Figure 3.4: SEM Images of Aged Titanate NBs Post HCl Washing (Scale Bar: 5 µm): (A) Day-0, (B) Day-7, (C) Day-30

When HCl washing is applied to aged form titanate NBs, the structure's width is diminished and the length is allowed to extend to a small degree. Again, this dimensional change is only slightly noticeable, between day 0 and 7 (figure 3.4, (A) and (B) respectively) it becomes more pronounced at the day 30 mark (figure 3.4 (C)). The instantaneous pH change is likely the direct cause of this shift in structural stability. The pH of the DDW was ~ 6, whereas the pH for the HCl was observed at ~ 2. Introduction into this environment allows the nanomaterial to undergo immediate ion exchange process causing structural defects along the longitudinal surface. Due to this, the resulting structure is altered depending technique utilized.

The question then became since the additional aging played such an effect with the synthesis of the layered titanate NB structure, as depicted in figure 1.3, what effect if any, does it have with the intercalation of various cations? To answer this question, the XRD patterns of the lattice matrix were further investigated. Based on Bragg's Law, the diffraction peak of an XRD pattern may shift from the (001) plane to a higher or lower 2θ angle due to the presence of decreased or increased sizes of the cations present. The core 2θ peak within the tolerance range of 9 to 11 theta was evaluated due to the intercalated specificity of the $d_{(001)}$.

This peak identifies the level of intercalation possible for this layered material through shifting. Typically, the diffraction peaks for this crystal phase reside in the (002), (004), etc. due to sample stage orientation. Three separate trials were performed in the creation of the titanate membranes (aging day 0, 7, and 30). This study was evaluated to identify which washing technique yielded the highest crystallinity versus the time allotted for continued growth (if any existed).

Figure 3.5 represents trial day zero aging, the results from XRD indicate the following characteristics. The unwashed, day zero sample 2θ peak at 10.91˚ indicates the lack of washing technique suppresses the crystallinity of the sample being evaluated despite the aging process. This is further observed in the XRD results in figures 3.6 and 3.7, as well as the SEM results in figures 3.2, 3.3, and 3.4.

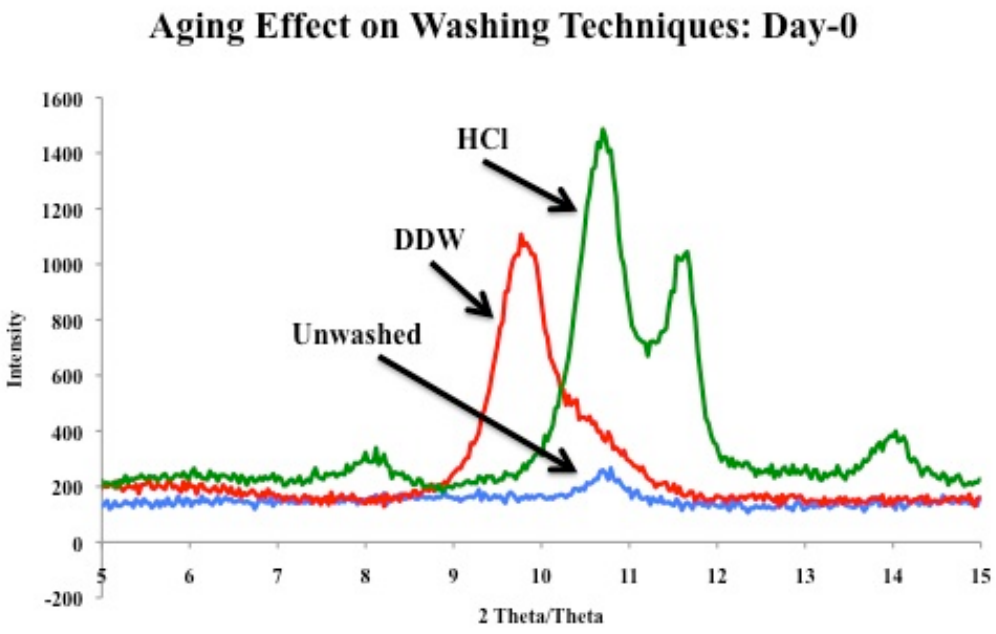

Figure 3.5: XRD Patterns of Samples From Different Washings: Day-0

The DDW washed, day zero 2θ peak at 9.77˚ indicates the presence of nanobelt formation with a higher crystallinity than the 2θ peaks at 10.64˚ and 11.54˚ has for the HCl process indicates.

However, the $d_{(001)}$ peak shift observed in the HCl technique acknowledges the direct intercalation effect of dominance of protons within the lattice matrix; whereas, the DDW technique may possess a mixture of both sodium and protons within the lattice. The mixture is presence of mixture of both sodium and protons is likely due to the higher pH level DDW offers during the washing procedure when compared to the HCl technique.

The crystallinity and peak shift trending from day 0 is continued through the rest of the titanate NB aging. Figure 3.6 represents trial day seven, the results from the XRD indicate the following characteristics: The DDW washed, day seven 2θ peaks at 9.47˚ and 10.52˚ indicates a distinct crystallinity change occurs despite the washing technique employed, which is further identified by the 2θ peaks are present at 10.94˚ and 11.57˚ in the HCl process.

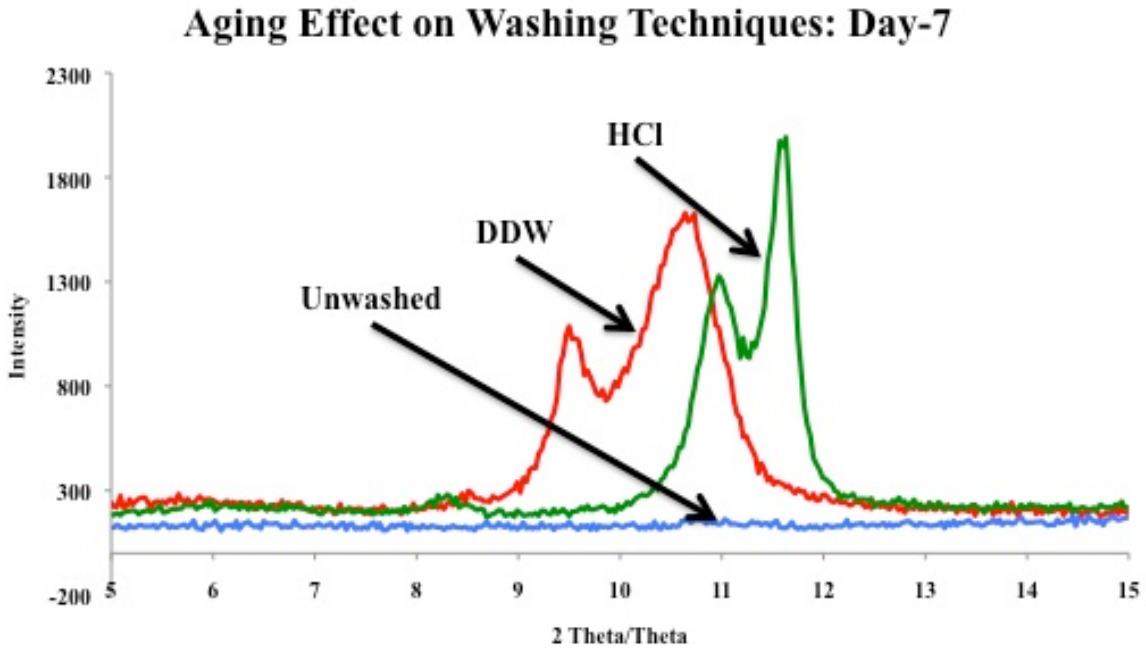

Figure 3.6: XRD Patterns of samples from different washings: Day-7

Figure 3.7 represents day 30, the results from the XRD indicate the following characteristics: The DDW washed, day 30 2θ peaks at 9.56˚ and 10.61˚, indicates a lower crystallinity when compared to the HCl washed, day 30 2θ singular peak at 10.91˚. This indicates

the HCl washing form when aging for 30 days yields a higher crystallinity and survivability to mechanistic intercalation types typically used (e.g. stirring, heating, etc.).

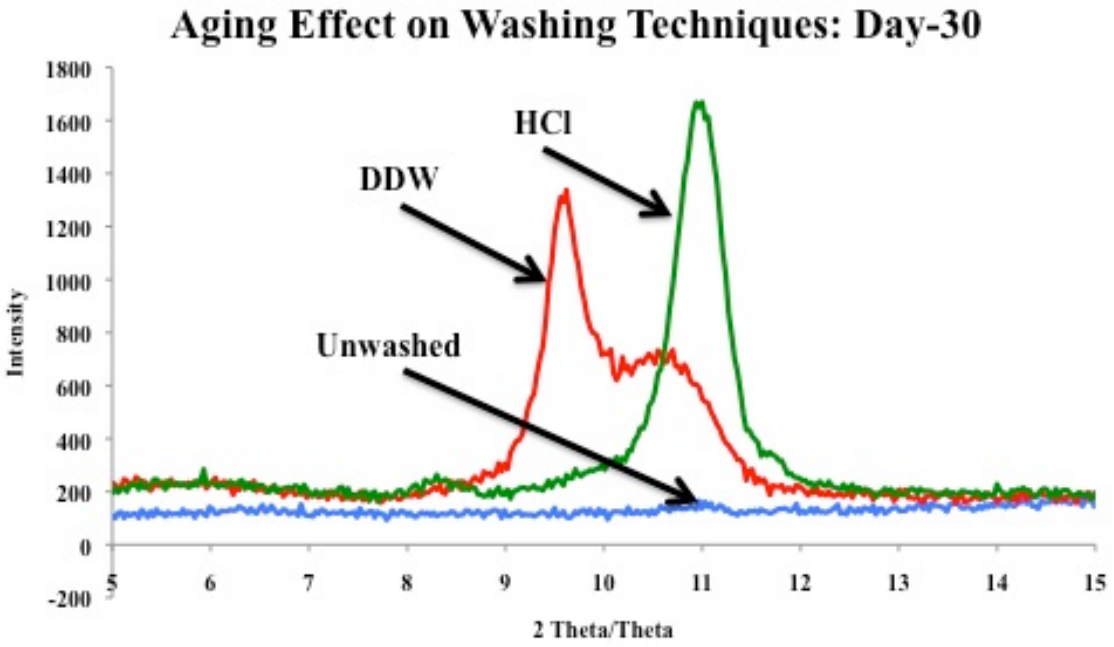

Figure 3.7: XRD Patterns of Samples From Different Washings: Day-30

To further illustrate the intercalation effect, the HCl washed, day zero was slowly stirred in a covered beaker for two weeks in a 0.1 M HCl solution. Figure 3.8 shows the XRD comparison of this prolonged protocol. As comparison, the day 30+ sample using standardized intercalation techniques (e.g. stirring for 3 days in 1M HCl solution) is also included. The XRD diffraction peak in the prolonged intercalation protocol indicates a lower crystallinity value when compared to the aged sample when under normalized intercalation protocol. Also, the positioning of the $d_{(001)}$ peak in both suggests the intercalation utilizing the aged product produces a higher level of ion exchange while retaining crystallinity.

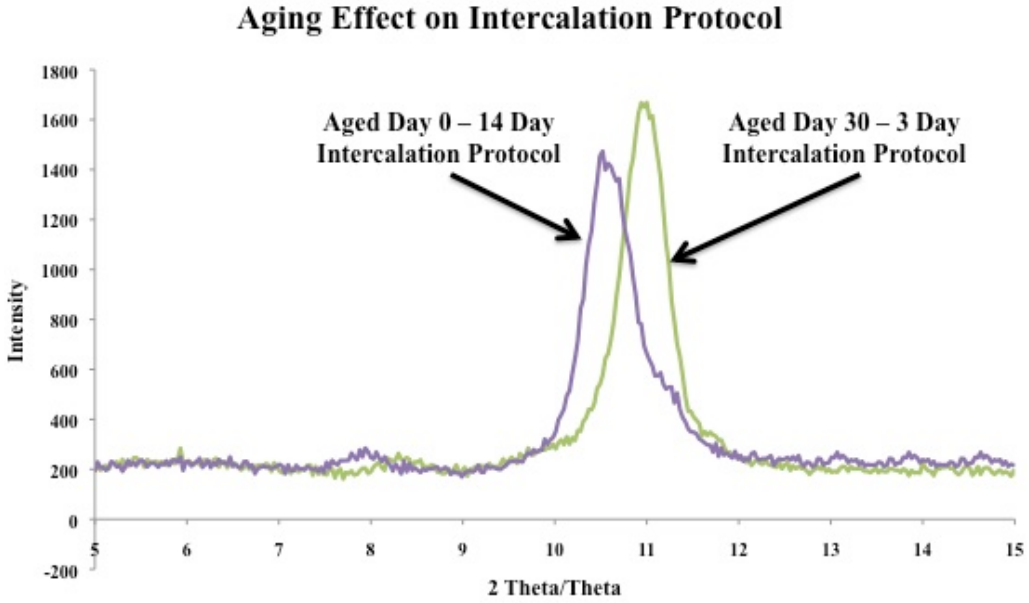

Figure 3.8: XRD Patterns for Samples Showing Aging and Intercalation Effects

Furthermore, this structural change can be directly observed from the SEM results depicted in figure 3.9 [(A) prolonged intercalation protocol using aged day zero raw form and (B) normalized intercalation protocol using aged day 30 raw form]. This seems to prove the forced intercalation seen observed was unnecessary in the aged sample. The stored sample allows the material to retain the dimensional characteristics and a similar intercalation.

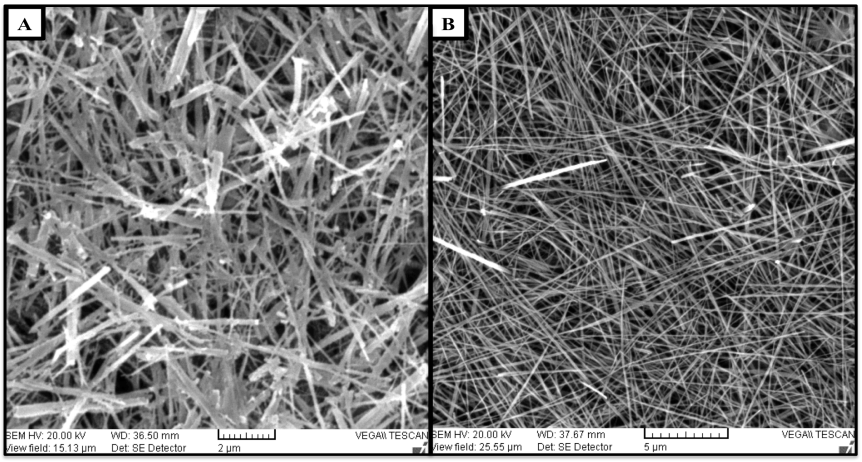

Figure 3.9: SEM Images of Further Intercalation Protocol of Aged Titanate NBs HCl Washed: (A) Aged Day-0 – 14 Day Intercalation (Scale Bar: 2 µm) (B) Aged Day-30 – 3 Day Intercalation (Scale Bar: 5 µm)

3.1.2. Aging Effect – II. The Criticality for the Final Step of Washing

Using DDW and HCl protocols on aged day 30 titanate NBs, a small-size membrane (using protocol described in 2.6.1.1.) was successfully formed. However, it became apparent the DDW formed membrane yielded a more flexible titanate NB form shown in figure 3.10.

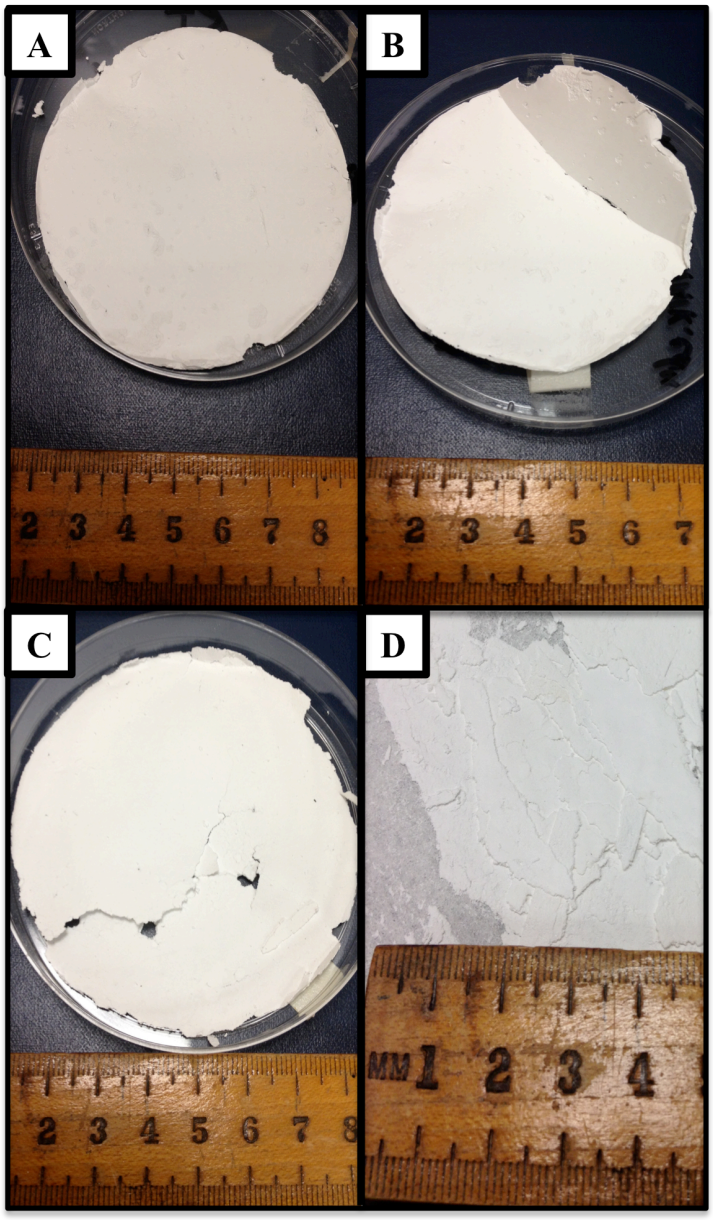

Figure 3.10: Photographs of Small-Size Titanate NBs Membrane (Scale Bar: mm): (A) DDW Washed: Fabricated Membrane (B) DDW Washed: Flexibility Failure (C) HCl Washed: Fabricated Membrane, (D) HCl Washed: Flexibility Failure

As depicted in figure 3.10 (A), the DDW post synthetic washing technique yielded the better quality membrane (when compared to HCl (B)).

Unfortunately, the flexibility of the both small-scale titanate NB membranes is stymied until the reasoning for this structural effect on flexibility was better understood. In order to obtain the best opportunity for successful fabrication of a titanate NB membrane, the day 30 aged sample was used. Figure 3.11 shows the center of the fabricated membrane form using the DDW protocol. The results of using the DDW washing indicates that the post synthetic washing yields a shorter (though stouter) NB form; whereas in figure 3.12 (HCl protocol) all NBs present harbor a higher concentration of longer (though thinner) structure.

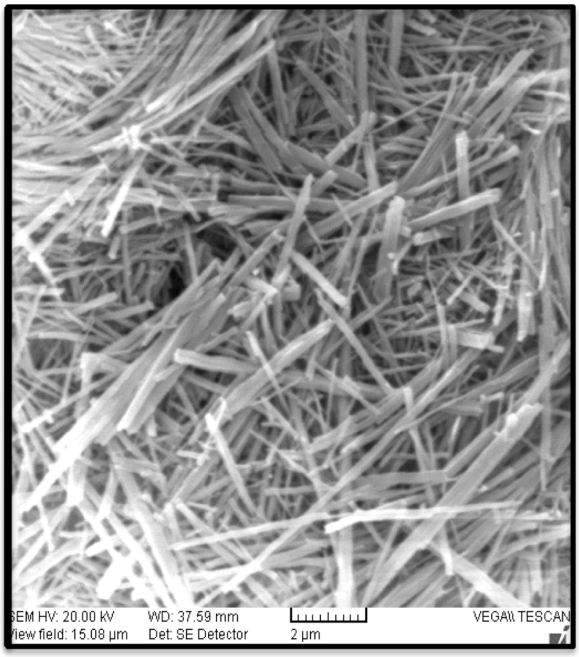

Figure 3.11: SEM Image of Titanate NB Membrane Center Using DDW Washing (Scale Bar: 2 µm)

These results demonstrate how the DDW is more rugged form, but is not indicative of the flexibility a thinner NB would have from the HCl process. The stability reasoning becomes clear when the environmental pH of the titanate NBs in the aforementioned membranes are considered. Through the HCl washing procedure, the basic environment undergoes a fast pH

change (e.g. from a very high pH to very low pH) to causes severe surface defects along the longitudinal surface of the titanate NB. Surface defects due to the pH quenching process may affect the overall instability of the NB during the membrane formation.

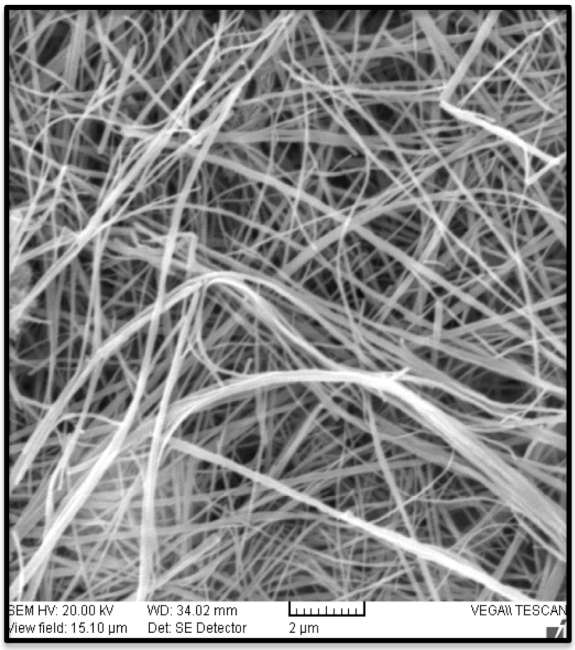

Figure 3.12: SEM Images of Titanate NB Membrane Center Using HCl Washing (Scale Bar: 2 µm)

As discussed in section 1.7, the ability to produce a protonated titanate NB without this structural instability is very crucial if forward momentum in the fuel cell field is to take place, thus another post synthetic technique was sought.

As discussed in section 2.4.4., the 1M NaCl post synthetic technique shows the most promise. In order to observe any change resulting from this technique, only the two extremes were chosen (aged day 1 and day 30). The pH of the 1M NaCl was ~ 7.0. The titanate NBs was processed slowly to control the drop of pH to insure absence of surface defects. The SEM and XRD results of both aged forms are shown in figures 3.13 and 3.14 respectively.

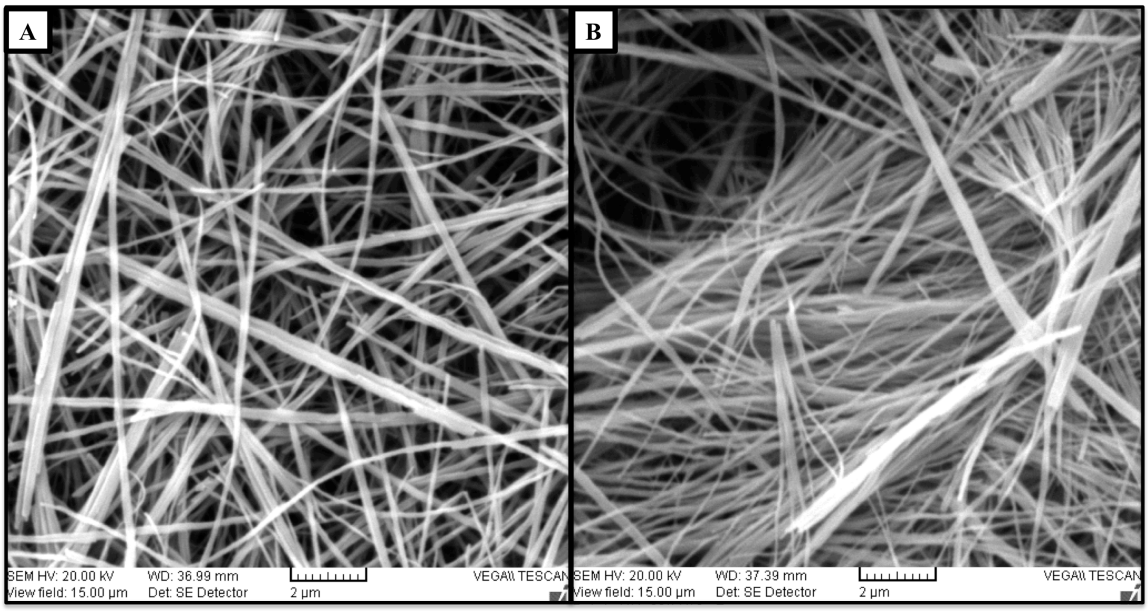

Figure 3.13: SEM Images of Aged Titanate NB Membrane Center Using NaCl Washing (Scale Bar: 2 µm): (A) Day-1, (B) Day-30

In figure 3.13, the SEM results show the 1M NaCl post synthetic technique yielded no observable surface defects in the longitudinal surface; thus indicating the pH control allows for a structurally stable NB to be formed.

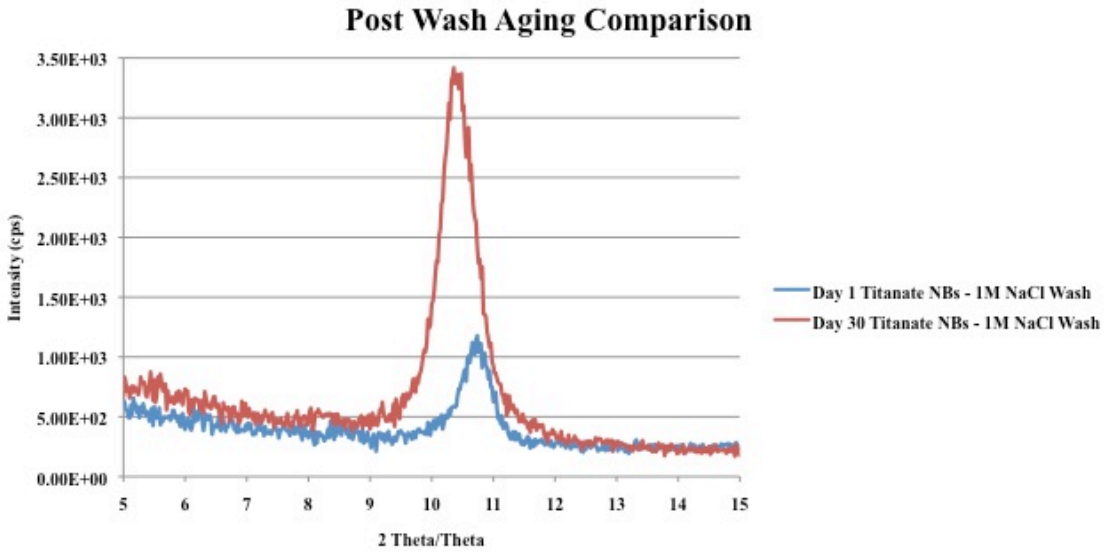

Figure 3.14: XRD Patterns for Samples Showing Aging Effects on NaCl Washing

In figure 3.14, the XRD results indicated the $d_{(001)}$ peak are observed at 10.36° (day 30) and 10.72° (day 1). The day 30 peak shows an increased crystallinity and likely has an abundance sodium intercalated within the lattice matrix; whereas, the day 0 peak possesses a reduced crystallinity and likely has a mixture of both sodium and protonated ions within the layered NB structure.

The 1M NaCl washing procedure (see 2.4.4.) was successfully used on an aged day 30 titanate NB to form a small-size titanate NB membrane shown in figure 3.15. The small-size NB membrane possesses increased flexibility and structural stability the previous methods do not. During the fold examination, the membrane did not yield a crack along the surface as observed in figure 3.10.

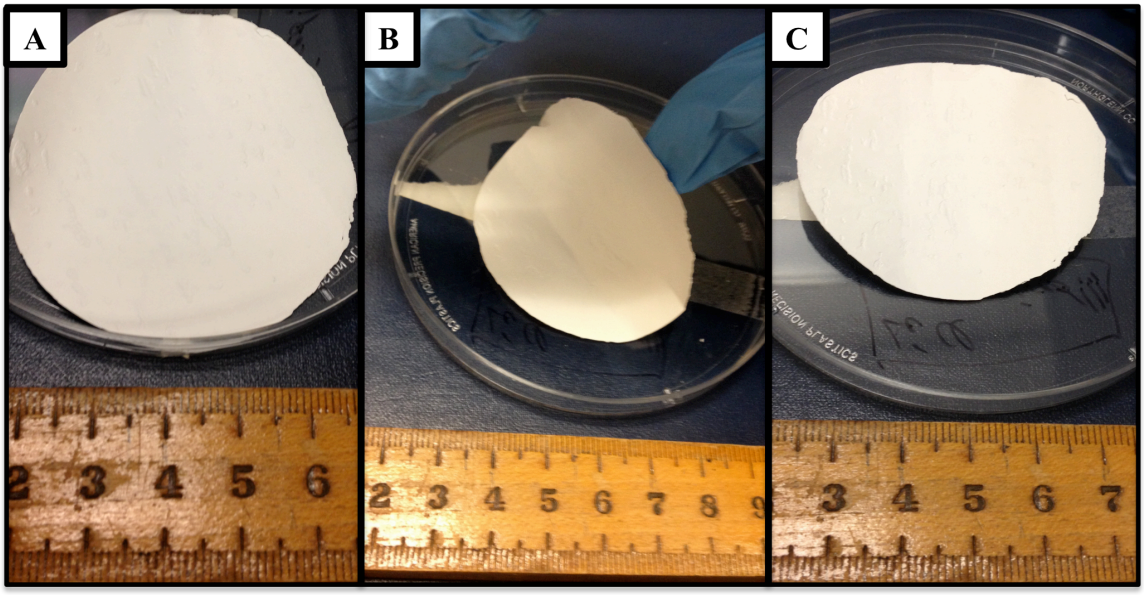

Figure 3.15: Photographs of Small-Size Titanate NBs Membrane Using NaCl Washing Technique (Scale Bar: mm) – (A) As Fabricated, (B) Initial Flexibility Results, (C) Post Flexibility Results

Figure 3.16 depicts the comparison with the previously discussed membranes. Figure 3.17 shows a close up of the internal view of the NaCl washing technique of the titanate NB membrane.

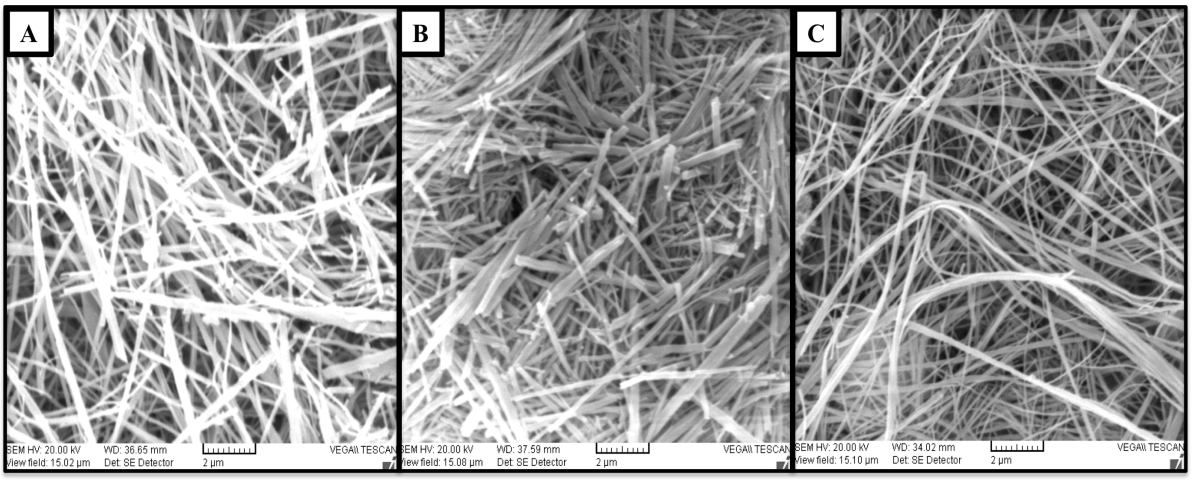

Figure 3.16: SEM Images of Titanate NB Membrane Comparison (Scale Bar: 2 µm): (A) NaCl Washing Technique, (B) DDW Washing Technique, (C) HCl Washing Technique

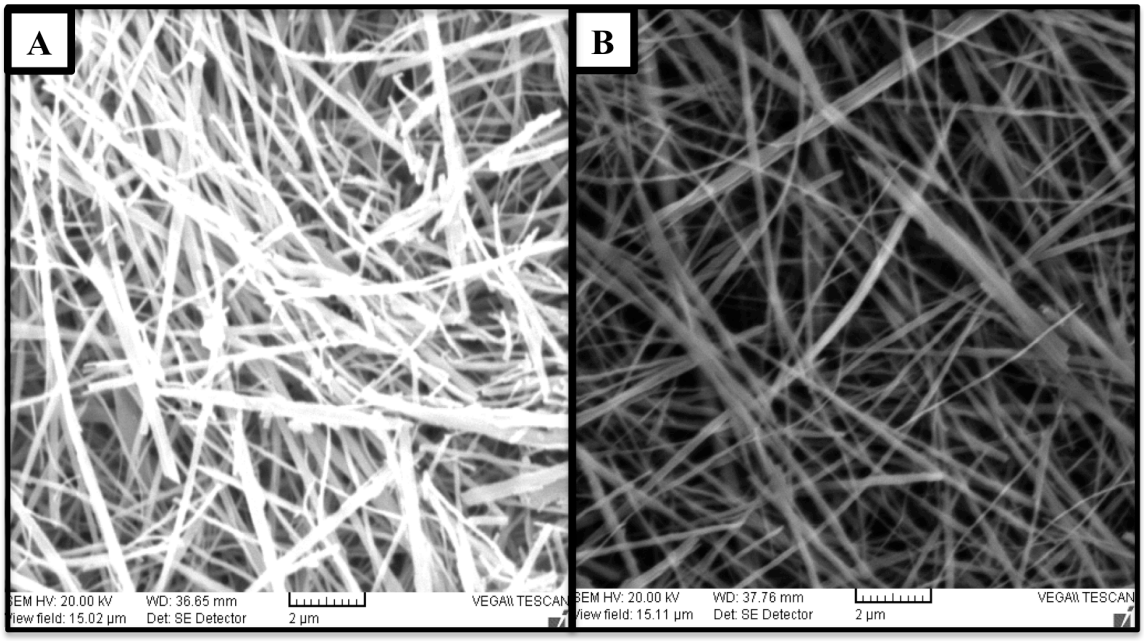

Figure 3.17: SEM Images of Titanate NB Membrane NaCl Washing Technique (Scale Bar: 2 µm): (A) Face On View of Center, (B) Close Up View

As shown in figure 3.17, the NaCl washing technique yielded no discernable longitudinal surface abnormalities.

The 1M NaCl washing technique has successfully formed a small-scale titanate NB membrane. However, as discussed previously, a successfully fabricated protonated titanate NB

membrane needs to be achieved. To do this, first an ion intercalation study using the 1M NaCl washing technique is required.

3.1.3. Aging Effect – III. The Criticallity of Aging on the Intercalation of Cations

Aged day zero samples were used during intercalation procedures using separate monovalent (H^+, Li^+, Na^+, and K^+) and divalent (Mg^{2+}, Ca^{2+}, Sr^{2+}, and Ba^{2+}) cationic capable solutions at room temperature. The resulting XRD data obtained from figures 3.18 represent monovalent cations and 3.19 represent divalent cations. The intercalation layer ($d_{(001)}$) of the titanate NBs are further summarized in tables 3.1 and 3.2.

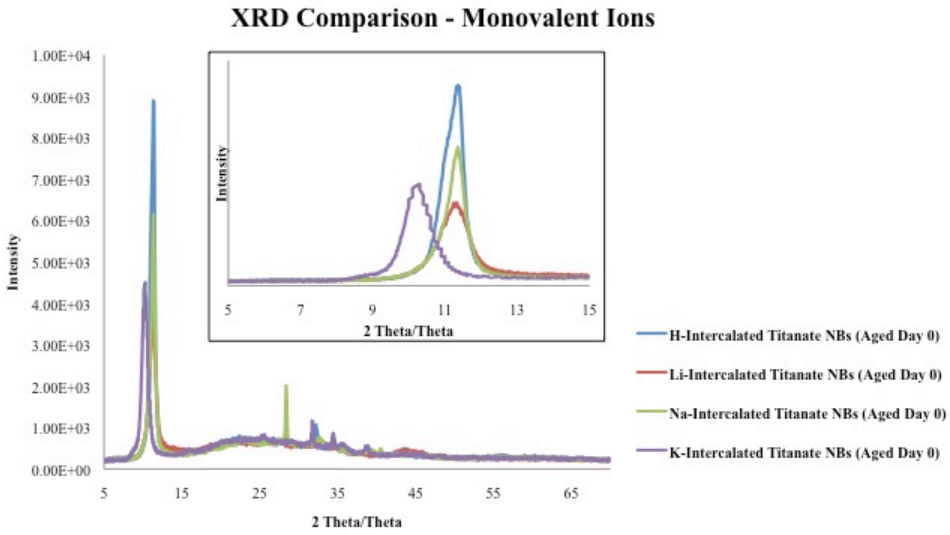

Figure 3.18: XRD Patterns of Monovalent Cations Intercalated Titanate NBs – Aged Day 0. (Inset: $d_{(001)}$ Peak)

Cation Used	$d_{(001)}$: 2θ (°)	(λ_{Cu}=2d sinθ) (Å)	(Å) ⇒nm
H^+	11.36	7.78	0.778
Li^+	11.32	7.81	0.781
Na^+	11.24	7.86	0.786
K^+	10.16	8.69	0.869

Table 3.1: XRD Data for Monovalent Cations Intercalation of $d_{(001)}$ Titanate NBs – Aged Day 0

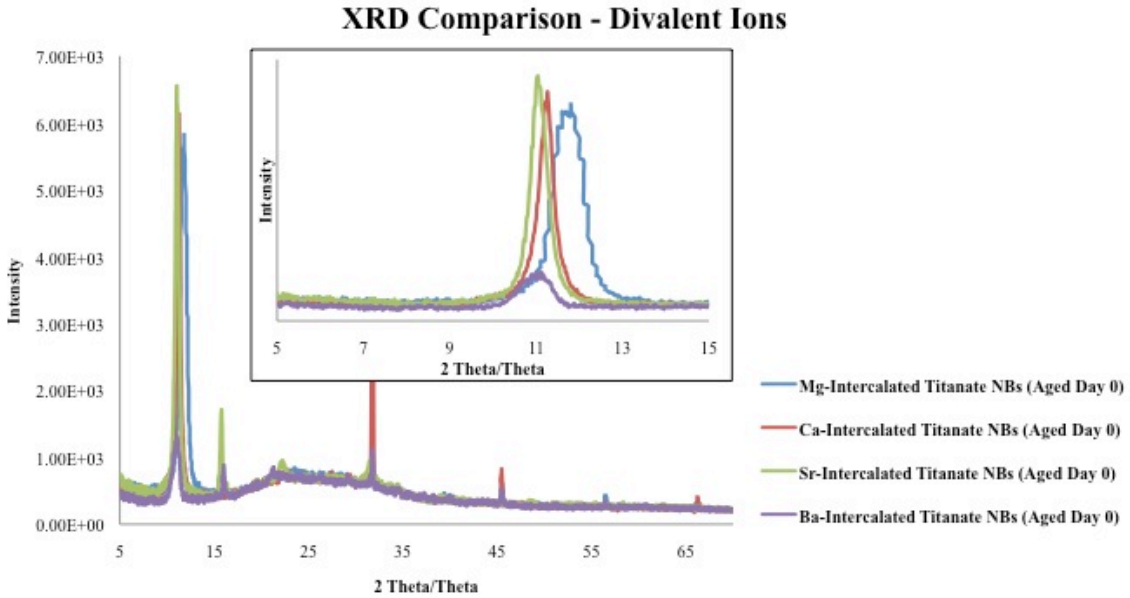

Figure 3.19: XRD Patterns of Divalent Cations Intercalated Titanate NBs – Aged Day 0. (Inset: $d_{(001)}$ Peak)

Cation Used	$d_{(001)}$: 2θ (°)	(λ_{Cu}=2d sinθ) (Å)	(Å) ⇒nm
Mg^{2+}	11.80	7.49	0.749
Ca^{2+}	11.26	7.85	0.785
Sr^{2+}	11.02	8.02	0.802
Ba^{2+}	10.09	8.76	0.876

Table 3.2: XRD Data for Divalent Intercalation Comparison of $d_{(001)}$ Titanate NBs – Aged Day 0

Ionic diameters versus interlayer d-space are represented in figures 3.20 (e.g. monovalent cations) and 3.21 (e.g. divalent cations). The ion exchanged NBs increased in the d-space trends in line with the cation diameters aqueous formation (Li^+ = 0.152 nm < Na^+ = 0.204 nm) [147, 148]. However, the d-space for each monovalent and divalent ion intercalated does not elicit the propensity for the hydrated cation radii form (Li^+ = 0.600 nm > Na^+ = 0.450 nm) [147, 148]. This seems to suggest that the non-hydrated forms of the ions dominate the interlayer matrix.

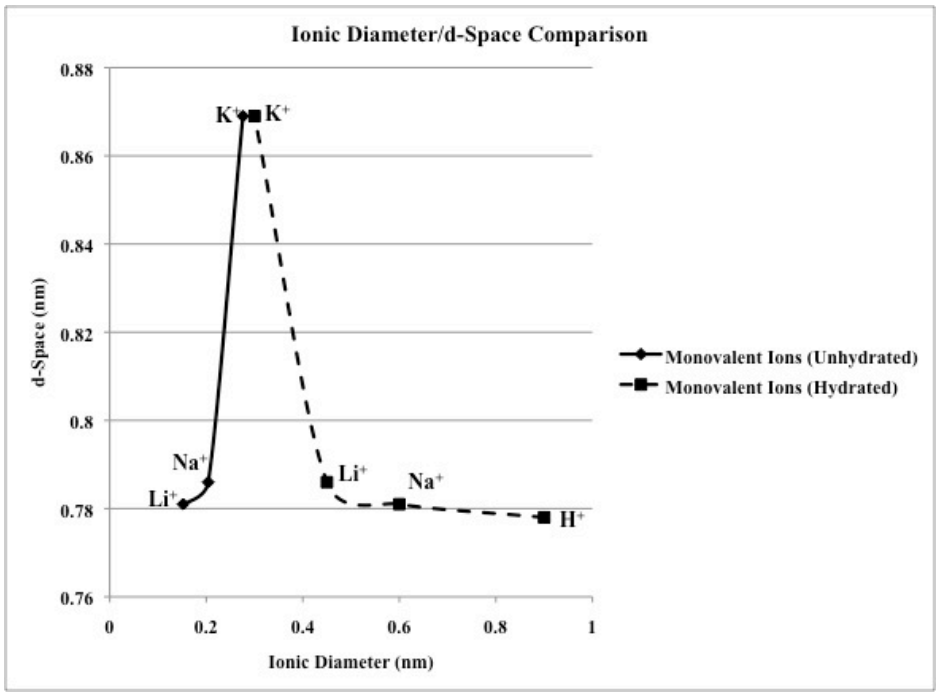

Figure 3.20: Ionic Diameters and d-Spaces of Monovalent Cations

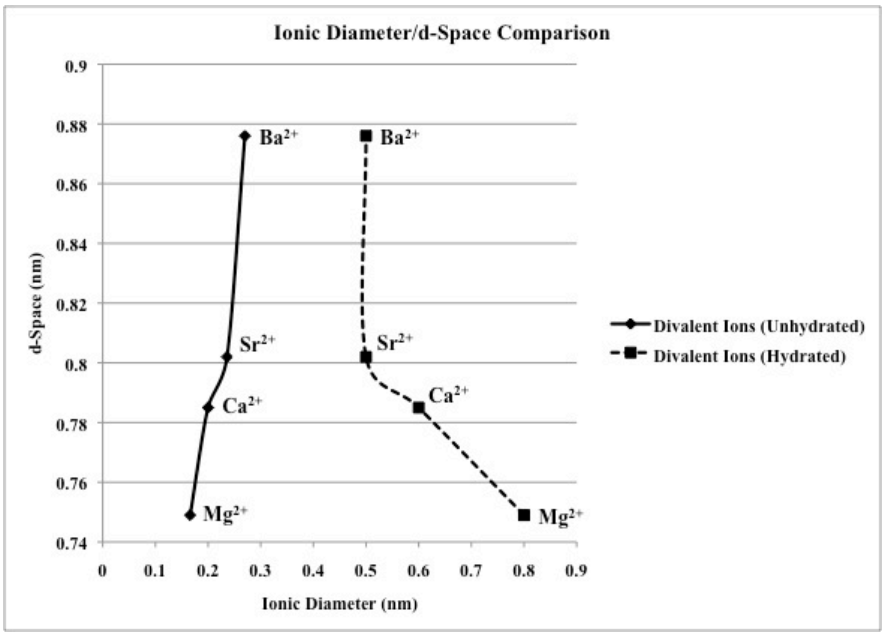

Figure 3.21: Ionic Diameters and d-Spaces of Divalent Cations

Futhermore, using a washing technique employing 1M solution of sodium chloride, followed by stirring the resulting material in a 1M aqueous solution of ionic salt for a period of three days, proper intercalation can be yielded under room temperature conditions. Following

this directive, the next intercalation trials will progress using 30-day aged material to observe any changes the additional ripening offers to the intercalation of the titanate NBs. These results are further examined in figures 3.22 through 3.23. The d-space is summarized in tables 3.3 and 3.4.

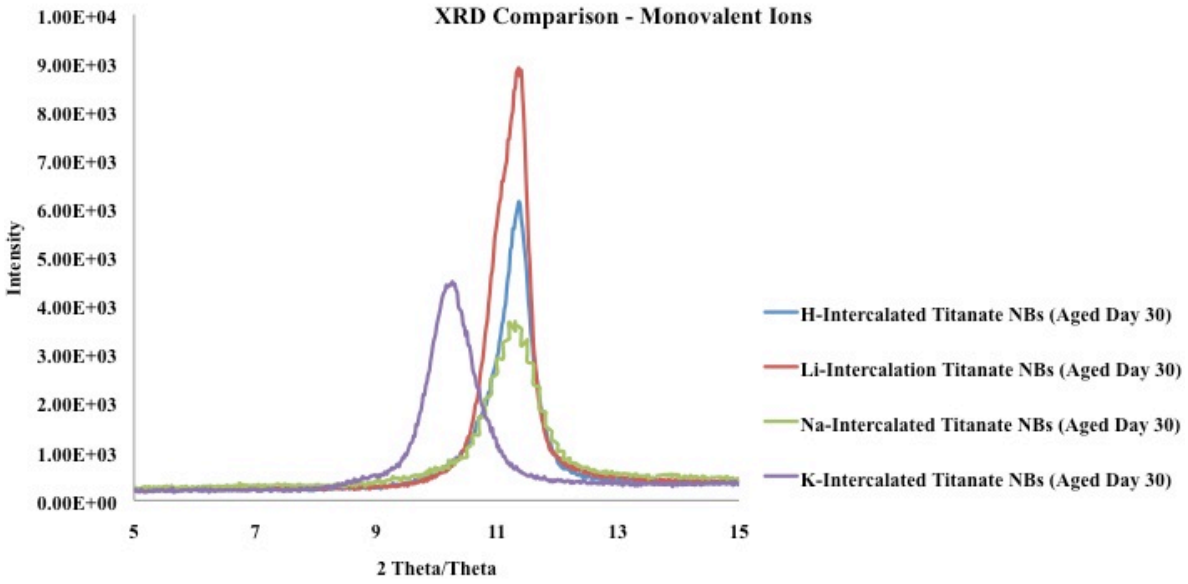

Figure 3.22: XRD Patterns ($d_{(001)}$) of Monovalent Cations Intercalated Titanate NBs – Aged Day 30

Cation Used	$d_{(001)}$: 2θ (°)	(λ_{Cu}=2d sinθ) (Å)	(Å) ⇒nm
H^+	11.50	7.68	0.768
Li^+	11.32	7.81	0.781
Na^+	11.20	7.89	0.789
K^+	10.12	8.73	0.873

Table 3.3: XRD Data for Monovalent Intercalation Comparison of $d_{(001)}$ Titanate NBs – Aged Day 30

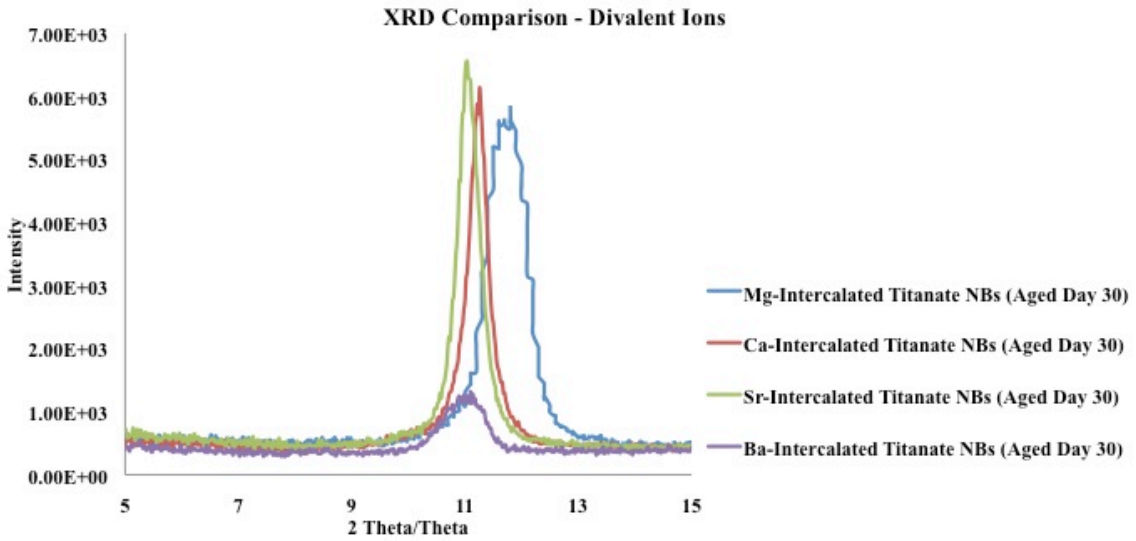

Figure 3.23: XRD Patterns ($d_{(001)}$) of Divalent Cations Intercalated Titanate NBs – Aged Day 30

Cation Used	$d_{(001)}$: 2θ (°)	(λ_{Cu}=2d sinθ) (Å)	(Å) ⇒nm
Mg^{2+}	11.70	7.55	0.755
Ca^{2+}	11.26	7.85	0.785
Sr^{2+}	11.02	8.02	0.802
Ba^{2+}	10.94	8.08	0.808

Table 3.4: XRD Data for Divalent Intercalation Comparison of $d_{(001)}$ Titanate NBs – Aged Day 30

As previously stated, the cation exchanged NBs also increased in the d-space trends in line with the anhydrous cation-diameters (Li^+ = 0.152 nm < Na^+ = 0.204 nm) [147, 148]; as well as, the d-space for each monovalent and divalent cation intercalated does no elect the hydrated radii (Li^+ = 0.600 nm > Na^+ = 0.450 nm) [147, 148]. Thus, the further growth continues the same results to the non-hydrated form as well.

Further investigation of the SEM aging results, yielded similar results. To ensure that the aging procedure coupled with the updated washing protocol did not bestow structural defects to the longitudinal surface, further analysis was performed (e.g. field emission scanning electron microscopy – FESEM). The FESEM results comparing all intercalated species of both Day 0 and Day 30 samples are shown in figures 3.24 through 3.31.

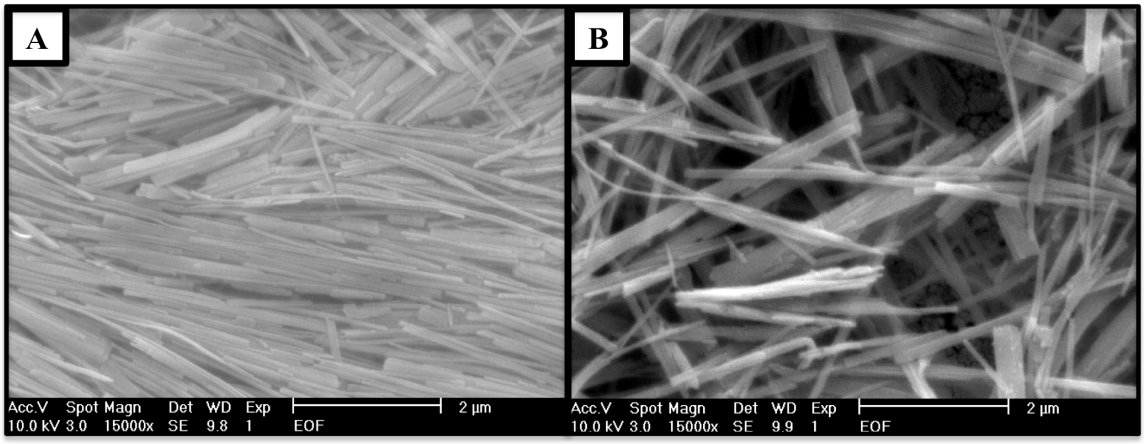

Figure 3.24: FESEM Images of Proton Intercalated Titanate NBs (Scale Bar: 2 µm): (A) Aged Day 0, (B) Aged Day 30

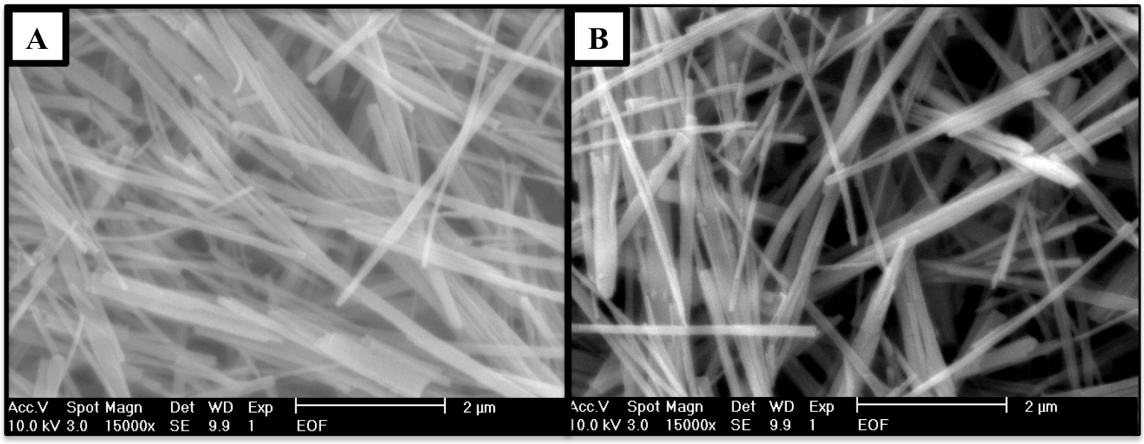

Figure 3.25: FESEM Images of Lithium Intercalated Titanate NBs (Scale Bar: 2µm): (A) Aged Day-0, (B) Aged Day-30

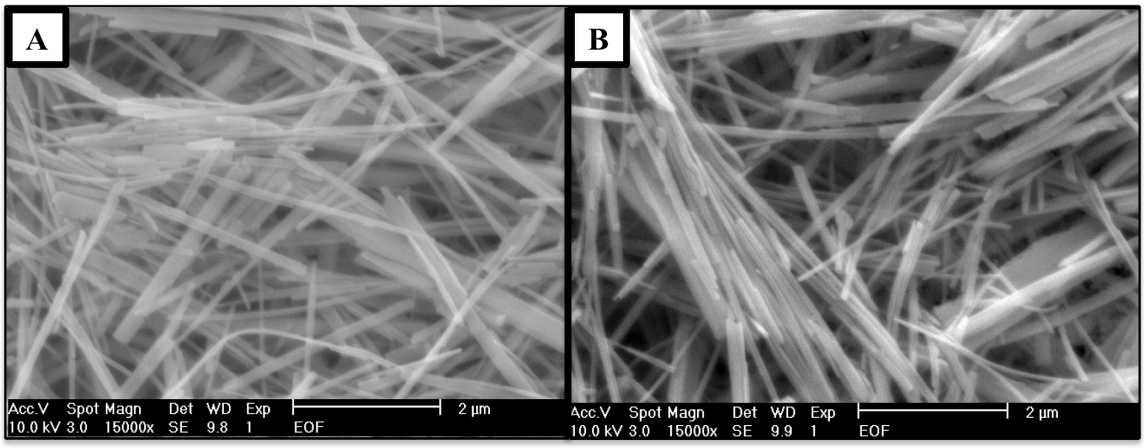

Figure 3.26: FESEM Images of Sodium Intercalated Titanate NBs (Scale Bar: 2µm): (A) Aged Day-0, (B) Aged Day-30

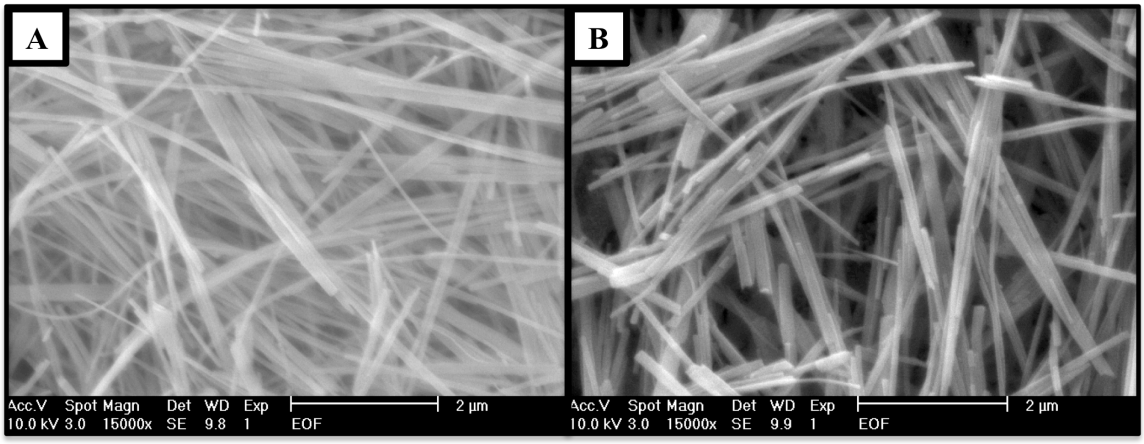

Figure 3.27: FESEM Images of Potassium Intercalated Titanate NBs (Scale Bar: 2µm): (A) Aged Day-0, (B) Aged Day-30

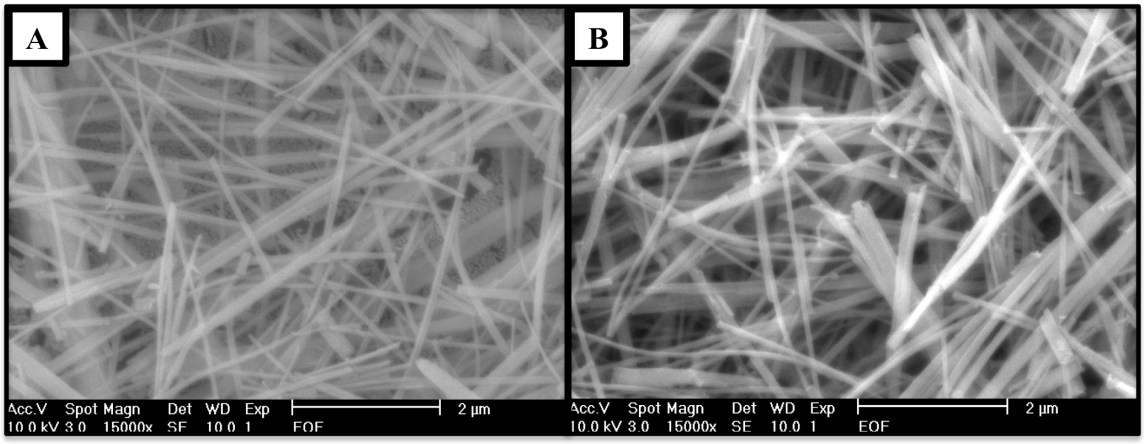

Figure 3.28: FESEM Images of Magnesium Intercalated Titanate NBs (Scale Bar: 2µm): (A) Aged Day-0, (B) Aged Day-30

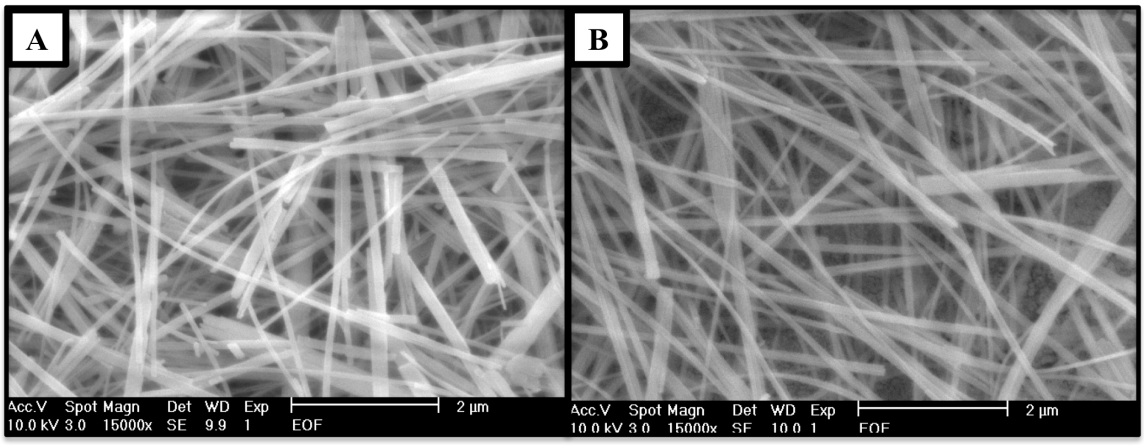

Figure 3.29: FESEM Images of Calcium Intercalated Titanate NBs (Scale Bar: 2µm): (A) Aged Day-0, (B) Aged Day-30

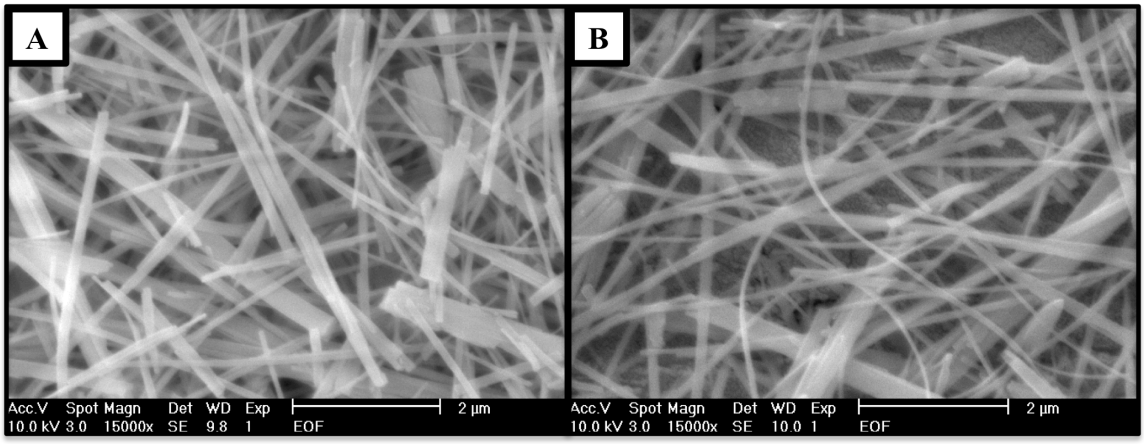

Figure 3.30: FESEM Images of Strontium Intercalated Titanate NBs (Scale Bar: 2µm): (A) Aged Day-0, (B) Aged Day-30

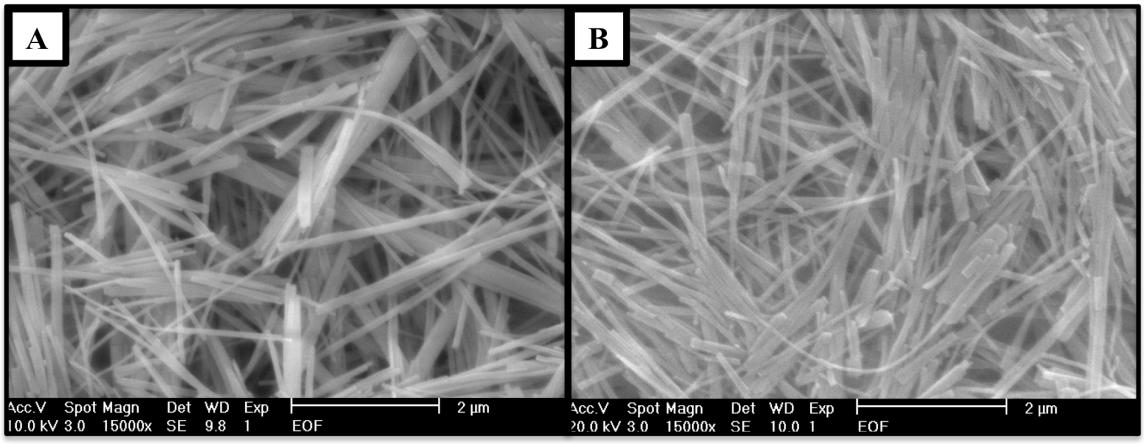

Figure 3.31: FESEM Images of Barium Intercalated Titanate NBs (Scale Bar: 2µm): (A) Aged Day-0, (B) Aged Day-30

From the FESEM results, no apparent structural alterations in the NB structure have been noted from a visual inspection. However, by allowing the H^+-intercalated titanate NB sample to stand for 30 days, full removal of all sodium ions was obtained without disruption of the main form NBs, as shown in figure 3.32, table 3.3, and figure 3.12.

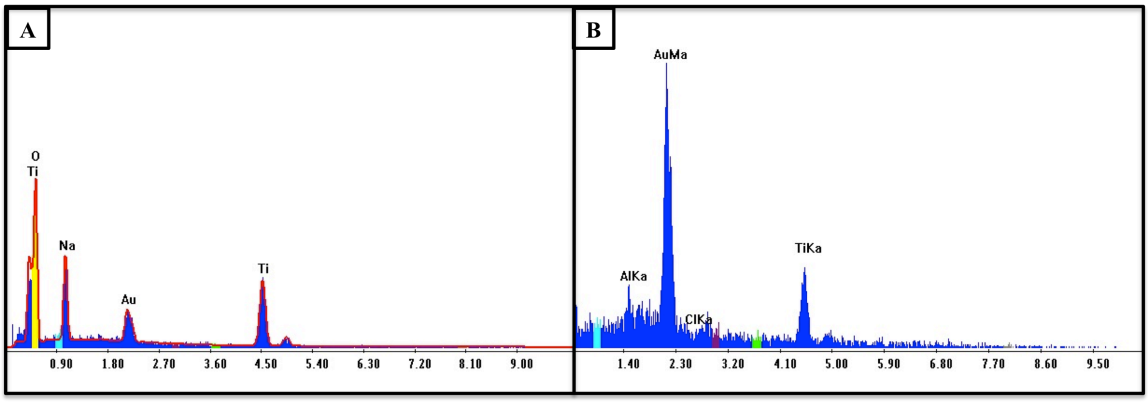

Figure 3.32: EDX Results of Proton Intercalated Titanate NBs Comparison: (A) Aged Day 0, (B) Aged Day 30

H-Titanate NBs Elemental Results	Wt% Day 0	Wt% Day 30
O	38.483	52.065
Na	12.040	0
Ti	49.477	47.935

Table 3.5: EDX Data of Titnate NBs Aging Comparison - (H^+) Intercalation

These results demonstrate that using the controlled NaCl washing technique allows for successful intercalation of the proton without the presence of the surface defects.

However, this effect has not been limited to the protanated form. When comparing to the EDX results between other cations and aging schemes, it seems that the interlayer space harbors an increased overall presence of guest-intercalated cations. These results are further described in tables 3.6 through 3.9.

K-Titanate NBs Elemental Results	Wt% Day 0	Wt% Day 30
Na	11.482	8.204
K	0.786	2.229

Table 3.6: EDX Data of Titnate NBs Aging Comparison – (K^+) Intercalation

Mg-Titanate NBs Elemental Results	Wt% Day 0	Wt% Day 30
Na	9.703	9.064
Mg	0.657	1.073

Table 3.7: EDX Data of Titnate NBs Aging Comparison – (Mg^{2+}) Intercalation

Ca-Titanate NBs Elemental Results	Wt% Day 0	Wt% Day 30
Na	10.464	8.821
Ca	0.960	2.61

Table 3.8: EDX Data of Titanate NBs Aging Comparison – (Ca^{2+}) Intercalation

Ba-Titanate NBs Elemental Results	Wt% Day 0	Wt% Day 30
Na	10.286	12.546
Ba	0.174	1.288

Table 3.9: EDX Data of Titanate NBs Aging Comparison – (Ba^{2+}) Intercalation

3.2. Improved Fabrication of Titanate NB Membranes

3.2.1. Large Size H^+-Intercalated Titanate NB Membrane

In previous attempts from this group, only small diameter membranes (< 50.00 cm^2) have been possible. However, utilizing the previously described additional stirring during titanate NBs synthesis, sufficient aging afterwards, and finally the NaCl washing procedure dictated through the intercalation process, the fabrication of larger area titanate NB membranes (≅ 613.12 cm^2) has been successfully achieved.

Although all intercalated forms have been easily achieved at both small and large-sized fabrication protocols, only the proton-intercalated form has been selected for further analysis due to fuel cell applications. The fabrication results are further depicted in figures 3.33 through 3.35.

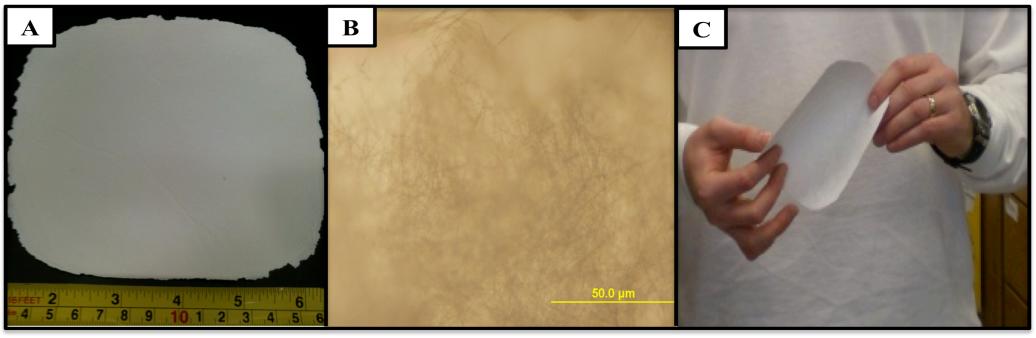

Figure 3.33: Photographs of Large-Size H^+-Titanate NB Membranes: (A) As Fabricated (Scale Bar: inch), (B) Optical (Scale Bar: 50 µm), (C) Flexibility Results

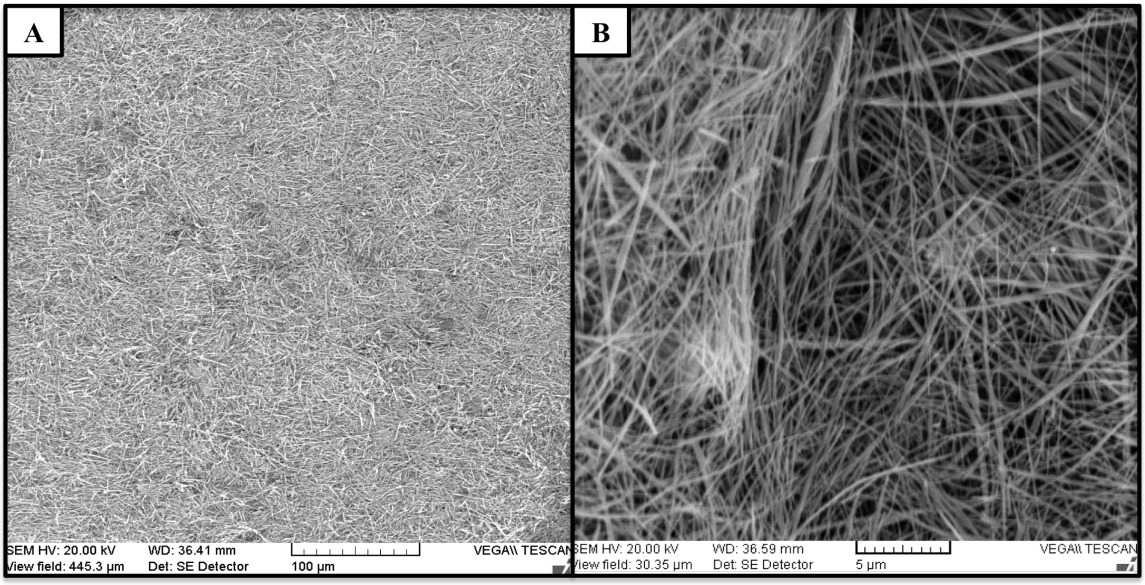

Figure 3.34: Large-Size H^+-Intercalated Titanate NB Membrane Center. (A) Distal View (Scale Bar: 100 µm), (B) Close Up View (Scale Bar: 5 µm)

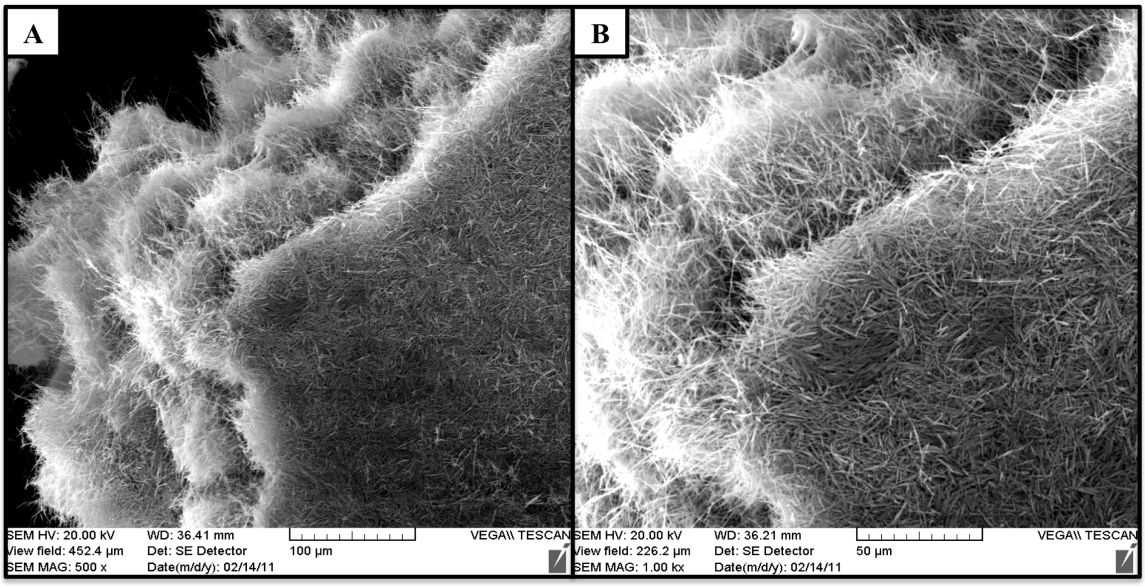

Figure 3.35: Large-Size H^+-Intercalated Titanate NB Membrane – Outside Edge. (A) Distal View (Scale Bar: 100 µm), (B) Close Up View (Scale Bar: 50 µm)

Additionally, we observed that a membrane thickness could be successfully controlled by the amount of intercalated titanate material in the fabrication process. Simply through using a larger amount of the product a more robust membrane can be created without the use of any

binder agents. However, a thicker membrane produced in this manner became overly brittle to the touch indicating issues with mechanical strength.

As previously discussed, the single layer membrane proton-intercalated form of the titanate membrane yielded the best quality, thus, it was selected for further investigation in ion conductivity studies. The overall thickness of the membrane examined was ~ 0.15 mm. Unfortunately, the freestanding form had significant structural issues around the edging when secured in the ion conductivity test chamber. Thus, a methodology of imbuing the material with a hydrophobic surface regulated to a specific area (i.e. edge) needed to be accomplished to ensure ionic conductivity properties of the titanate NB membrane could be determined.

3.2.2. Samples of Functionalized Titanate NB Membranes.

Chemically modifying the surface of the titanate membrane will aid in altering not only the hydrophobicity but perhaps in the future allow it to be tagged with various biomarkers. The three trials indicated various improvements to the surface-functionalization process.

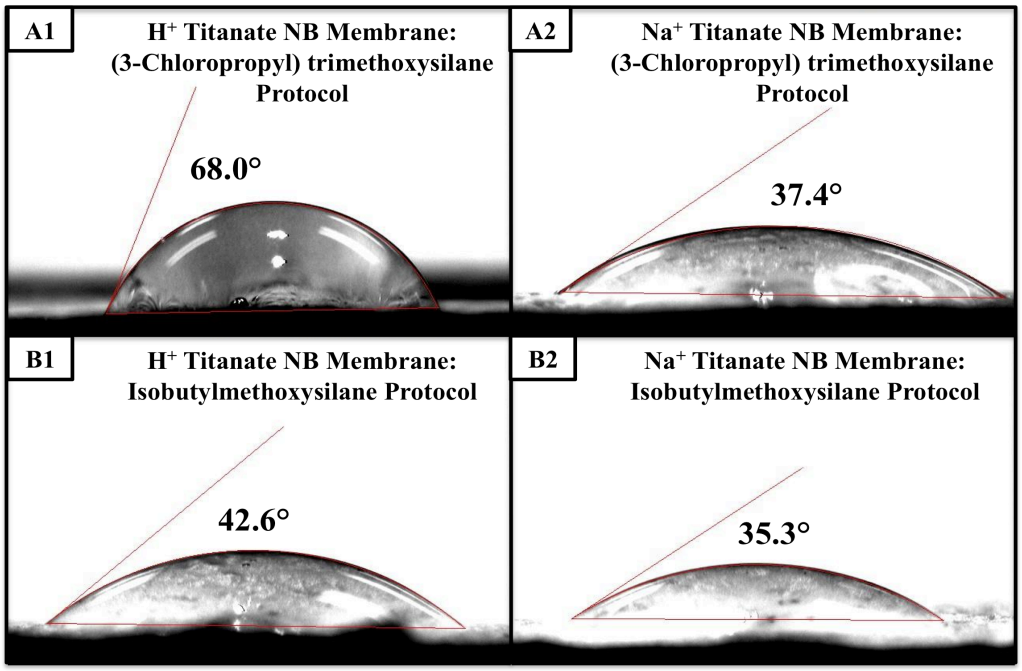

Figure 3.36: Contact Angle Micrographs of Surface-Functionalized NB Membranes

Trial one, results depicted in figure 3.36 (A1) and (A2), indicated that the protonic titanate in the soaked in the (3-Chloropropyl) trimethoxysilane yielded the best results in hydrophobicity with a contact angle measurement of 68.0˚. The other titanate samples in the sodium form did not retain the drop very long after exposure (less than a minute); therefore, could not be evaluated by the equipment at hand. The protonic forms of both functionalizations however did retain the drop for greater than five minutes before completely disappearing.

Utilizing the results from trial one, (3-Chloropropyl) trimethoxysilane was selected for further functionalization of the proton titanate membrane via under mild heating. The scheme is shown in figure 3.37 (A), and the hydrophobicity results of the examination are shown in figure 3.37.

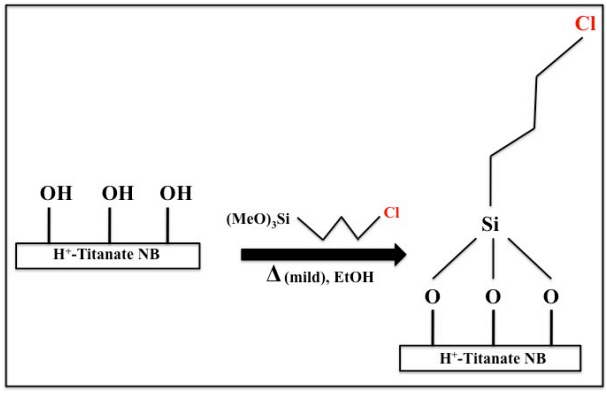

Figure 3.37 (I): Scheme for the Surface Functionalization

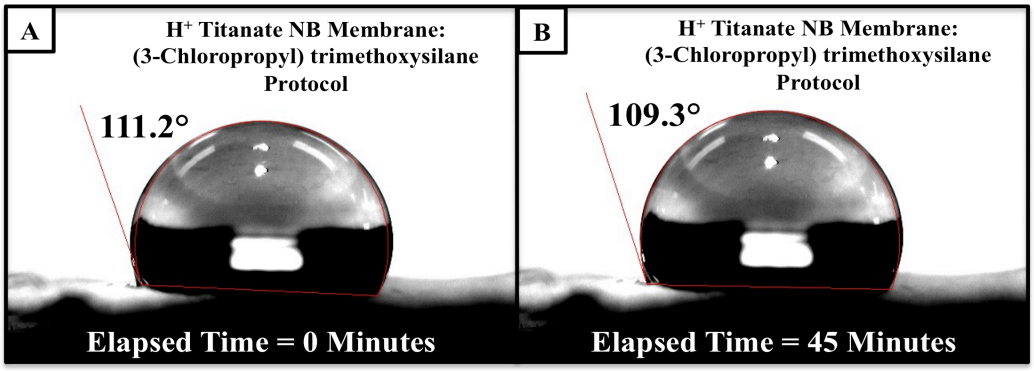

Figure 3.37(II): Contact Angles Micrographs for Surface-Functionalized NB Membranes – Timed Study (A) Time = 0 Minutes, (B) Time = 45 Minutes

These results indicate that the samples exhibited a stronger hydrophobic ability than those previously tested. This is seen by a contact angle measurement of 111.2˚ in figure 3.37 (A). As represented by this comparison figures, a time scale investigation was also performed to see if the hydrophobicity seen at time zero could be held for a longer amount of time, which was accomplished. At a time of 45 minutes, the contact angle resides at 109.30˚ in figure 3.37 (B). This indicates that functionization of our material is possible under mildest of conditions.

This methodology was further successfully utilized on both unpressed and pressed titanate membranes using the homemade functionaliztion chamber depicted in figures 2.4 through 2.7. Furthermore, the procedure allowed both membrane types to be further analyzed through ionic conduction without the drawback of structural breakdown around the membrane edging due to the aqueous environment of the test chamber.

3.2.3. Ionic Conductivity of the Freestanding Titanate NB Membranes.

Utilizing the test set up previously described in figure 2.8.4., the ion transport results are shown in figure 3.38 and table 3.10.

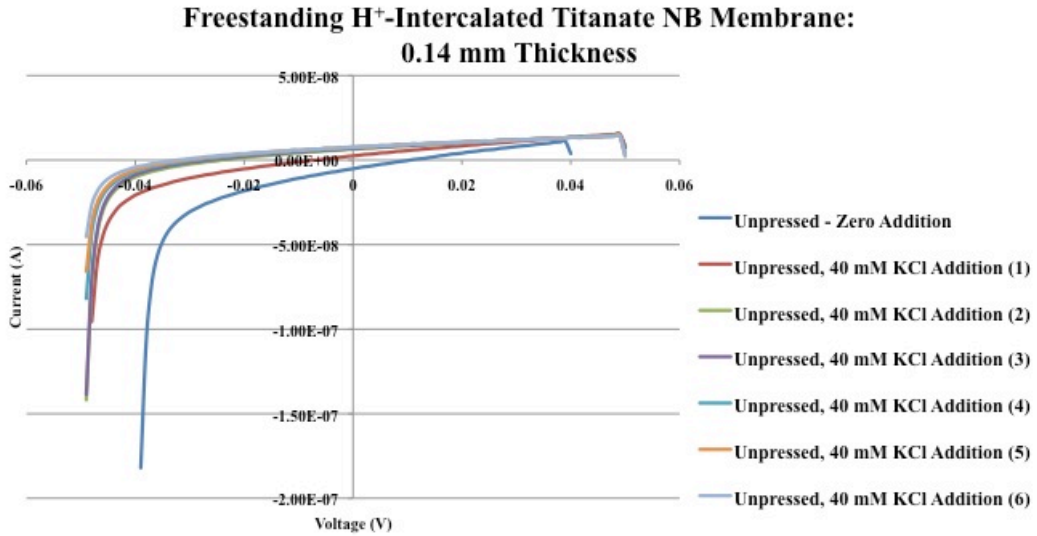

Figure 3.38: Ionic Conductivity for Freestanding H^{+}-Intercalated Titanate NBs Membranes

Addition	Transmembrane Voltage (mV)
Zero	7
1st Addition, 40 mM KCl	24
2nd Addition, 40 mM KCl	27
3rd Addition, 40 mM KCl	29
4th Addition, 40 mM KCl	31
5th Addition, 40 mM KCl	32
6th Addition, 40 mM KCl	32

Table 3.10: Transmembrane Voltage Data of Freestanding H^+-Intercalated Titanate NB Membranes

These results indicate the titanate membrane form does indeed conduct ions in the concentration cell developed. However, the low slope of the data is indicative of a lack of ease of transfer through the membrane. Also, the concentration cell had become over saturated, as the results of the stabilized transmembranve voltage generated seem to suggest. Unfortunately, upon retesting the single titanate it became apparent that despite the functionalization around the outer edge of the membrane, the center had severe delamination issues. Due to this significant problem, reproducibility of several of the ion transport studies was stymied. It was observed after the membrane resides in the test chamber for a short period of time in direct contact with an aqueous environment, the membrane seems to degrade.

As previously mentioned in section 1.7.2.1., current PEM technologies have 3 core responsibilities: (1) facilitate ion conduction, (2) offer thermal stability, and (3) offer resistance to both electrons and gas crossover. Using this membrane does offer proper free flow ion conduction albeit temporary. It also offers great thermal stabilities and shunts the passages of electrons. However, due to the pore size this particular membrane offers, it does not offer resistance to gas crossover. The fundamental reason for this is due to the loose formation of the NBs within the membrane.

Although this slack form cannot be directly observed from the center of the membrane, as depicted in the SEM picture in figure 3.34; however, it can be scrutinized in figure 3.35,when

concentrating on the outside edge of the membrane. Furthermore, it seems from the vantage point given in figure 3.35 that during the formation of the titanate membrane the NBs formed a multitude of layers. Unfortunately, the stratum abundance does not afford much stability while under the constraints of the aqueous examination environment. However, further fabrication processing of the titanate membrane may correct this issue.

3.2.4. Pressed Titanate NB Membrane: Fabrication Progress

In order to address this loose formation issue, two separate presses were constructed, previously described in figure 2.3, to be used to form two sizes of tightly packed membranes. The process using the press to develop a tighter membrane is summarized in figure 2.3(C). So as to check the effectiveness for forming tightly packed layers of the titanate, the press was used by layering ten circular sections (12.7 mm diameter) of titanate into the device and pressed at five thousand pounds per square inch for five minutes. The resulting thickness of the pressed material is ~ 1.5 mm.

The membrane disk was then scrutinized on both the surface and a cross section, depicted in figure 3.39 (A & B). The cross-section seems to reinforce the previous observation made regarding figure 3.35. The amount of layers observed in the cross-section is vastly more than the ten used during construction, indicating multiple layers exist in a single membrane.

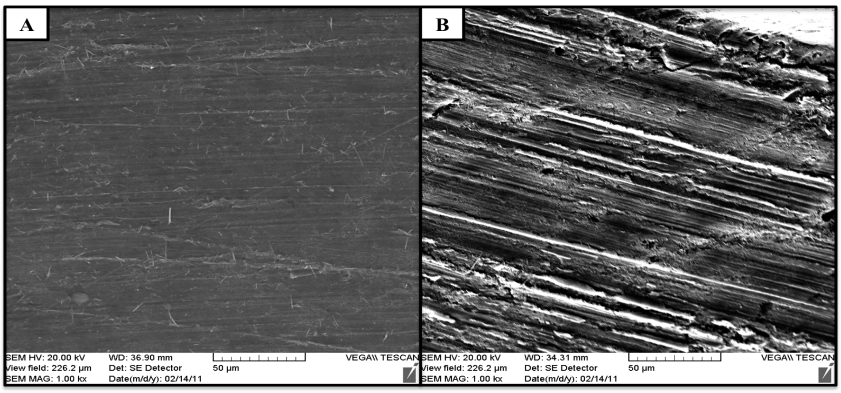

Figure 3.39: SEM Images of Pressed H^+-Intercalated Titanate Sample (Scale Bar: 50 µm): (A) Face On view, (B) Cross-sectional view

3.2.5. Ionic Conductivity of Pressed H^+-Intercalated Titanate NB Membrane

In the initial test with the pressed H^+-intercalated titanate Ns shown in figure 3.40 and table 3.11, it is apparent that upon each addition of potassium chloride to one side of the concentration cell that passage of potassium ions are occurring yielding a lower transmembrane voltage especially when compared to previous slopes in figure 3.38. These results indicate proton-intercalated titanate membranes produce the ability to transport monovalent cations despite different porosities within the membrane structure.

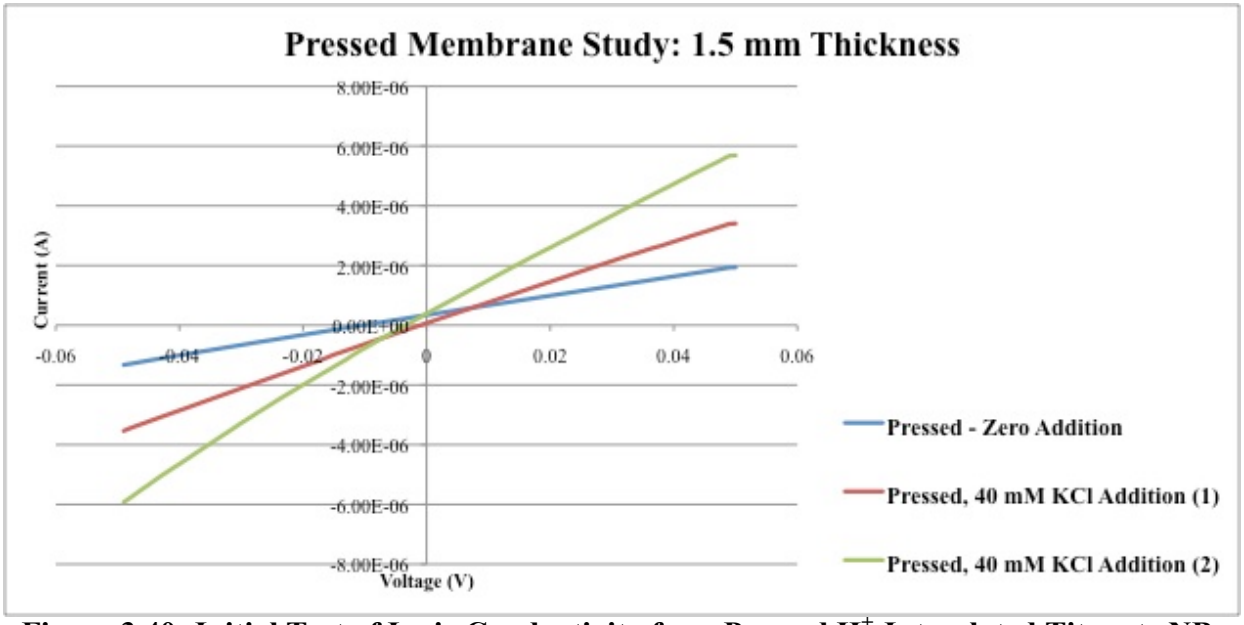

Figure 3.40: Initial Test of Ionic Conductivity for a Pressed H^+-Intecalated Titanate NB Membrane

Addition	Transmembrane Voltage (mV)
Zero	10
1st Addition, 40 mM KCl	1
2nd Addition, 40 mM KCl	4

Table 3.11: Initial Transmembrane Voltage Data of Pressed H^+-Intercalated Titanate NB Membranes

After 24 hours from the initial results, the pressed membrane was removed from the test chamber after the test from figure 3.40 had been completed. The reason for this was to visually

inspect the sample for any structural degradation for being in the cell for several hours. The sample had no apparent surface defects and while retaining rigidity throughout. The pressed sample was then cleaned thoroughly with distilled water, dried at 100°C for an hour, and replaced in the cell once it returned to room temperature.

The sample was then returned to the test chamber. The results from which are shown in figure 3.41 and table 3.12. These results indicate a lower generation of transmembrane voltage and generated current by the cell when compared to the single layer results; however, the stability increase has never been seen before now. The retest ability of this new fabrication process is now completely possible.

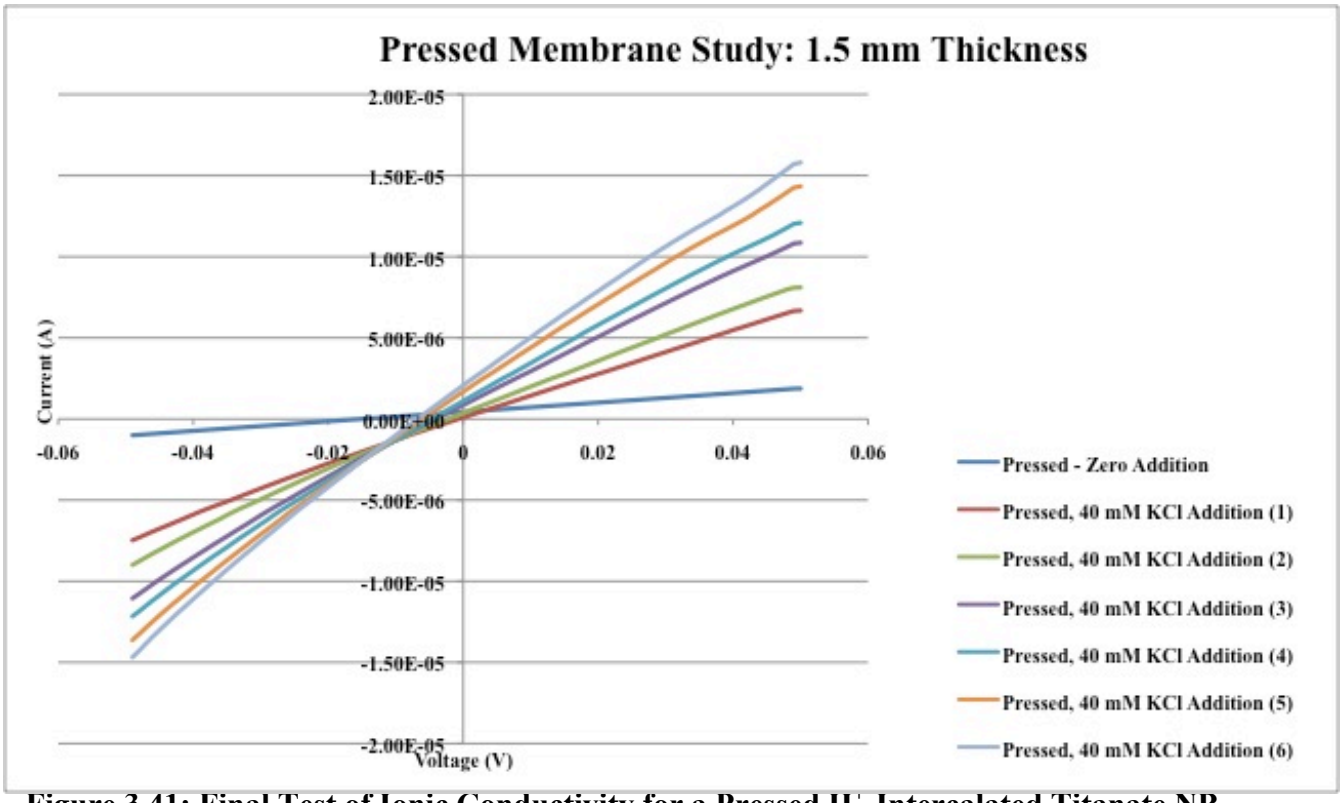

Figure 3.41: Final Test of Ionic Conductivity for a Pressed H⁺-Intercalated Titanate NB Membrane

Addition	Transmembrane Voltage (mV)
Zero	15
1st Addition, 40 mM KCl	1
2nd Addition, 40 mM KCl	2
3rd Addition, 40 mM KCl	4
4th Addition, 40 mM KCl	5
5th Addition, 40 mM KCl	7
6th Addition, 40 mM KCl	8

Table 3.12: Final Transmembrane Voltage Data of Pressed H^+-Intercalated Titanate NB Membranes

With the reduction of pore size gas crossover would indeed be reduced; however, the new fabricated form did exhibit some ionic conduction issues with time. It seems that although the thicker membrane yielded increased structural stability while in a prolonged aqueous testing environment, it took several minutes for the ion conduction to reach equilibrium. Thus, it seems that although the single layer has stability issues in the aqueous environment, it did harbor higher transmembrane voltages albeit short lived. Unfortunately, the ion conduction through the membrane is not ideal for the fuel cell applications. Thus, another methodology needs to be acquired to yield a titanate NB membrane that has ease of ionic conduction, high resistance to gas crossover and retaining a high thermal stability. The Nafion© titanate composite form may be the answer.

3.3. Nafion© Laminated Titanate NB Membrane

3.3.1. A New Fabrication

In order to address the structural stability issue in the aqueous environment, as well as to examine the imbuement of high thermal stability possibility to a polymer form, another membrane form was fabricated and examined. The laminated form of Nafion©/H^+ Intercalated Titanate NB membrane is depicted in figure 3.42.

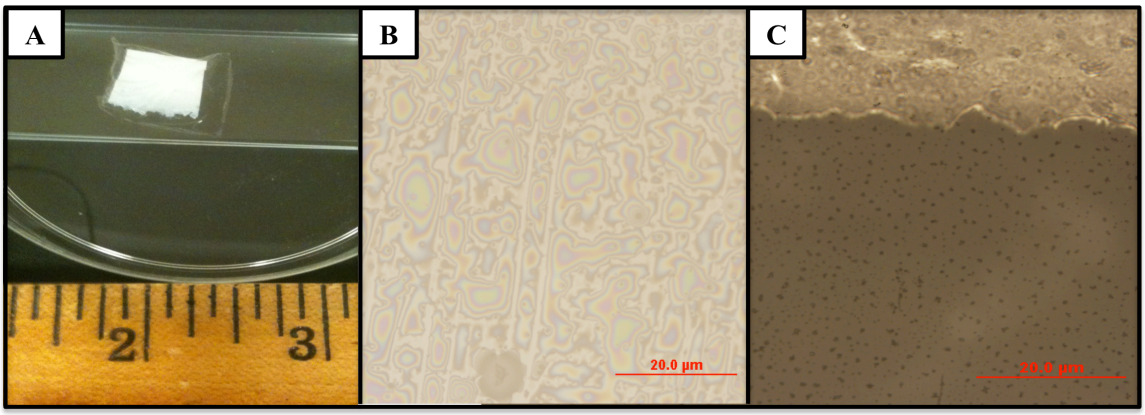

Figure 3.42: Photographs of Laminated Nafion©/H^+ Intercalated Titanate NB Membrane (A): Distal View (Scale Bar: inch), (B) Optical View: Face On View of Center of Membrane (Scale Bar: 20 µm), (C) Optical View: Outside Edge of Membrane (Scale Bar: 20 µm)

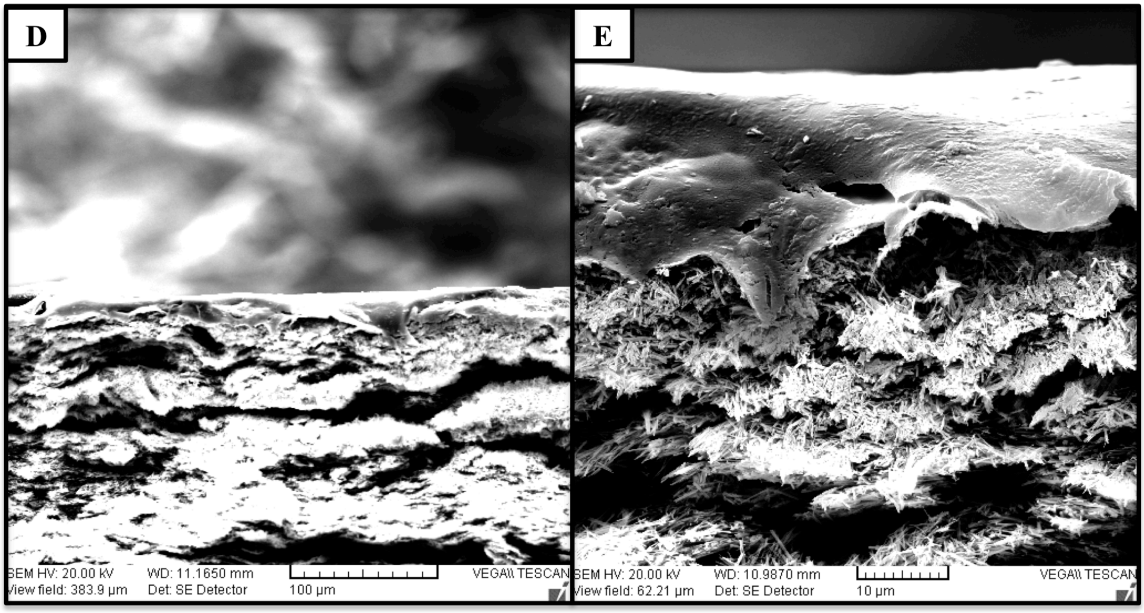

Figure 3.42: Laminated Nafion©/H^+ Intercalated Titanate NB Membrane (D) Cross Sectional View of Membrane Center (Scale Bar: 100 µm) (E) Cross Sectional View of Membrane Center (Scale Bar: 10 µm)

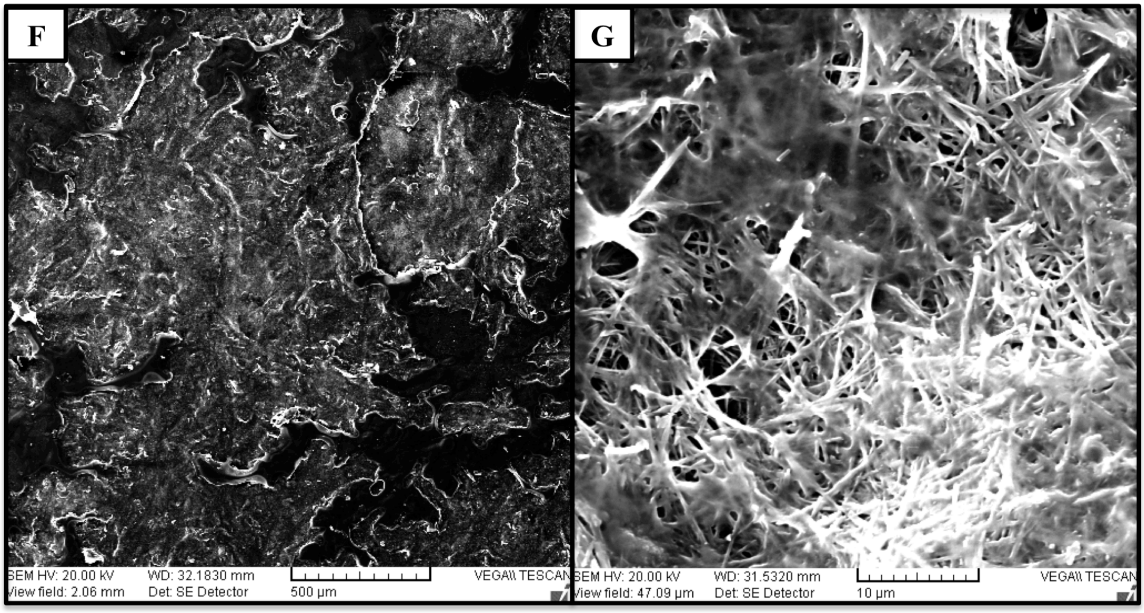

Figure 3.42: Laminated Nafion©/H^+ Intercalated Titanate NB Membrane
(F) Face On View of Membrane Center (Scale Bar: 100 µm)
(G) Face On View of Membrane Center (Scale Bar: 10 µm)

3.3.2. Ionic Conductivity of Nafion© Laminated H^+-Intercalated Titanate NB Membranes

Before analysis into the laminate forms accomplished, first the pure cast Nafion© membrane was examined. The casted Nafion© form possessed a thickness of 0.180 mm which is similar to established Nafion© 117 thickness primarily used in PEMFC applications.[149]

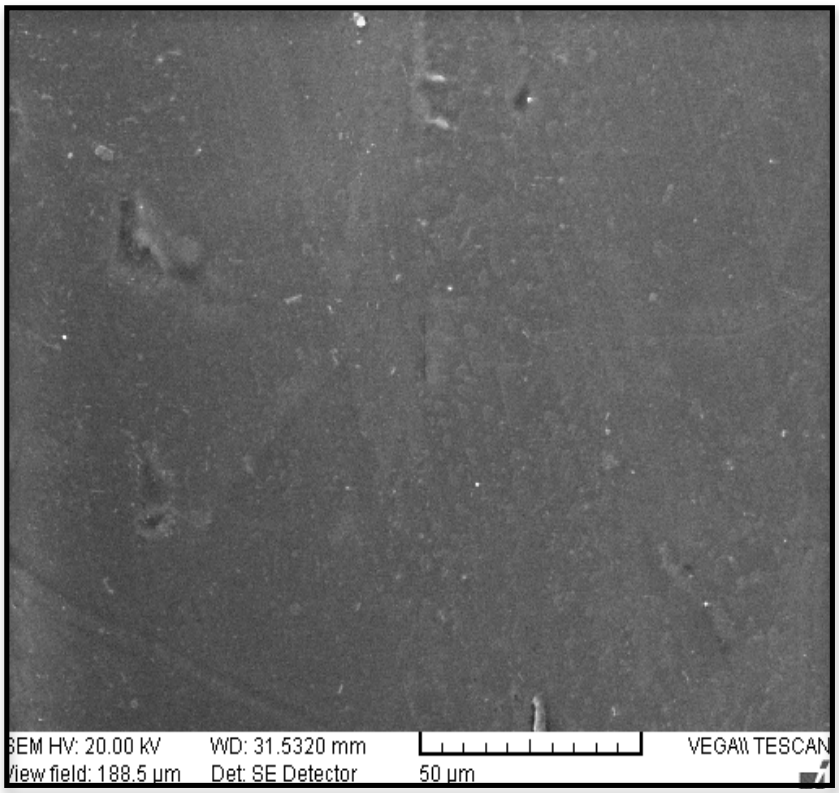

Figure 3.43 (A): Face On View of Casted Pure Nafion© Membrane Center (Scale Bar: 50 µm)

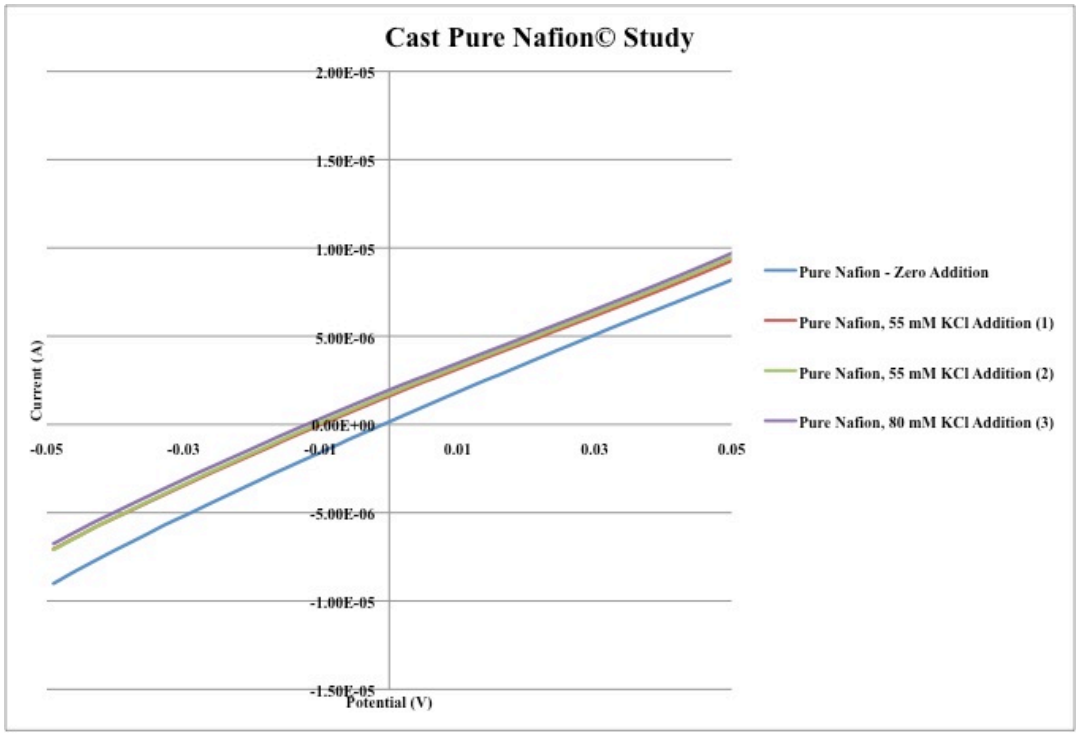

Figure 3.43 (B): Ionic Conductivity of Casted Pure Nafion© Membrane

Addition	Transmembrane Voltage (mV)
Zero	0
1st Addition, 55 mM KCl	9
2nd Addition, 55 mM KCl	10
3rd Addition, 80 mM KCl	11

Table 3.13: Transmembrane Voltage Data of Pure Nafion© Casted Membrane

In the ionic conductivity assessment depicted in figure 3.44 and table 3.14, the Nafion© laminate coating on the H^+-intecalated titanate NB membrane yielded sustainable transmembrane voltages without membrane breakdown when compared to the freestanding single layer results in figure 3.38.

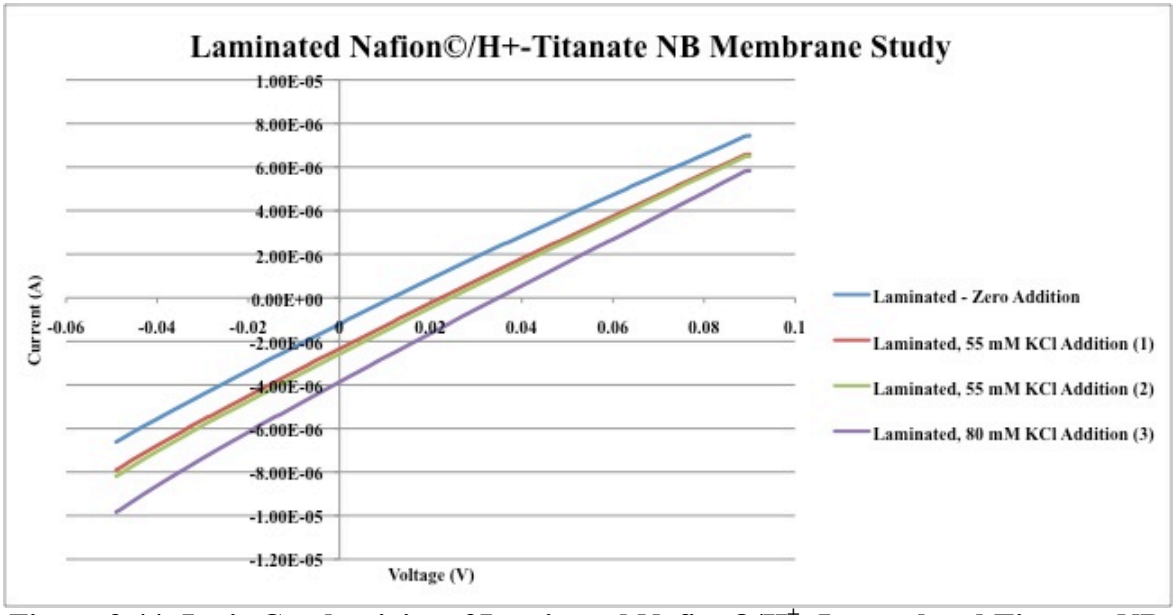

Figure 3.44: Ionic Conductivity of Laminated Nafion©/H^+- Intercalated Titanate NB Composite Membranes

Addition	Transmembrane Voltage (mV)
Zero	12
1st Addition, 55 mM KCl	23
2nd Addition, 55 mM KCl	25
3rd Addition, 80 mM KCl	35

Table 3.14: Transmembrane Voltage Data of Laminated Nafion©/H^+-Intercalated Titanate NB Membranes

When compared to the transmembrane voltages of the single layer titanate membrane of figure 3.38 or the laminate form in figure 3.44, the pure Nafion© does not register higher

transmembrane voltages shown in figure 3.43 and table 3.13; however, it does possess immediate ionic conduction and does not suffer the time equilibration issues previously mentioned in the pressed titanate NB membrane formation previously examined.

3.3.3. TGA Analysis of Nafion© Laminated H^+-Intercalated Titanate NB Membranes

The casted Nafion© and laminate H^+-intercalated titanate NB composite membranes were analyzed using TGA. The results follow in figure 3.45 (A) through (C).

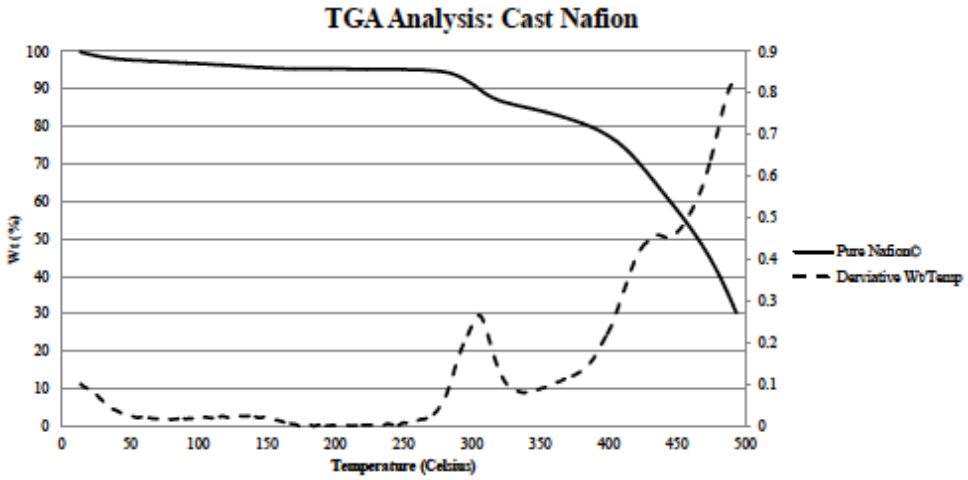

Figure 3.45 (A): TGA Results of Pure Casted Nafion© Membranes

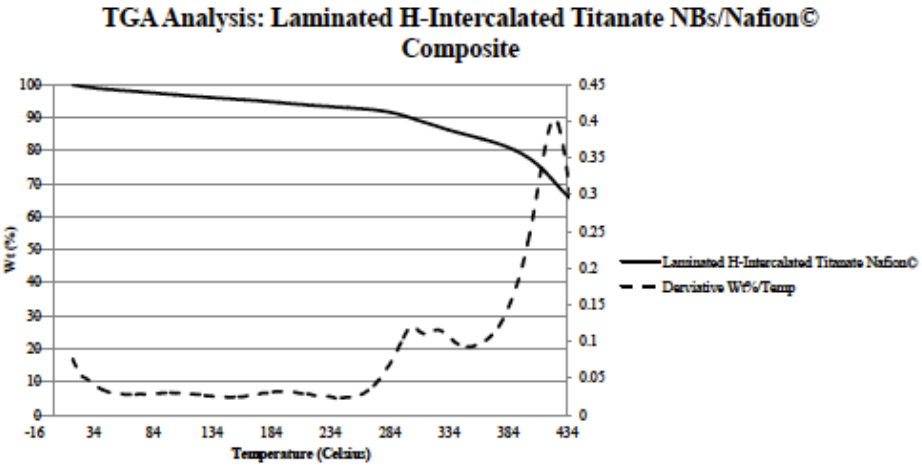

Figure 3.45 (B): TGA Results of Laminated Nafion©/H^+- Intercalated Titanate NB Membranes

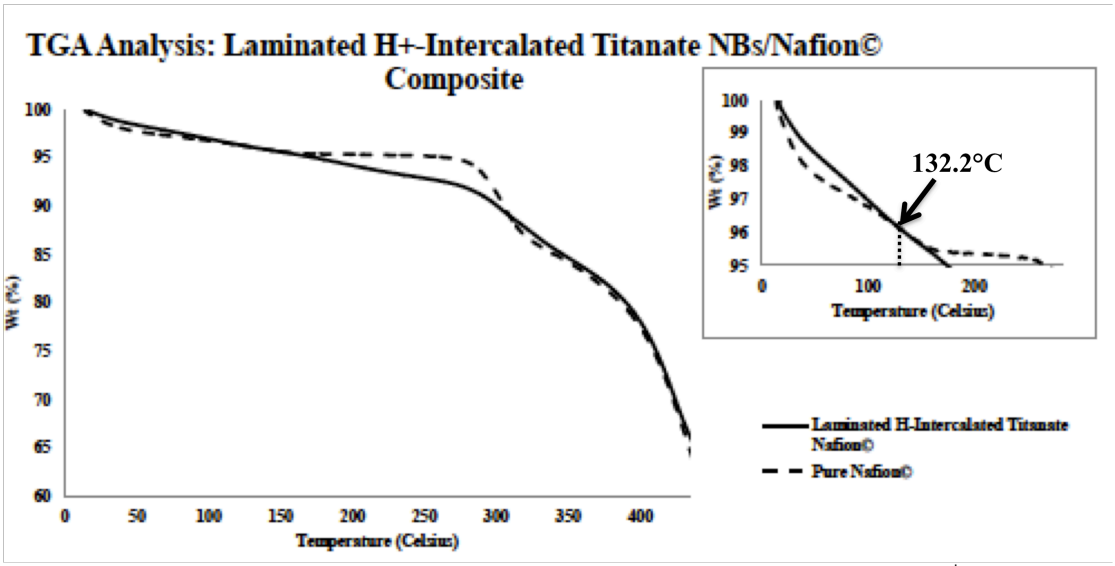

Figure 3.45 (C): TGA Results of Pure Nafion© vs Laminated Nafion©/H^+- Intercalated Titanate NBs Composite Membrane

In the cast form of Nafion© and the laminated composite, the initial mass loss until 150°C is attributed to removal of all adsorbed water molecules in the ion channels within the Nafion© matrix.[149] The secondary mass loss of Nafion© incurred in the range of 276°C to 308°C is principally due to losses within the sulfonic groups.[150, 151] The third mass loss at 330°C and greater is likely due to the oxidative degradation of the flouronated backbone structure as well as any remaining sulfonic moieties.[149-152]

As observed in figure 3.45(C), the laminated structure retains higher mass percentages up to 132.2°C, then it directs into the similar loss path as Nafion until 150°C. The higher mass percentages are likely because composite loading is so increased, it therby reduces the sulfonic group interaction. The secondary mass loss of the composite is lower then the Nafion© cast pure form; however when the progress tracks into the third mass loss of 330°C and higher, the composite retains at a slightly higher level. The thermal stability at this high level may be due to the sulfonic group protection within the composite filler layers, as observed in figure 3.42 (D) and (E). The composite material may allow several gaps in which may protect the protonated

sulfonic groups within the layers. The laminate Nafion©/H^+-intercalated titanate NB composite does offer thermal stability to mass reduction up to temperatures of ~ 110°C. Further thermal stability studies of the laminate composite are underway.

3.4. Nafion©/Titanate NB Blended Membrane Composites

3.4.1. Nafion©/Titanate NB 20% Blended Membrane Composites: Fabrication & Characerization

As observed in figure 3.46, the fabrication of the low composite formation (e.g. 20% composite) of the Nafion© /Titanate NBs was achieved.

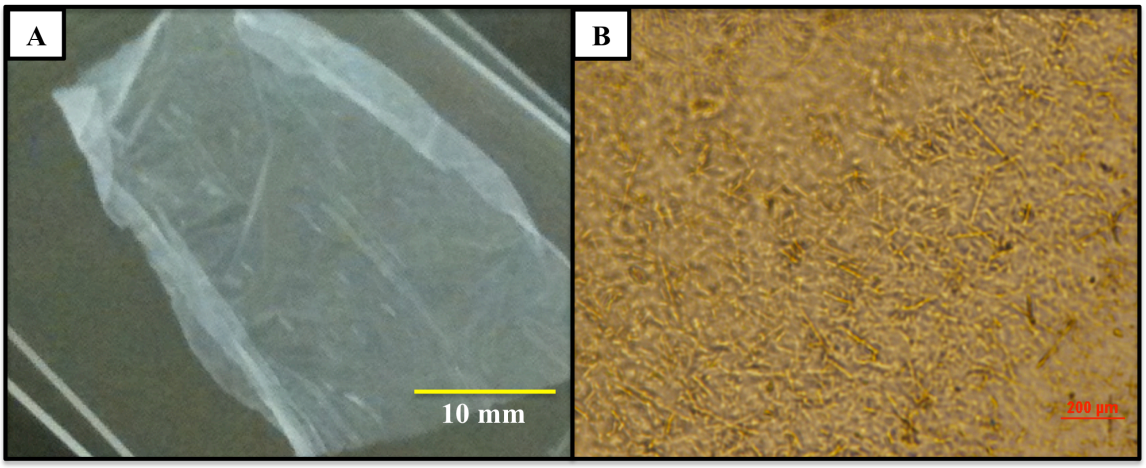

Figure 3.46: Nafion©/H^+- Intercalated Titanate NB 20% Blended Composite Membrane: (A) Photograph (Scale Bar: 10 mm), (B) Optical Face On View (Scale Bar: 200 µm)

The casting process was evaluated using pure Nafion© cast as a standard by which the rest of the data was further evaluated. The resulting membranes were then examined through XRD, depicted in figure 3.47. The XRD result indicates the casting process harbors a reduction in crystallinity upon addition of the composite material (H^+-intercalated titanate NBs).

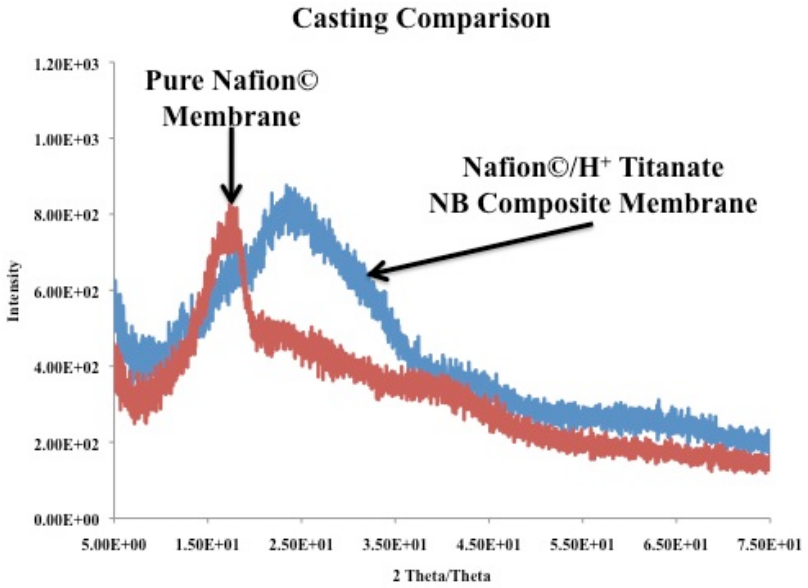

Figure 3.47: XRD Results of Casting Process Pure Nafion© vs. Nafion©/H^+- Intercalated Titanate NB 20% Blended Composite Membrane

3.4.2. Ionic Conductivity of Nafion©/Titanate NB 20% Blended Composite Membranes

The ion conductivity was also performed using the 20% Nafion©/H^+-intercalated titanate NB blended composite. As shown in figure 3.48 and table 3.15, the composite yielded slightly higher transmembrane voltages when compared to the pure Nafion© form shown in figure 3.43 and table 3.13. The ionic conductivity of the 20% blended composite possesses similar initial transmembrane voltage when compared to the laminated composite previously discussed in section 3.4.2; however, the test cell equilibration (e.g. zero addition) was vastly improved and manageable in 20% NB blended composite membrane formation.

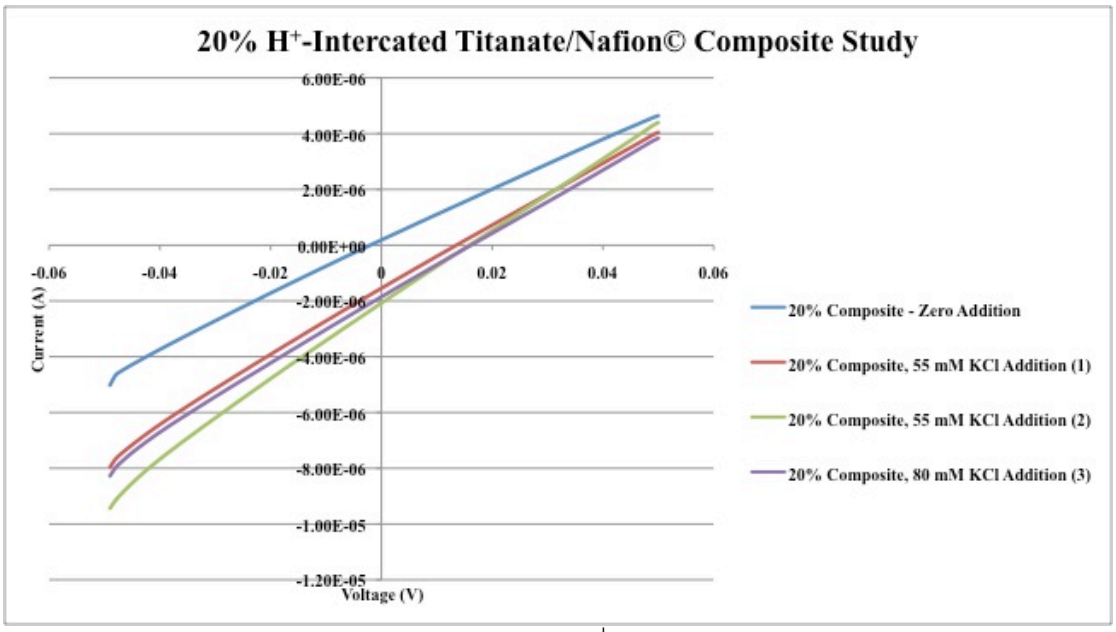

Figure 3.48: Ionic Conductivity of Nafion©/H^+-Titanate NB 20% Blended Composite Membrane

Addition	Transmembrane Voltage (mV)
Zero	1
1st Addition, 55 mM KCl	14
2nd Addition, 55 mM KCl	16
3rd Addition, 80 mM KCl	17

Table 3.15: Transmembrane Voltage Data of Blended Nafion©/H^+-Titanate NB 20% Blended Composite Membrane

3.4.3. Fabrication & Ionic Conductivity of Nafion© Blended Titanate NB High-content Form Composite Membranes

Up to now only low-level composite amounts of less than 25 percent have been successfully fabricated and evaluated for ionic conductivity and thermal stability. Herein it is reported for the first time the successful completion of the high-content composite (titanate NB:Nafion©) fabrication of 50:50, 100: 1, 150:1, and 200:1. The aforementioned composite spread is depicted in the photographs in figure 3.49.

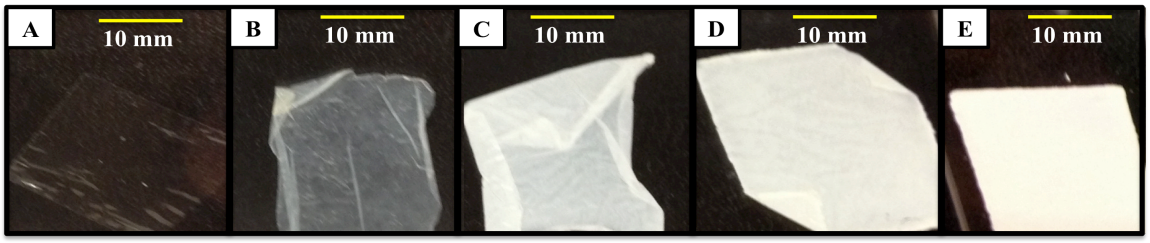

Figure 3.49: Photograph of H^+-Titanate NB/Nafion© Composite Membranes (Scale Bar: 10 mm): (A) Cast Pure Nafion©, (B) [50:50], (C) [100:1], (D) [150:1], (E) [200:1]

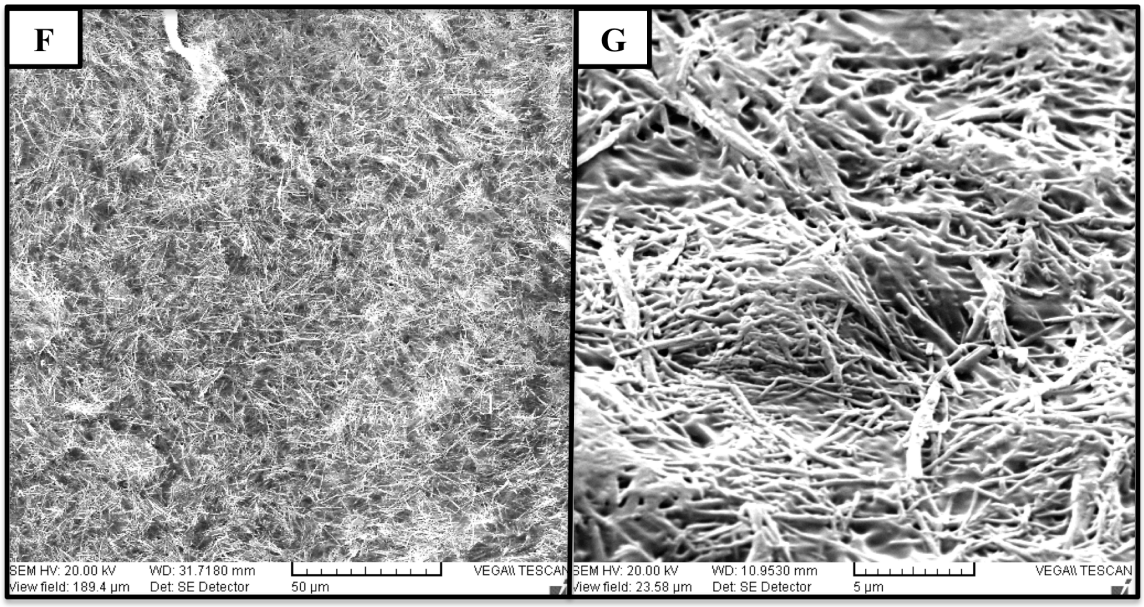

Figure 3.49 (F) & (G): SEM Images of H^+-Intercalated Titanate NB/Nafion© Blended [50:50] Composite Membrane Center:
(F) Face On View (Scale Bar: 50 µm), (G) Close Up View (Scale Bar: 5 µm)

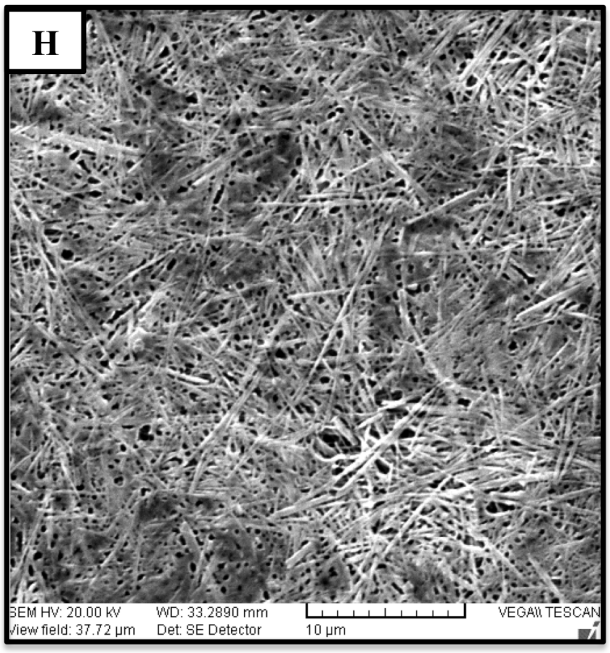

Figure 3.49 (H): SEM Image of H^+-Titanate NB/Nafion© 100:1 Blended Composite Membranes –Face On View of Center (Scale Bar: 50 µm)

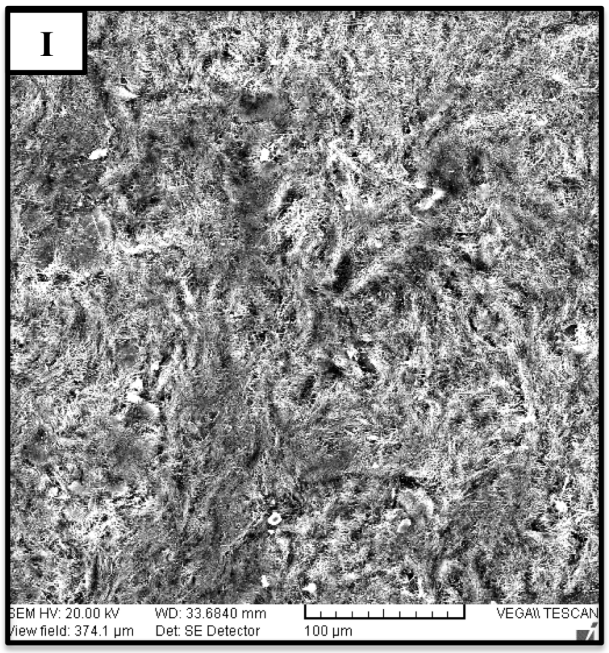

Figure 3.49 (I): SEM Image of H^+-Titanate NB/Nafion© 150:1 Composite Membranes – Face On View of Center (Scale Bar: 100 µm)

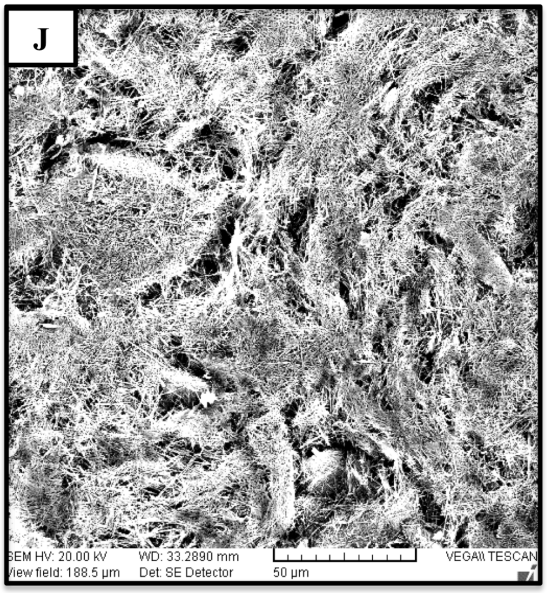

Figure 3.49 (J): SEM Image of H^+-Titanate NB/Nafion© 200:1 Blended Composite Membranes –Face On View of Center (Scale Bar: 50 µm)

Figure 3.49 indicates that although the load level increases and the Nafion© presence is reduced; the filler allows the connective anchoring ensuring the stability of the overall membrane. The highest filler composite thus far (200:1) fabricated yielded the best quality membrane to date. The two extremes (pure cast Nafion© 0 filler load and 200% filler loading) were chosen for further ionic analysis.

The results of which are established in figure 3.50 and table 3.16. From the data, it can be quickly observed that the transmembrane values have significantly increased using the overloaded titanate formation of the composite material when compared to the pure form (see figure 3.43 and table 3.13).

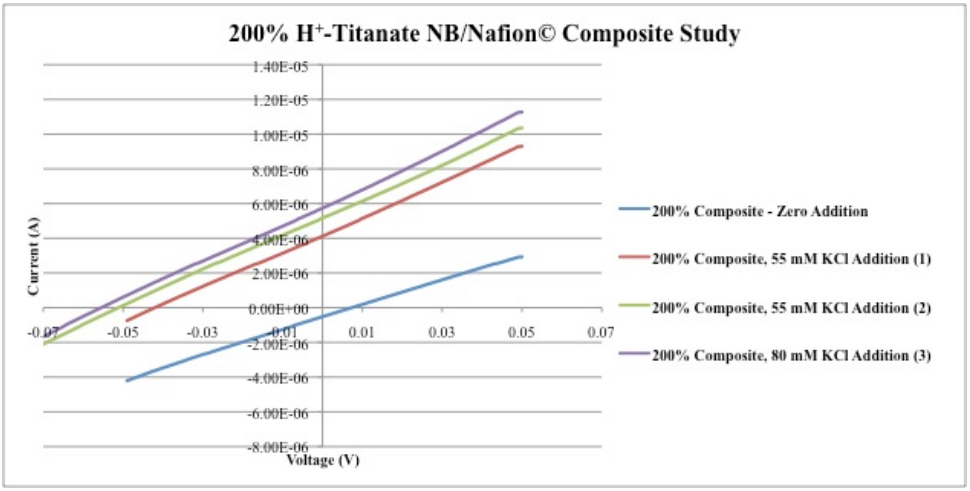

Figure 3.50: Ion Conductivity of [200:1] High-content Titanate NBs/Nafion© Blended Composite Membranes

Addition	Transmembrane Voltage (mV)
Zero	4
1st Addition, 55 mM KCl	42
2nd Addition, 55 mM KCl	50
3rd Addition, 80 mM KCl	55

Table 3.16:Transmembrane Voltage Data of [200:1] H^+-Titanate NB/Nafion© Blended Composite Membranes

3.4.4. Nafion© Blended with High-content Titanate NBs Composite Membranes:

Hydration Management in a Harsh Hydrothermal Environment

The similarities of the ionic conductivity data suggests the hydration level within the composite matrix is similar to that of the pure cast Nafion© formation. To examine this phenomenon more closely, the water uptake of all membranes were studied, the results of which are in table 3.17.

Titanate NB/Nafion© Composites	$WU_{(\%}$ std dev)
Cast Pure Nafion©	32.75 ± 0.66
50:50	37.07 ± 0.96
100:1	8.67 ± 0.67
150:1	13.80 ± 0.95
200:1	23.97 ± 0.55

Table 3.17: Water Uptake ($WU_{(\%)}$) Data for the Titanate NB/Nafion© Blended Composite Membranes

From the water retention results of table 3.16, the 200:1 form and the 50:50 form has the closest hydration management quality to the pure cast Nafion© form. The cast Nafion© form water uptake is very similar to established data from DuPont (Nafion© 117, 38.0%). [149] Further, this data indicates that 50:50 has a similar hydration retention to the 117 form which is currently being examined.

The cast Nafion© and all composite H^+-intercalated titanate NB membrane forms were analyzed using TGA. The results follow in figure 3.51 (A1) through (D2). Figure (A1) through (C1) shows the raw data form and comparison with the pure cast Nafion© form. The true comparison of the TGA analysis between the composite and pure cast Nafion© form is shown in figure 3.51 (D1) and (D2).

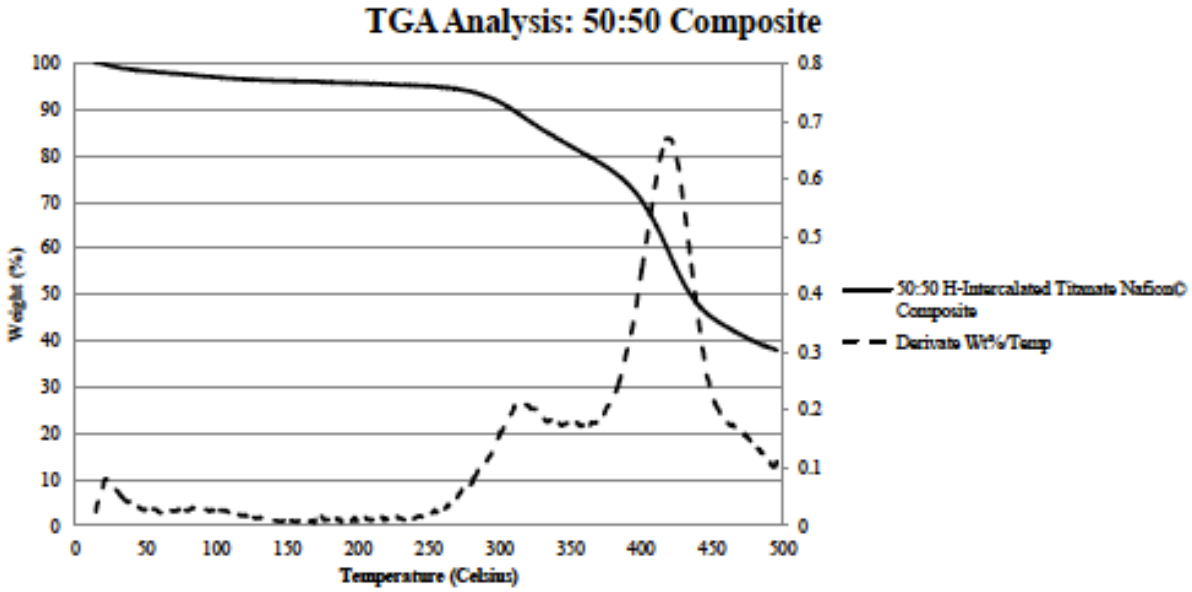

Figure 3.51 (A1): TGA Analysis of H^+-Intercalated Titanate NB/Nafion© [50:50] Blended Composite Membrane

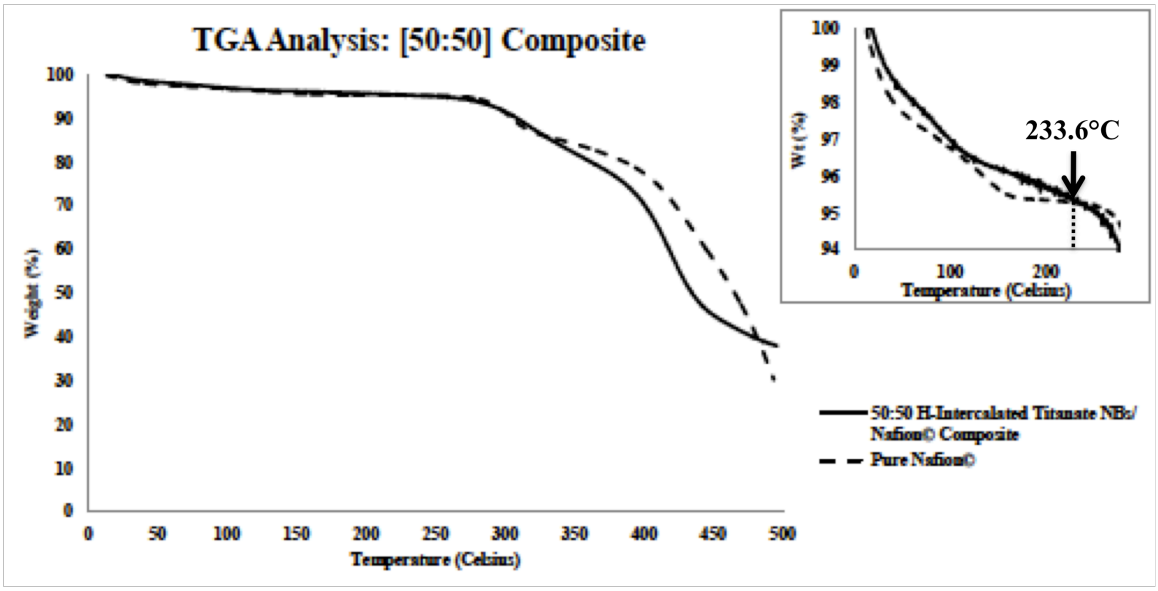

Figure 3.51 (A2): TGA Data for Two Different Cast Composite Membranes

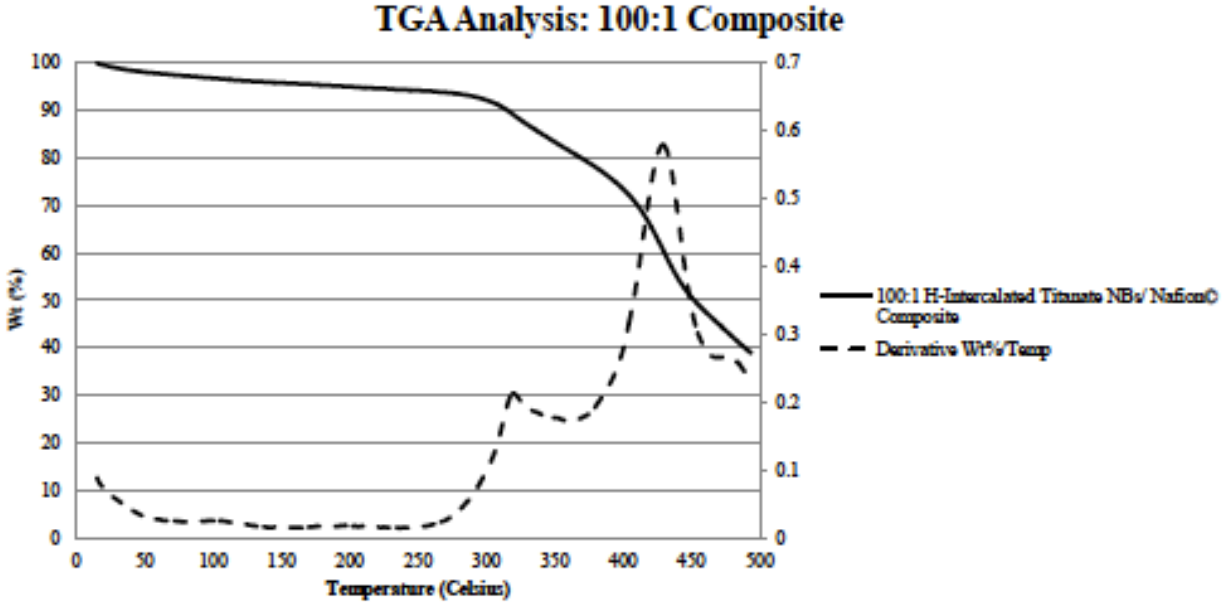

Figure 3.51 (B1): TGA Data of the H^+-Intercalated Titanate NB/Nafion© [100:1] Blended Composite Membrane

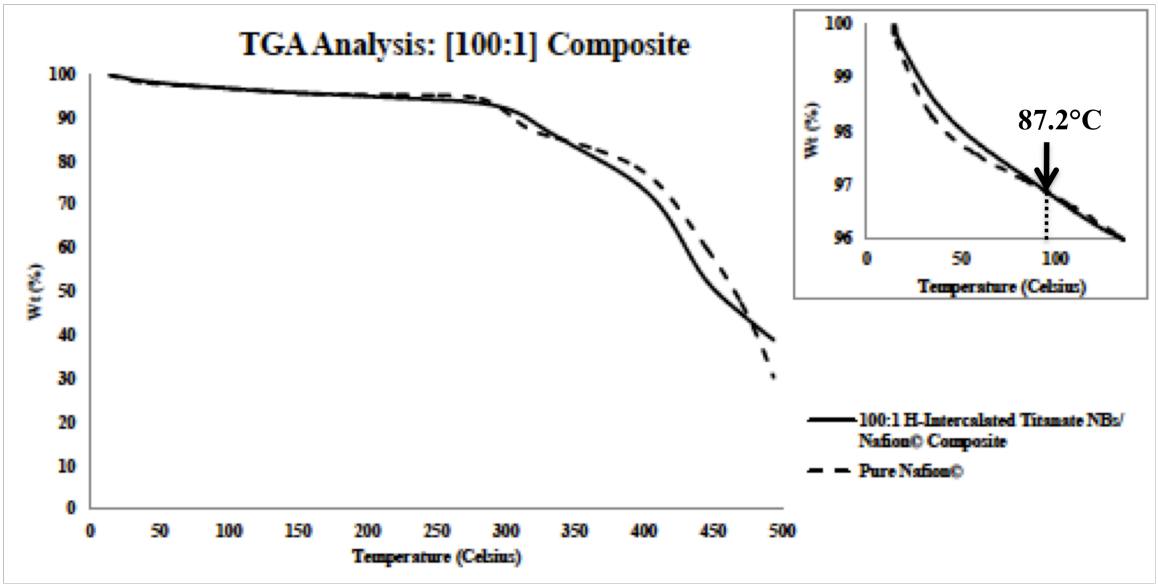

Figure 3.51 (B2): TGA Data for Two Different Cast Composite Membranes

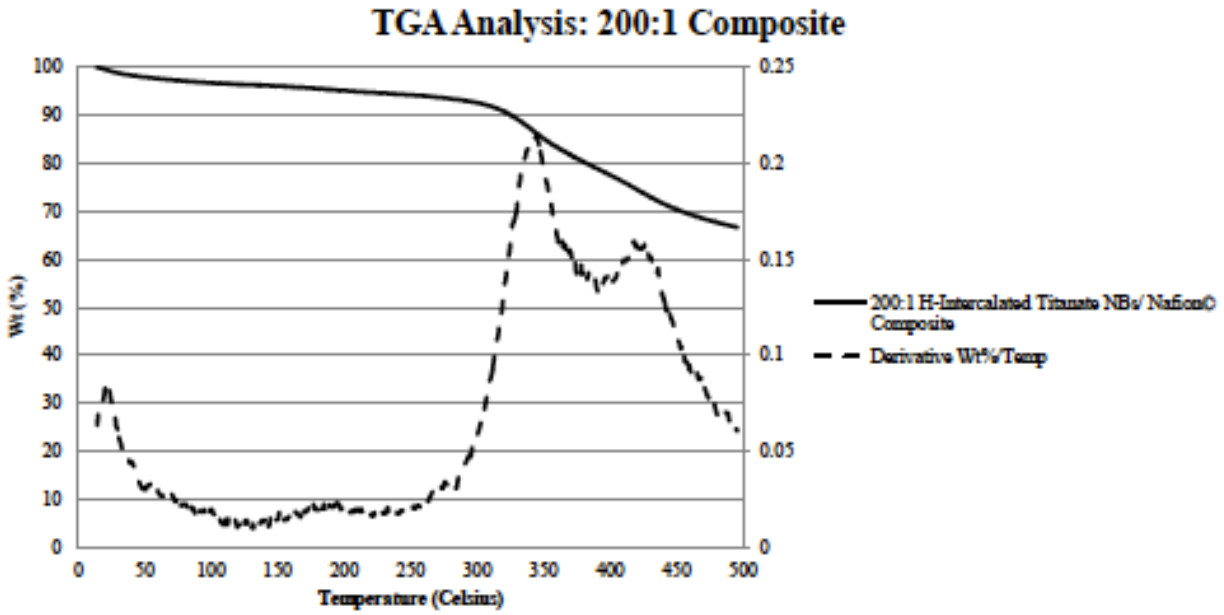

Figure 3.51 (C1): TGA Data of the H^+-Intercalated Titanate NB/Nafion© [100:1] Blended Composite Membrane

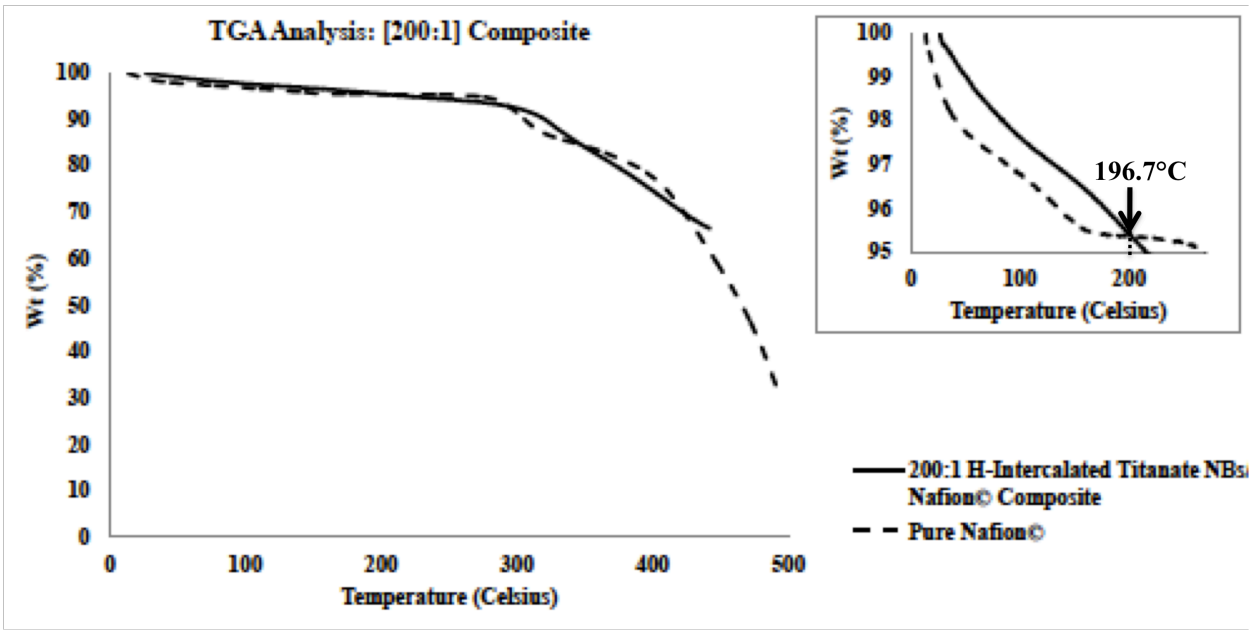

Figure 3.51 (C2): TGA Data for Two Different Cast Composite Membranes

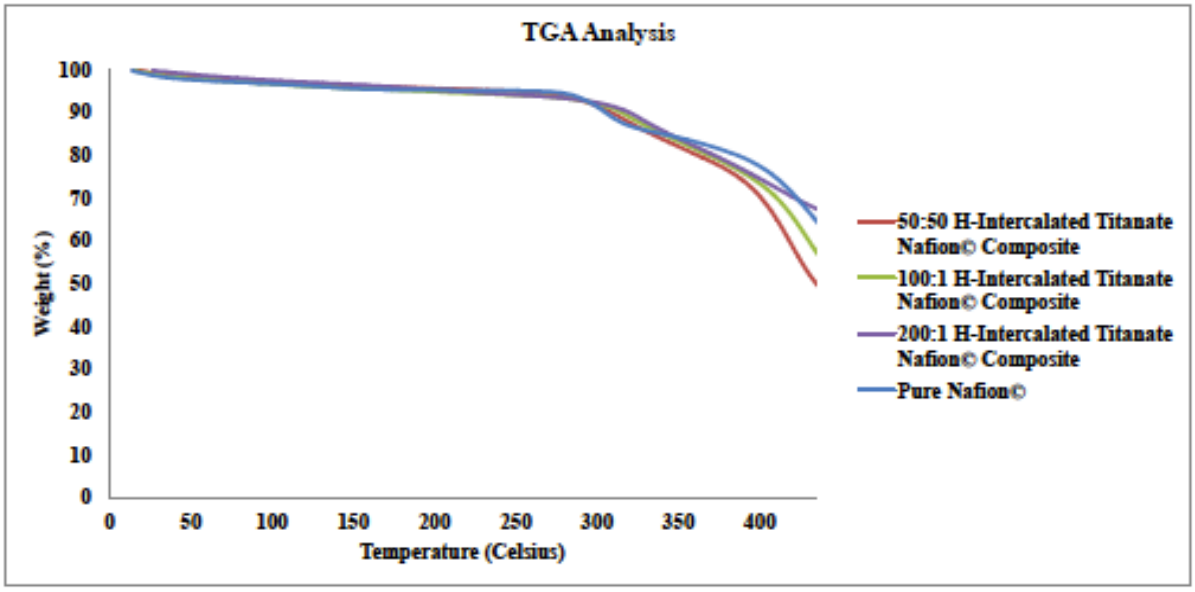

Figure 3.51 (D1): Cast Pure Nafion© vs [Total] H^+- Intercalated Titanate NB/Nafion© Blended Composite Membrane TGA Overview Comparison

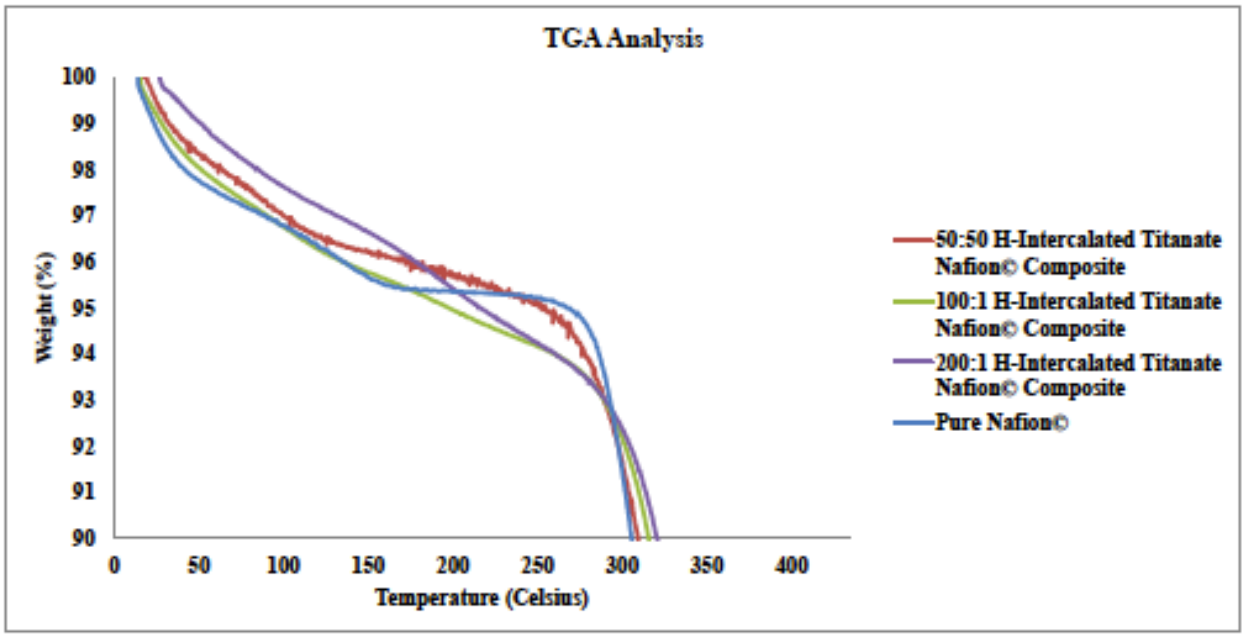

Figure 3.51 (D2): Cast Pure Nafion© vs [Total] H^+-Intercalated Titanate NB/Nafion© Blended Composite Membrane TGA Condensed Comparison

As discussed previously in section 3.4.4., the hydration management up to 150°C (first mass loss) is what identifies the quality of the membrane for use in the PEMFC. Retention and stability of the water molecules within the Nafion© matrix up to that thermal limit would allow for a greater fuel cell efficiency.[150, 151] The higher mass percentages are likely due to similarities previously discussed in section 3.4.4; however, the 100:1 doesn't follow the trending pattern. This is likely due to insufficient balance of interaction between the low concentration of sulfonic groups present and filler material.

Up to the third mass loss, the ranking of the observed data in figure 3.51 agrees with the water retention data previously presented in table 3.17, in which the 50:50 and 200:1 has the higher water intake values when compared the pure Nafion© cast. After the third mass loss of greater than 300°C, the system returns to similar conditions as the pure Nafion© cast form. Overall, the water retention management of the composite forms possesses advantageous property that requires further investigation.

3.5. Titanate NB Membranes: A Relative Humidity (RH) Sensory Material

All trials were assessed for impedance using seven levels of relative humidity starting from 12% to 100%, using saturated solutions already published.[146, 147] Utilizing the interdigitated (IDE) probe preparation outlined section 2.7, each relative humidity (12%, 33%, 50%, 75%, 81%, 92%, 100%) [146, 147] was tested, to determine if the prepared IDE could find a similar ranking of impedance within the given testing parameters.

3.5.1. A Confidence Study on the RH Probe

In order to ensure that the differences observed during the previous eight trials were from the drop coated intercalated material and not from the eight probes created, another experimental trial was performed. The best probe was first selected from the eight probes created. This probe would be tested having no coating ("blank") and having a different coating ("new coat") from that which was previously tested on the probe.

In the "blank" experiment, the probe was first cleaned thoroughly using the following technique: first it is submerged in distilled water, sonicated for 10 minutes, then submerged in acetone, sonicated for 10 minutes, allowed to dry at room temperature for 30 minutes, and finally dried in an 80°C oven for 30 minutes.

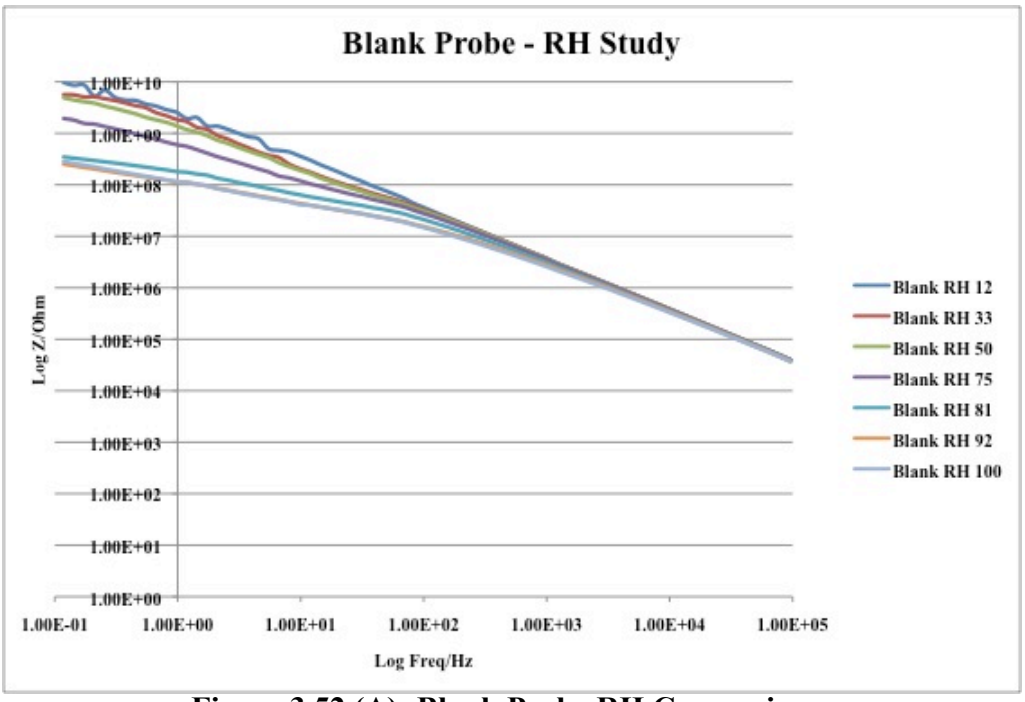

Figure 3.52 (A): Blank Probe RH Comparison

The blank was then run in each relative humidity chamber, the results of which are shown in figure 3.52. Interestingly, when compared to the results of the original proton-intercalated titanate NB deposited probe in figure 3.53 (A), it seems that the nanomaterials push the sensitivity of the probe at higher levels of relative humidity.

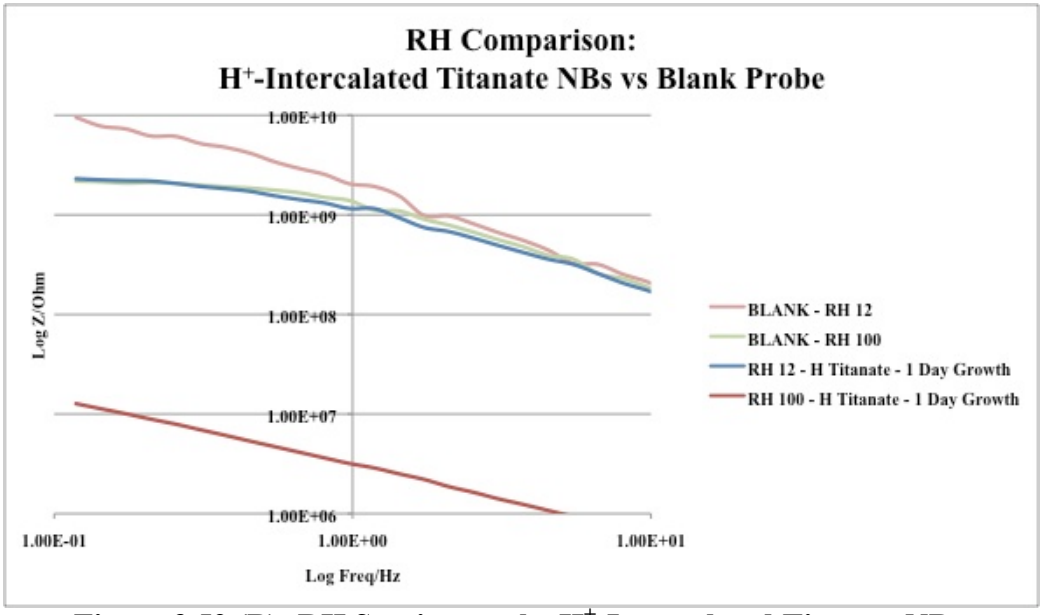

Figure 3.52 (B): RH Sensing on the H^+-Intercalated Titanate NBs

3.5.2. RH Sensing on Titanate NBs Intercalated with Eight Different Cations

As indicated in figures 3.53 (A) through 3.53 (K), all intercalated forms of titanate used in probe fabrication demonstrate a copious reaction to different levels of humidity as demonstrated by the Bode plots (variation of the logarithm of impedance with the logarithm of frequency).

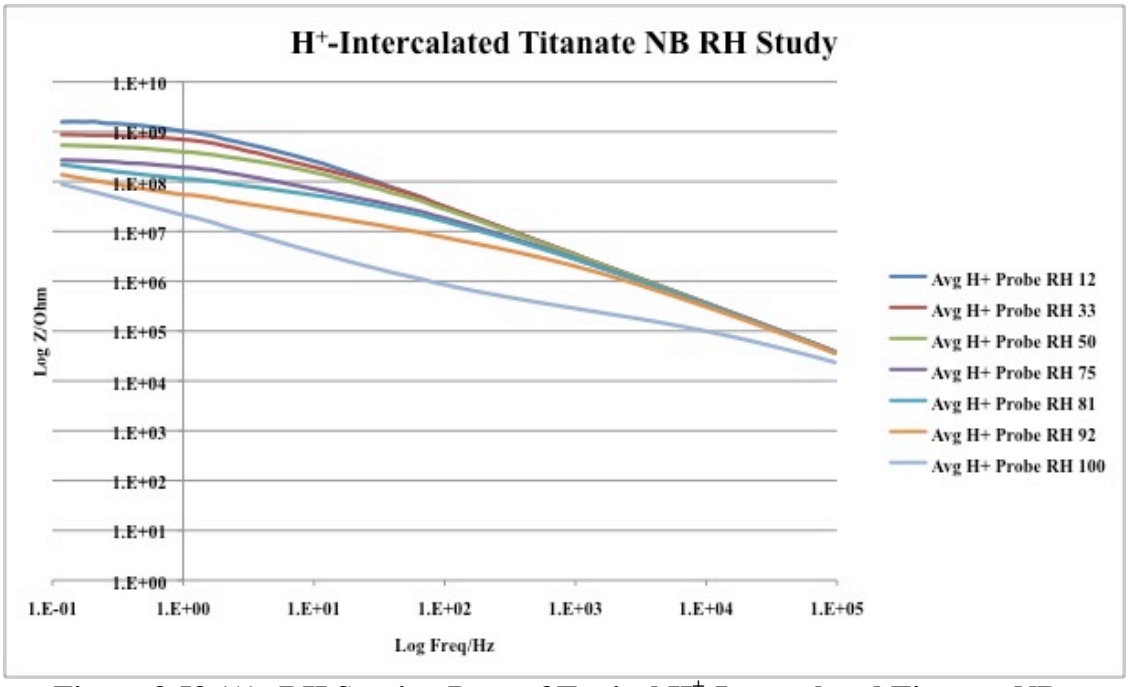

Figure 3.53 (A): RH Sensing Data of Typical H^+-Intercalated Titanate NBs

In Figure 3.53, the proton intercalated titanate NBs probe shows a generous sensitivity to humidity change at low frequency levels. For proton-intercalated titanate NBs, the impedance spectrum can be modeled with an equivalent circuit consisting of a parallel combination of resistor and capacitor. It is observed that the increasing relative humidity levels result in a decrease of impedance at low frequency values.

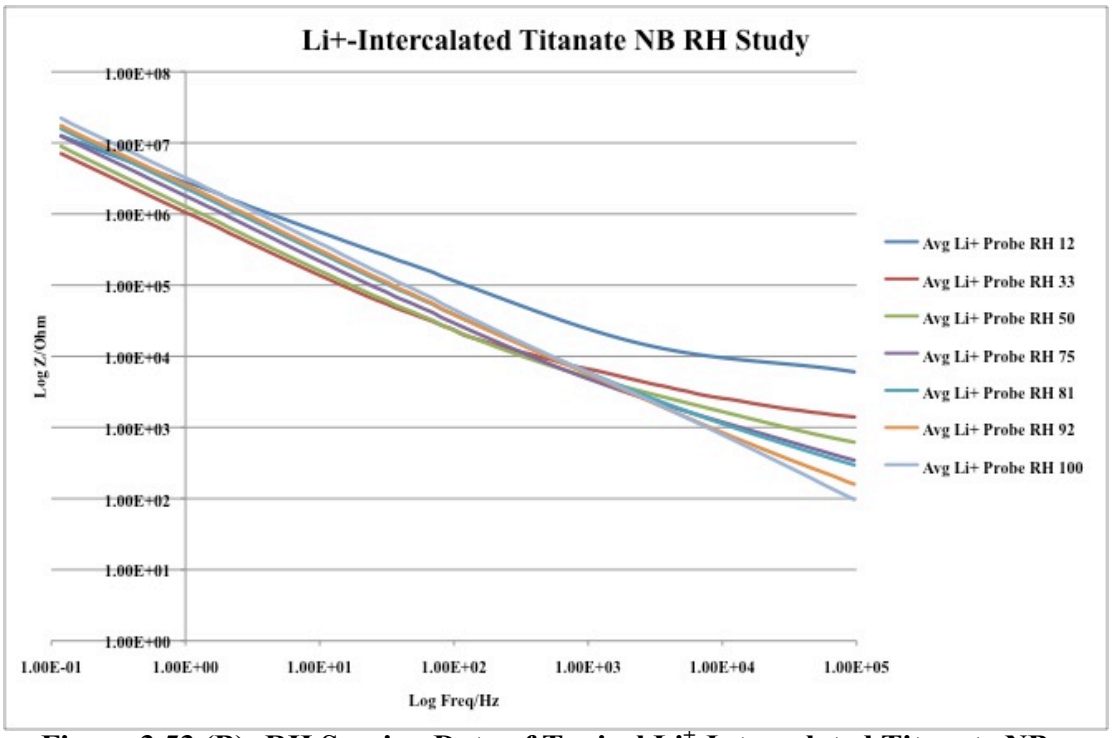

Figure 3.53 (B): RH Sensing Data of Typical Li^+-Intercalated Titanate NBs

However, in the case of lithium intercalation results in figure 3.53 (B), this progression is more dramatic at levels of higher frequency. Thus for titanate NBs intercalated with other ions it is observed that increasing relative humidity values lead to a decrease of impedance at the high frequency end of the impedance spectrum. This can be modeled using an equivalent circuit possessing a resistor and capacitor in a series orientation.

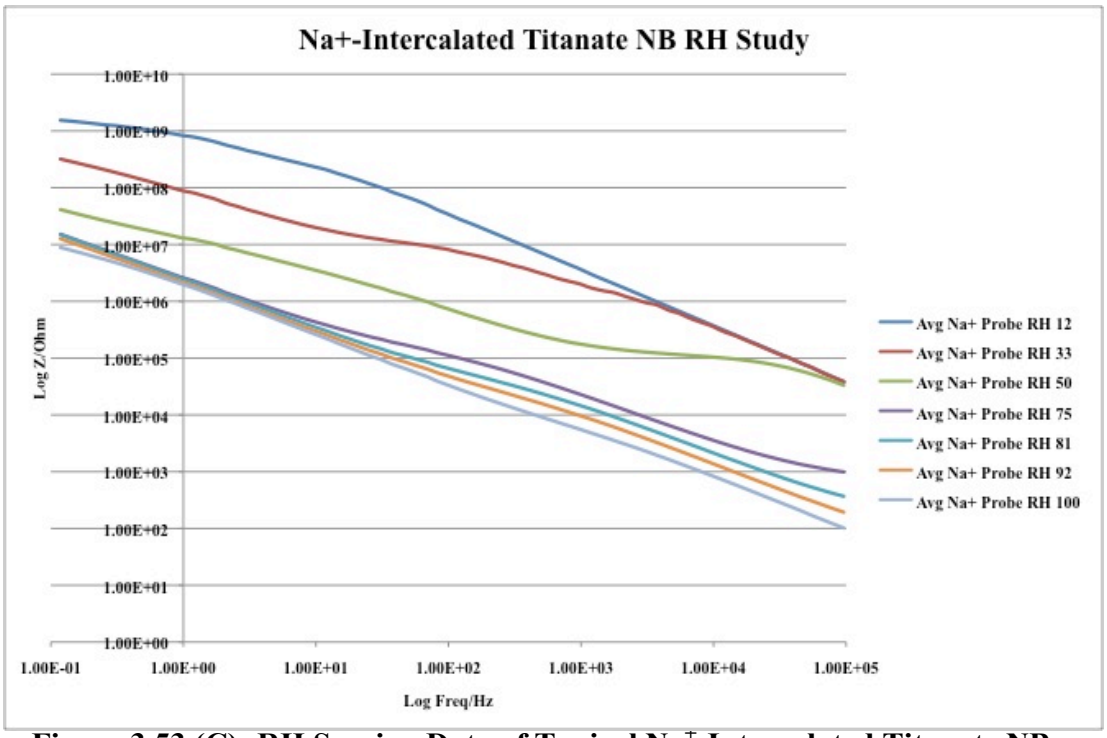

Figure 3.53 (C): RH Sensing Data of Typical Na^+-Intercalated Titanate NBs

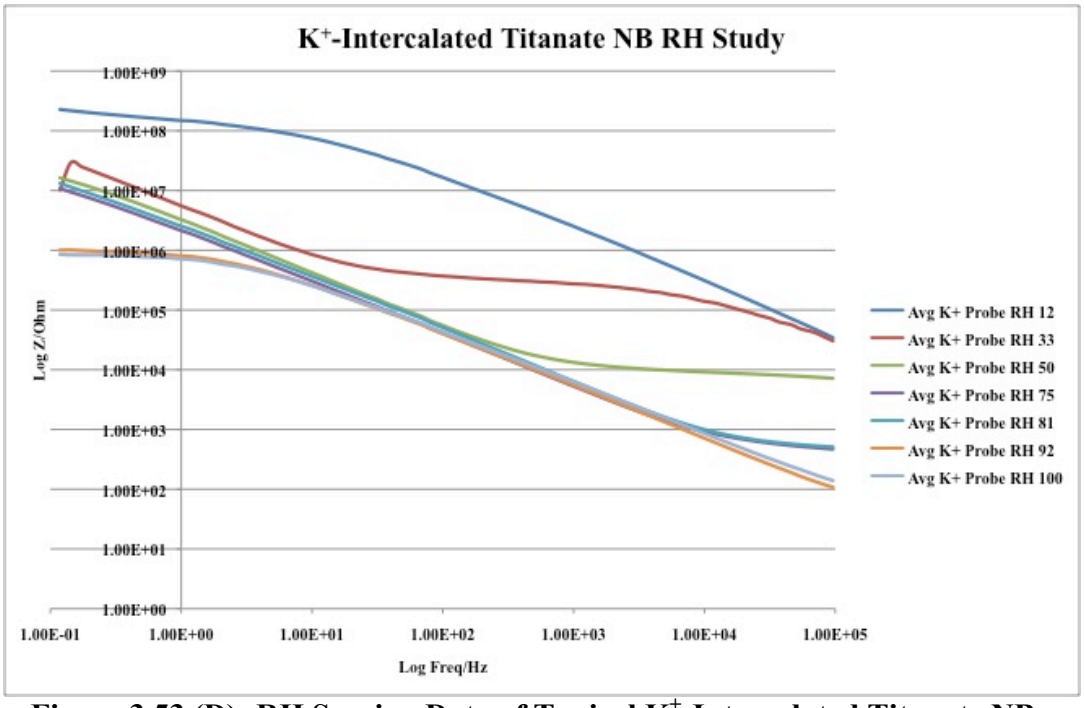

Figure 3.53 (D): RH Sensing Data of Typical K^+-Intercalated Titanate NBs

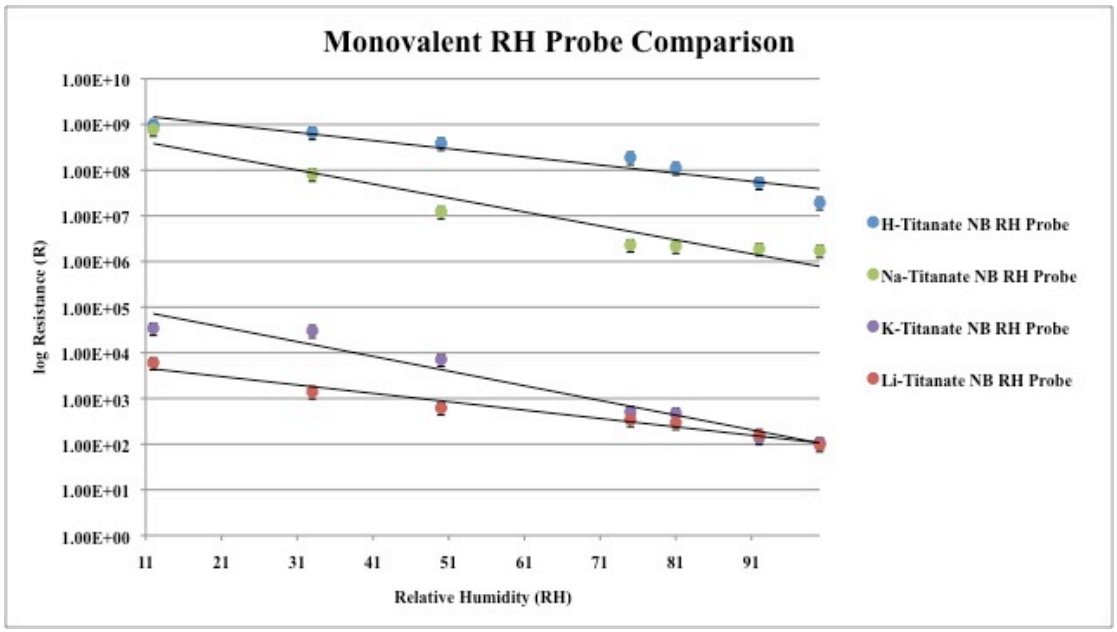

Figure 3.53 (E): RH Sensing on Titanate NBs Intercalated by Monovalent Cations

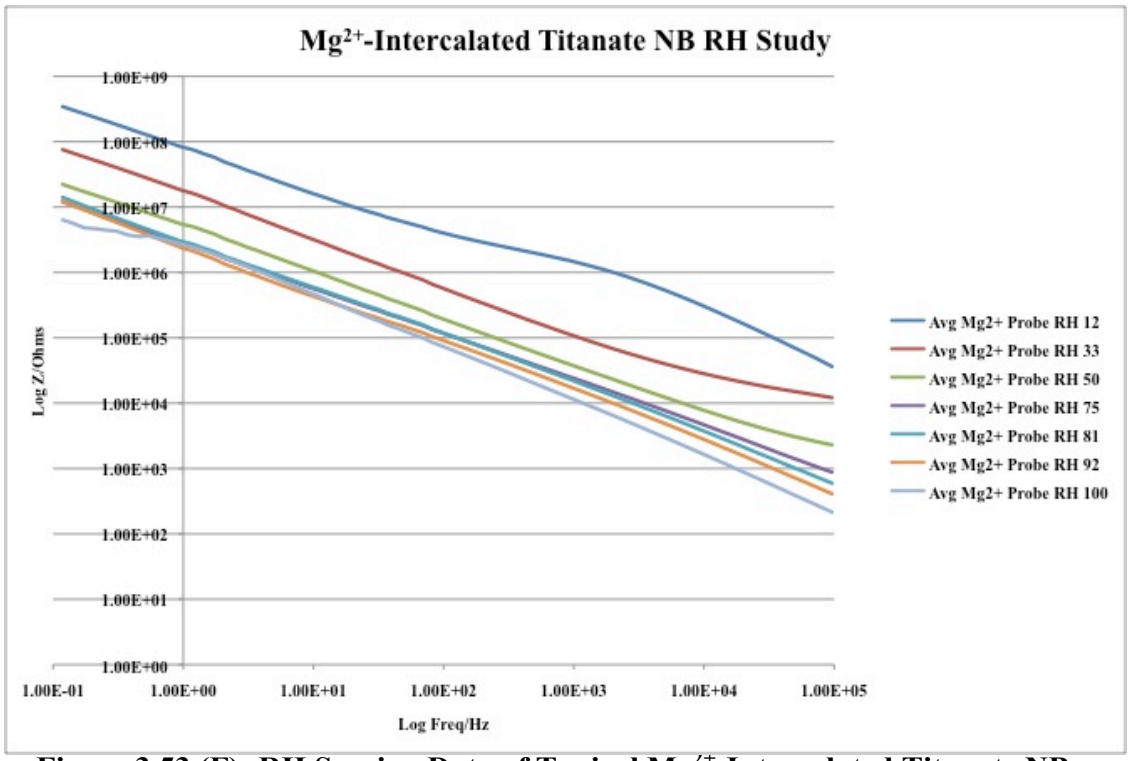

Figure 3.53 (F): RH Sensing Data of Typical Mg^{2+}-Intercalated Titanate NBs

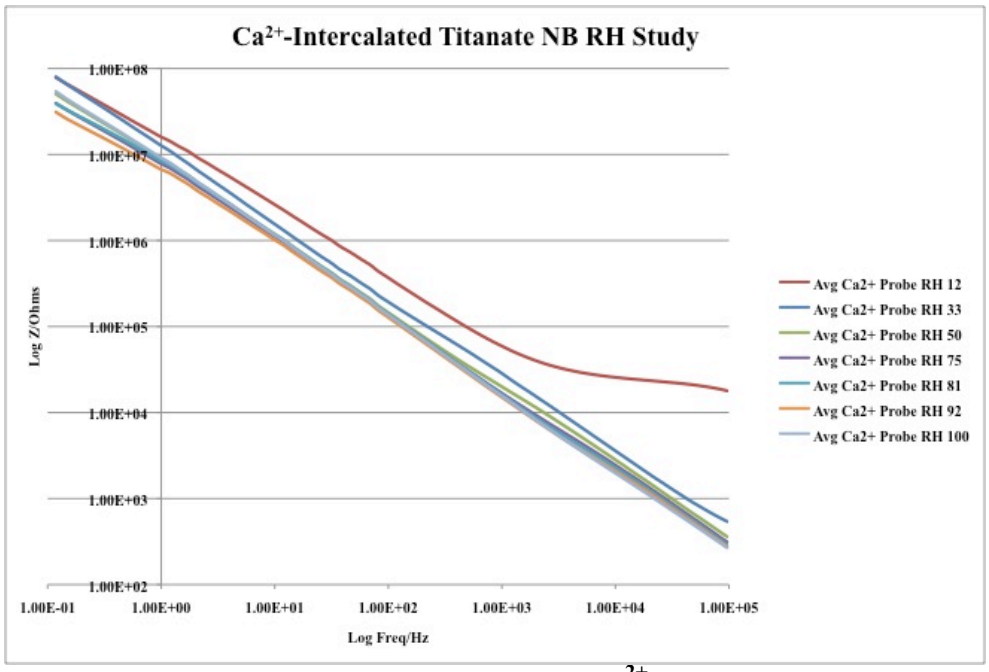

Figure 3.53 (G): RH Sensing Data of Typical Ca^{2+}-Intercalated Titanate NBs

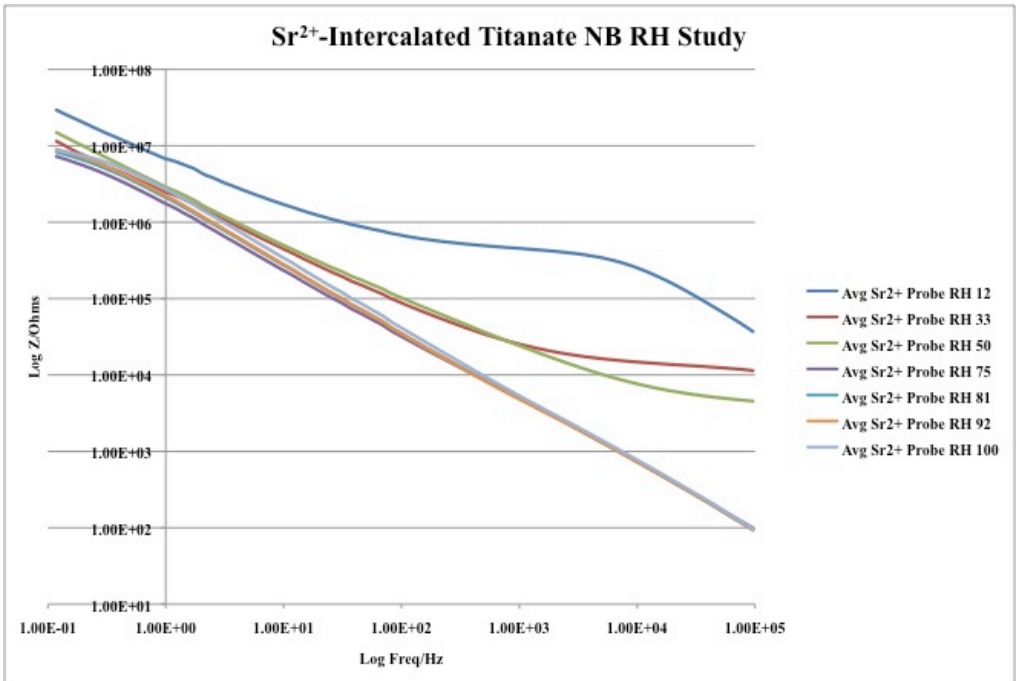

Figure 3.53 (H): RH Sensing Data of Typical Sr^{2+}-Intercalated Titanate NBs

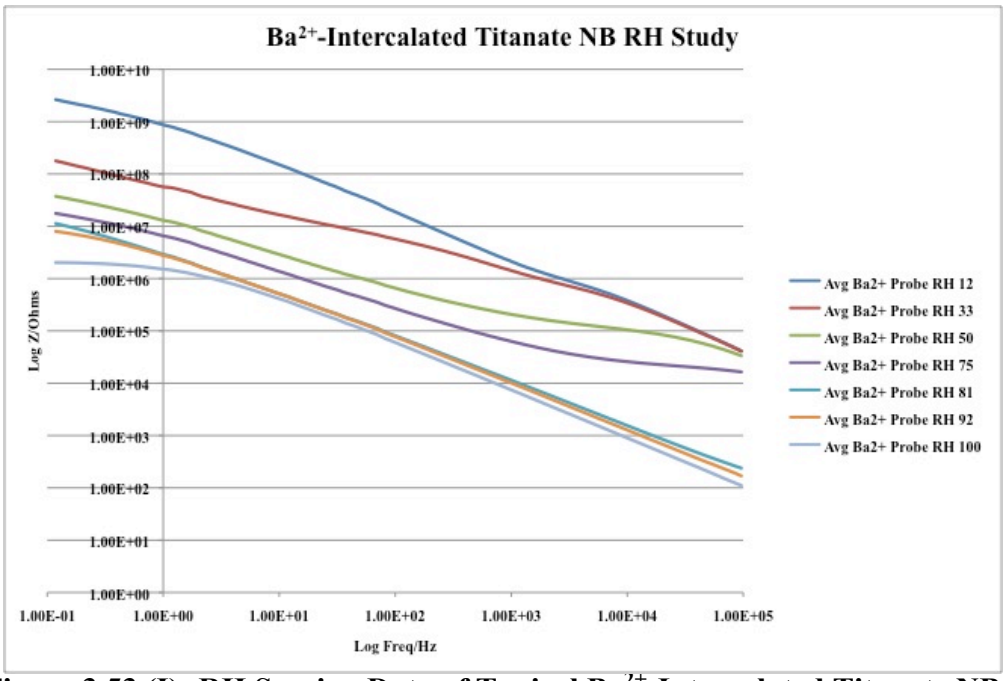

Figure 3.53 (I): RH Sensing Data of Typical Ba^{2+}-Intercalated Titanate NBs

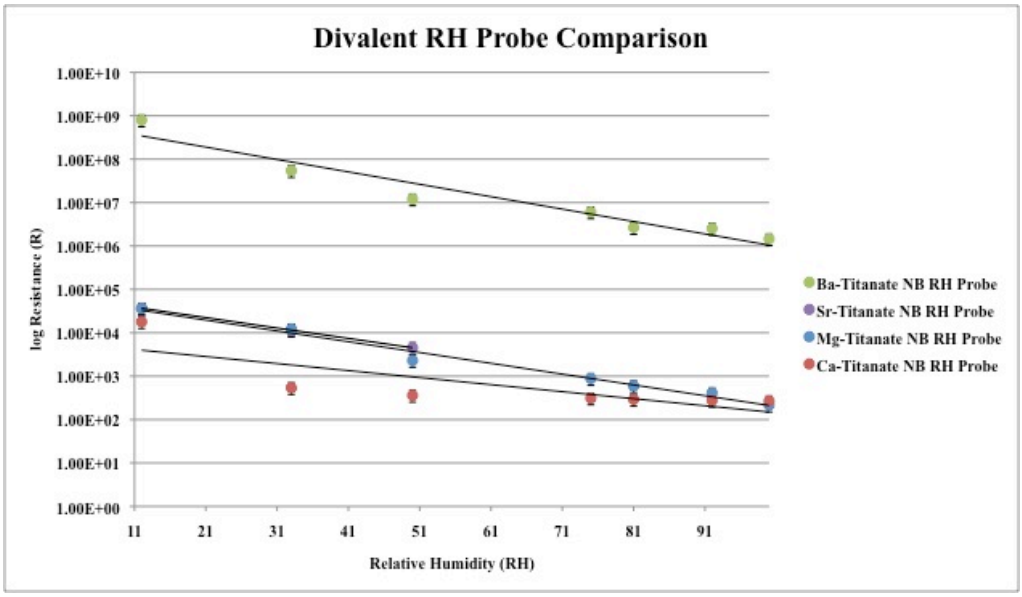

Figure 3.53 (J): RH Sensing on Titanate NBs Intercalated by Divalent Cations

All intercalated forms of titanate used in probe fabrication demonstrate a copious reaction to different levels of humidity. The proton intercalated titanate NBs probe shows a generous

sensitivity to humidity change at low frequency levels, whereas in the case of lithium intercalation results, this progression is more dramatic at levels of higher frequency.

Also except for the proton-intercalated titanate sensor, a considerable amount signal crossover was observed as the trace moves to a lower frequency level depending on the level of RH involved. Meaning the more humidity involved in the test the more pronounced the crossover signal change. Thus far, the RH sensing results indicate that despite the intercalated material being used, a measure of resistance change trends with the relative humidity being tested.

3.6. Summary

1). Our results indicate for the first time in nanomaterials chemistry that the intercalation process plays an important role in alterations of the titanate NB crystal structure, surface active sites and charge conduction, aspect ratios of the NBs, and the quality of the NB-membranes.

2). The room-temperature (RT) aging has been for the first time found to be critical to enabling the abovementioned alterations, which result in new properties, e.g. ion-exchange, thermal stability, surface reactivity and charge conduction, etc.

3). In addition, this RT-aging was found to be able to improve the NB's crystallinity and growing the NB-length, and in turn to expedite the guest cation intercalation and stabilize the intercalated cations, which was seldom discussed in the literature. It must be emphasizes that using the aging process the production of flexible large-scale freestanding titanate NB membranes can now be easily achieved, which is new in materials science in general.

4). Extending the guest load of the aged titanate NBs in Nafion© composites offers similar water management to that of the pure Nafion form, while producing higher transmembrane voltages.

5). Proton, sodium, and barium-intercalated titanate NBs possess high RH sensitivity at low frequency levels. At reduced frequencies, the large separation between signals at specific RH levels allows for ease of detection using these intercalated forms.

CHAPTER 4

RECOMMENED FUTURE WORK

4.1. Intercalated-Titanate NB Further Aging Study

Following the previously described directive, the next intercalation trials will be performed to observe any changes the additional ripening offers to the intercalation of the titanate material. In order to fully understand further ripening methods, the following directive should be taken. The titanate will be immediately processed for intercalation after removal of the autoclave container. After titanate has completed the three-day intercalation, these NBs will be used as a starting material. They will be sealed and undisturbed in a 10M NaOH solution until a designated time (1 day, 1 week, etc). Using this method will confirm or refute whether post-intercalation ripening occurs using these materials. All resulting products will be further characterized throughout the synthesis using XRD, SEM, EDX, and TEM.

4.2. Further Analysis of Intercalated Titanate NB Membranes

Now that all major roadblocks to large-scale titanate NB membrane fabrication have finally been resolved, further ionic transport testing will be accomplished. The fabrication will be completed using the following methodology of a scaled-up procedure of titanate NB membrane with the dimensions of 613.12 cm^2 (5.5 inch X 5.5 inch, 13.97 cm X 13.97 cm sheet).

To facilitate this fabrication, a "modified" Rubbermaid© 9 Cup Easy Find Lid Container having an internal lid depth of 0.25 inches (0.635 cm) was used. Standard coffee filters (100

g/m^2) were used to create the necessary covered area. Nine layers of individual filters were applied one at a time using deionized, distilled water to situate the filter properly to the apparatus surface. Once the apparatus is fully set up, approximately 1.2 g of raw titanate NBs ($Na_{2n-2}H_nTi_3O_7$) will be washed and intercalated in accordance to the directions previously indicated in section 2.5. All resulting products will be further characterized throughout the synthesis and fabrication using XRD, EDX, SEM, TEM, TGA, and ion conductivity.

4.3. Further Nafion©/Titante NB Composite Analysis

First, using all single layer membranes created in the previous section 4.2, laminated titanate NB samples will be fabricated of all eight intercalated titanate samples. Also, using the dried form of the intercalated material, all samples using the mixing method should also be fabricated. Each will be further characterized using the ionic transport chamber discussed in section 2.6.5. in order to ensure each sample facilitates the transport of ions while remaining structurally stable.

Each membrane sample will be further characterized via XRD, SEM, and TEM. Ion-exchange capacity (IEC) and water uptake should also be evaluated. Using IEC, each membrane will be dried and weighed then placed in a 1.0 M NaCl solution at vacuum-dried 80°C overnight to exchange ions. The membranes will then be removed from solution. This solution will be titrated to the phenolphthalein end point with 0.1 NaOH to determine the quantity of exchanged proton ions. Both quantities of IEC and equivalent weight will then be calculated. Using water uptake analysis, each membrane will also be tested via the following method: Each membrane will be dimensionally measured, vacuum dried at 110°C for 4 hours, weighed and dimensionally re-measured. Water uptake measurement will have membrane samples 100% submerged at both

room temperature and 100°C. The membranes will be removed; all droplets will be wiped away, then weighed and re-measured. Finally, the expansion factors (linear = $L_{\%}$ and H_2O adsorbtion = $WU_{\%}$) will be calculated from respective equations.[144]

4.4. Further Study of Intercalated Titanate NB Aging Effects on Gas Sensing Applications

Thus far, the preliminary results indicate that despite the intercalated material being used, a measure of resistance changes trending with the relative humidity being tested. In order to obtain an answer to the mechanism involved, the following experimental plan has been designed. During the preparation of the intercalated species being tested described section 2.5 a daily sample was taken to track the intercalation that progresses (if any). The daily samples will be used in the next trials to observe if cation concentration within the intercalated material plays a role in this mechanism.

Through this investigation, the results could indicate as to whether or not simply ionic presence or ion transport through the titanate NBs is causing the change in the material's resistance. Furthermore, these trials will then be retested utilizing aged intercalated titanate NBs in order to track any and all improvements or deteriorations to the sensor's response or sensitivity level.

Finally, further studies of all sensing properties (selectivity, response, and recovery times) of these probes fabricated using all aforementioned intercalated titanate forms will be investigated against an interfering analyte (ethanol, acetone, etc).

REFERENCES

1. S. Iijima. “Helical microtubules of graphitic carbon” Nature.1991, 354, 56.

2. J. M. Tarascon, M. Armand. “Issues and challenges facing rechargeable lithium batteries” Nature 2001, 414, 359-367.

3. B.O’Regan, M. Grätzel. “A low-cost, high-efficiency solar cell based on dye-sensitized colloidal TiO_2 films ” Nature. 1991, 353, 737-740.

4. A. Fujishima, K. Honda. “Electrochemical photolysis of water at a semiconductor electrode” Nature. 1972, 238, 37-38.

5. X. Gao, Y. Cui, R. M Levenson, L. W K Chung, Shuming Nie “In vivo cancer targeting and imaging with semiconductor quantum dots” Nat. Biotechnal. 2004, 22, 969-976.

6. F. Patolsky, G. Zheng, C. Lieber. “Nanowire sensors for medicine and the life sciences” Nanomedicine. 2006, 1, 51-56.

7. R.J. Chen. “Noncovalent functionalization of carbon nanotubes for highly specific electronic biosensors” Proc. Natl. Acad. Sci. USA 2003, 100, 4984-4989.

8. F. Patolsky, G. Zheng, C. M. Lieber. “Fabrication of silicon nanowire devices for ultrasensitive, label-free, real-time detection of biological and chemical species” Nature Protocols. 2006, 1, 1711-1724.

9. C. R. Martin, “Nanomaterials: A membrane-based synthetic approach” Science. 1994, 266, 1961-1966.

10. C. Vestal and Z. Zhang. “Atom transfer radical polymerization synthesis and magnetic characterization of $MnFe_2O_4$/Polystyrene Core/Shell Nanoparticles” J. Am. Chem. Soc., 2002. 124 (48), 14312-14313.

11. R. A. Andrievski and A.M. Glezer. “Size effects in properties of nanomaterials.” Scripta mater. 2001. 44, 1621-1624.

12. Q. Yuan, H. Duan, L. Li, L. Sun, Y. Zhang, and C. Yan. “Controlled synthesis and assembly of ceria-based nanomaterials.” Journal of Colloid and Interface Science. 2009. 335. 151-167.

13. A. Alivisatos. “Semiconductor clusters, nanocrystals, and quantum dots.” Science. 1996. 271. 933-937.

14. H. Jiang, K. Moon, H. Dong, F. Hua, and C. Wong. “Size-dependent melting properties of tin nanoparticles.” Chemical Physics Letters. 2006. 429. 492-496.

15. G. Glaspell, H. Hassan, A. Elzatahry, L. Fuoco, N. Radwan, and M. El-Shall. “Nanocatalysis on tailored shape supports: Au and Pd nanoparticles supported on MgO nanocubes and ZnO nanobelts.” J. Phys. Chem. B. 2006. 110. 21387-21393.

16. S. Yang, X. Feng, L. Wang, K. Tang, J. Maier, and K. Mullen. “Graphene-based nanosheets with a sandwich structure.” Angew. Chem. Int. Ed. 2010. 49. 4795-4799.

17. J. Son, et al. “Large-scale soft colloidal template synthesis of 1.4 nm thick CdSe nanosheets.” Angew. Chem. Int. Ed. 2009. 48. 6861-6864.

18. W. Ofaff, A. Vos, and R. Hanson. “Top-down fabrication of plasmonic nanostructures for deterministic coupling to single quantum emitters.” 2013. 113. 24310.1-24310.4

19. M. Sadhukham and S. Barman. “Bottom-up fabrication of two-dimensional carbon nitride and highly sensitive electrochemical sensors for mercuric ions.” 2013. 1. 2752-2756.

20. S. Hecht. “Welding, organizing, and planting organic molecules on substrate surfaces-promising approaches towards nanoarchitectonics from the bottom up.” Angew. Chem., Int. Ed. Engl. 2003. 42. 24-26.

21. M. Daniel and D. Astruc. “Gold nanoparticles: assembly, supramolecular chemistry, quantum-size-related properties, and applications toward biology, catalysis, and nanotechnology.” Chem. Rev. 2004. 104. 293-346.

22. C. Park, J. Yoon, and E. Thomas. “Enabling nanotechnology with self assembled block copolymer patterns.” Polymer. 2003. 44, 6725-6760.

23. M. Tello, et al. “Bottom-up fabrication of carbon-rich silicon carbide nanowires by manipulation of nanometer-sized ethanol menisci.” 2005. 17. 1480-1483.

24. G. Whitesides and B. Grzybowski. “Self-assembly at all scales.” Science. 2002. 295, 2418-2421.

25. D. Gracias, J. Tien, T. Breen, C. Hsu, G. Whitesides. “Forming electrical networks in three dimensions by self-assembly.” Science. 2000. 289, 1170-1172.

26. R. Ma, K, Fukuda, T. Sasaki, M. Osada, and Y. Bando. “Structural features of titanate nanotubes/nanobelts revealed by raman, x-ray adsorption fine structure, and electron diffraction characterizations.” The Journal of Physical Chemistry. 2005. 109, 6210-6214.

27. A. Kiebele and G. Gruner, “Carbon nanotube based battery architecture” App. Phys. Lett. 2007, 91, 144104.

28. B.O'Regan, M. Grätzel. "A low-cost, high-efficiency solar cell based on dye-sensitized colloidal TiO_2 films " Nature. 1991, 353, 737-740.

29. A. Fujishima, K. Honda. "Electrochemical photolysis of water at a semiconductor electrode" Nature. 1972, 238, 37-38.

30. X. Gao, Y. Cui, R. M Levenson, L. W K Chung, Shuming Nie "In vivo cancer targeting and imaging with semiconductor quantum dots" Nat. Biotechnal. 2004, 22, 969-976.

31. F. Patolsky, G. Zheng, C. Lieber. "Nanowire sensors for medicine and the life sciences" Nanomedicine. 2006, 1, 51-56.

32. R.J. Chen. "Noncovalent functionalization of carbon nanotubes for highly specific electronic biosensors" Proc. Natl. Acad. Sci. USA 2003, 100, 4984-4989.

33. F. Patolsky, G. Zheng, C. M. Lieber. "Fabrication of silicon nanowire devices for ultrasensitive, label-free, real-time detection of biological and chemical species" Nature Protocols. 2006, 1, 1711-1724.

34. A. Magrez, S. Kasas, V. Salicio, N. Pasquier, J. W. Seo, M. Celio, S. Catsicas, B. Schwaller, and L. Forró. "Cellular toxicity of carbon based nanomaterials." Nanolett. 2006, 6 (6), 1121–1125.

35. A. Huczko, et al. "Pulmonary Toxicity of 1-D Nanocarbon Materials." Fullerenes, Nanotubes, and Carbon Nanostructures. 2005, 13, 141-145

36. P. Chakravarty, et al. "Thermal ablation of tumor cells with antibody-functionalized single-walled carbon nanotubes." PNAS. 2008, 105, 8697–8702.

37. H. Yang, et al. " High-pressure synthesis of carbon nanotubes with a variety of morphologies." Chemical Physics Letters 2005, 416, 18–21

38. Fujishima, A.and Honda, K. "Electrochemical photolysis of water at a semiconductor electrode." Nature 1972, 238, 37-38.

39. O. Legrini, E. Oliveros, and A. Braun. "Photochemical processes for water treatment." Chem. Rev. 1993. 93, 671-698.

40. Ji, Du, et al. "Hierarchically ordered macro-mesoporous TiO_2 – graphene composite films: improved mass transfer, reduced charge recombination, and their enhanced photocatalytic activities." ACS Nano. 2011. 5, 590-596.

41. J. Dalton, et al. "Photocatalytic oxidation of NO_x gases using TiO_2: a surface spectroscopic approach." Environmental Pollution. 2002. 120. 415-422.

42. H. Xue, et al. "TiO_2 based metal-semiconductor-metal ultraviolet photodetectors." Applied Physics Letters. 2007, 90, 201118-1-201118-3.

43. N. Savage, S. Akbar, P. Dutta. "Titanium dioxide based high temperature carbon monoxide selective sensor." Sensors and Actuators B. 2001, 72, 239-248.

44. D. Zhang, C. Kim, and Y. Kang. "A study on the crystalline structure of sodium titanate nanobelts prepared by the hydrothermal method." 2010, 114, 8294-8301.

45. S. Lim, et al. "Room temperature hydrogen uptake by TiO_2 nanotubes." Inorganic Chemistry. 2005, 44, 4124-4126.

46. A. Nakahira, T. Kubo, and C. Numako. "Formation mechanism of TiO_2-derived titanate nanotubes prepared by the hydrothermal process." Inorganic Chemistry. 2010, 49, 5845-5852.

47. H. Peng, G. Li, and Z. Zhang. "Synthesis of bundle-like structure of titanaia nanotubes." 2005. 59, 1142-1145.

48. T. Kasuga, et al. "Formation of titanium oxide nanotube." Langmuir. 1998, 14, 3160-3163.

49. D. Wang, F. Zhou, Y. Liu, and W. Liu. "Synthesis and characterization of anatase TiO_2 nanotubes with uniform diameter from titanium powder." Materials Letters. 2008, 62, 1819-1822.

50. Q. Chen, G. Du, S. Zhang, and L. Peng. "The structure of trititanate nanotubes." Acta Crystallographica Section B. 2002, 587-593.

51. R. Sui, A. Rizkalla, and P. Charpentier. "Formation of titania nanofibers: a direct sol-gel route in supercritical CO_2." Langmuir. 2005, 21, 6150-6153.

52. S. Lee, et al. "Two-step sol-gel method-based TiO_2 nanoparticles with uniform morphology and size for efficient photo-energy conversion device." 2010, 22, 1958-1965.

53. F. Woudenberg, W. Sager, J. Elshof, and H. Verweij. "Nanostructured barium titanate thin films from nanoparticles obtained by an emulsion precipitation method." Thin Solid Films, 2005, 471, 134-139.

54. X. Wei, et al. "Synthesis of highly dispersed barium titanate nanoparticles by a novel solvothermal method." Journal of the American Ceramic Society. 2008, 91, 315-318.

55. A. Nair, et al. "TiO_2 derived by titanate route from electrospun nanostructures for high-performance dye-sensitized solar cells." Langmuir. 2012, 28, 6202-6206.

56. Y. Kolen'ko, et al. "Hydrothermal synthesis and characterization of nanorods of various titanates and titanium dioxide." J. Phys. Chem. B. 2006, 110, 4030-4038.

57. A. Armstrong, G. Armstrong, J. Canales, and P. Bruce. "TiO_2-B Nanowires" Angewandte Chemie International Ed. 2004, 43, 2286-2288.

58. G. Armstrong, et al. "TiO_2B nanowires as an improved anode material for lithium-ion batteries containing $LiFePO_4$ or $LiNi_{0.5}Mn_{1.5}O_4$ cathodes and a polymer electrolyte." Advanced Materials. 2006, 18, 2597-2600.

59. S. Bela, et al. "Hydrolysis and ion exchange of titania nanoparticles towards large-scale and titanate nanobelts for gas sensing applications." 2010, 43, 035401.

60. A. Armstrong, G. Armstrong, J. Canales, R. Garcia, and P. Bruce. "Lithium-ion intercalation into TiO_2B nanowires." Advanced Materials. 2005. 17, 862-865.

61. J. Zhou, et al. "Electronic structure of TiO_2 nanotube arrays from X-ray absorption near edge structure studies." Journal of Materials Chemistry. 2009. 19, 6804-6809.

62. Y. Zhou, et al. "Lithium insertion into TiO_2 nanotube prepared by the hydrothermal process." Journal of the Electrochemical Society. 2003. 150, 1246-1249.

63. B. Meekins and P. Kamat. "Got TiO_2 nanotubes? Lithium ion intercalation can boost their photoelectrochemical performance." ACS Nano. 2009, 3, 3437-3446.

64. M. Margez, et al. "Cellular toxicity of TiO_2-based nanofilaments." ACS Nano. 2009. 3, 2274-2280.

65. W. Zhou, Z. Yin, Y. Du, et al. "Synthesis of few-layer MoS_2 nanosheet-coated TiO_2 nanobelt heterostructures for enhanced photocatalytic activities." Small. 2013. 9, 140-147.

66. S. Li, X. Chen, D. Tian, et al. "Synthesis and synergistic flocculation of $Na_2Ti_3O_7$ nanoribbons." Materials Research Bulletin. 2012. 47, 3770-3773.

67. L. Huang, T. Liu, J. Zhang, et al. "Hydrothermal synthesis of different TiO_2 nanostructures: structure, growth and gas sensor properties." Journal of Materials Science-Materials in Electronics. 2012. 23, 2024-2029.

68, B. Ahn, et al. "Synthesis and characterization of bioactive sodium titanate nanotube by alkali hydrothermal treatment." Solid State Phenomena. 2007. 124, 1277-1280.

69. H. Dai, Y. Chi, X. Wu, Y. Wang, M. Wei, and G. Chen. "Biocompatible electrochemiluminescent biosensor for choline based on enzyme/titanate nanotubes/chiosan composite modified electrode." Biosensors and Bioelectronics. 2010. 25, 1414-1419.

70. W. Wang, O. Varghese, M. Paulose, and C. Grimes. "A study on the growth and structure of titania nanotubes" J. Mater. Res. 2004, 19, 417 – 422.

71. D. V. Bavykin, J. M. Friedrich, F. C. Walsh. "Protonated titanates and TiO_2 nanostructured materials: synthesis, properties, and applications" Adv. Mater. 2006, 18, 2807-2824.

72. A. Riss, T. Berger, H. Grithe, J. Bemardi, O. Diwaid, E. Knözinger. "Chemical control of photoexcited states in titanate nanostructrures" Nanolett. 2007, 7, 433-438.

73. J. Yang, Z..Jin, X. Wang, W. Li, J. Zhang, S. Zhang, X. Gou, Z. Zhang. "Study on composition, structure and formation process of nanotube $Na_2Ti_2O_4(OH)_2$" Dalton Trans. 2003, 3898-3901.

74. S. Zhang, Q. Chen, L.-M. Peng. "Structure and formation of $H_2Ti_3O_7$ nanotubes in an alkali environment" Phys. Rev. B 2005, 71, 014104.

75. D. V. Bavykin, F. C. Walsh. "Kinetics of alkali metal ion exchange into nanotubular and nanofibrous titanates" J. Phys. Chem. C, 2007, 111, 14644-14651.

76. L. Xue-Fei et al. "Preparation of one-dimensional titanate nanomaterials using different titania sources" Acta Phys. – Chim. Sin. 2011, 27 (8), 1996-2000.

77. U.S. Department of Transportation: Office of Highway Policy – Highway Statistics Series for 2011. www.fhwa.dot.gov/policyinformation/statistics/2011/mv1.cfm

78. U.S. Department of Energy: Energy Efficiency & Renewable Energy Research Division. http://www1.eere.energy.gov/hydrogenandfuelcells/fuelcells/

79. A.J. Appleby, F.R. Foulkes, *Fuel Cell Handbook*, Van Norstand Reinhold, New York, N.Y., 1989. Republished by Krieger Publishing Company, Melborne, FL, 1993

80. M. Marronya, R. Barrerab, S. Quenet, S. Ginocchiob, L. Montelatici, A. Aslanidesa. "Durability study and lifetime prediction of baseline proton exchange membrane fuel cell under severe operating conditions." Journal of Power Sources. 2008, 182, 469–475

81. Y. Li, T. Zhao, W. Yang. "Measurements of water uptake and transport properties in anion-exchange membranes." International Journal of Hydrogen Energy. 2010, 35, 5656-5665.

82. P. Choi, N. Jalani, and R. Datta. "Thermodynamics and proton transport in Nafion© II. Proton diffusion mechanisms and conductivity." Journal of Electrochemical Society. 2005, 152, E123-E130.

83. S. Slade, S. Campbell, T. Ralph, and F. Walsh. "Ionic conductivity of an extruded Nafion© 1100 EW series of membranes." Journal of the Electrochemical Society. 2002, 149, A1556-A1564.

84. M. Williams, E. Begg, L. Bonville, H. Kunz, and J. Fenton. "Characterization of gas diffusion layers for PEMFC." Journal of the Electrochemical Society. 2004. 151, A1173-A1180.

85. P. Zhou and C. Wu. “Numerical study on the compression effect of gas diffusion layer on PEMFC performance.” Journal of Power Sources. 2007. 170, 93-100.

86. J. Gao, J. Liu, et al. “Proton exchange membrane fuel cell working at elevated temperature with ionic liquid as electrolyte.” Int. J. Electrochem. Sci,, 2001, 6, 6115-6122.

87. L. Lage, P. Delgado, and Y. Kawano. “Thermal stability and decomposition of Nafion© membranes with different cations using high-resolution thermogravimetry.” Journal of Thermal Analysis and Calorimetry. 2004, 75. 521-530.

88. J. Hensley, J. Way, S. Dec, and K. Abney. “The effects of thermal annealing on commercial Nafion© membranes.” Journal of Membrane Science. 2007. 298, 190-201.

89. G. Sasikumar, J. Ihm, and H. Ryu. “Optimum Nafion© content in PEM fuel cell electrodes.” Electrochimica Acta. 2004. 50, 601-605.

90. W. Hsu and T. Gierke. “ Ion transport and clustering in Nafion© perfluorinated membranes.” Journal of Membrane Science. 1983. 13, 307-326.

91. T. Gierke, G. Munn, and F. Wilson. “The morphology in Nafion© perfluorinated membrane products, as determined by wide- and small-angle x-ray studies.” Journal of Polymer Science: Polymer Physics Edition. 1981, 19, 1687-1704.

92. D. Spry and M. Fayer. “Proton transfer and proton concentrations in protonated Nafion© fuel cell membranes.” Journal of Physical Chemistry B. 2009, 113, 10210-10221.

93. M. Wilson and S. Gottesfeld. “Thin-film catalyst layers for polymer electrolyte fuel cell electrodes.” Journal of Applied Electrochemistry. 1992, 22, 1-7.

94. P. Costamagna, C. Yang, A. Bocarsly, and S. Srinivasan. “Nafion© 115/zirconium phosphate composite membranes of PEMFCs above 100°C.” Electrochmica Acta. 2002, 47, 1023-1033.

95. P. Antonucci, A. Arico, P. Creti, E. Ramunni, and V. Antonucci. “Investigation of a direct methanol fuel cell based on composite Nafion©-silica electrolyte for high temperature operation.” Solid State Ionics. 1999. 125, 431-437.

96. M. Watanabe, H. Uchida, Y. Seki, M. Emori, and P. Stonehart. “Self-humidifying polymer electrolyte membranes for fuel cells.” Journal of the Electrochemistry Society. 1996, 143, 3847-3852.

97. F. Mura, R. Silva and A. Pozio. “Study on the conductivity of recast Nafion©/montmorillonite and Nafion©/TiO_2 composite membranes.” Electrochemica Acta. 2007. 52, 5824-5228.

98. C. Felice, S. Ye, and D. Qu. “Nafion-montmorillonite nanocomposite membrane for effective reduction of fuel crossover.” Ind. Eng. Chem. Res. 2010. 49, 1514-1519.

99. D. Jung, et al. “Preparation and performance of a Nafion©/montmorillonite nanocomposite membrane for direct methanol fuel cell.” Journal of Power Sources. 2003. 18, 205-211.

100. C. Rhee, H. Kim, H. Chang, and J. Lee. “Nafion©/sulfonated montmorillonite composite: a new concept electrolyte membrane for direct methanol fuel cells.” Chem. Mater. 2005. 17, 1691-1697.

101. C. Beauger, et al. “Nafion©-sepiolite composite membranes for improved proton exchange membrane fuel cell performance.” Journal of Membrane Science. 2013. 130, 167-179.

102. F. Fenandez-Carretero, V. Compan, and E. Riande. “Hybrid ion-exchange membranes for fuel cells and separation processes.” Journal of Power Sources. 2007. 173, 68-76.

103. T. Thampan, N. Jalani, P. Choi, and R. Datta. “Systematic approach to design high temperature composite PEMs.” Journal of the Electrochemical Society. 2005, 152, A316-A325.

104. K. Adjemain, S. Srinivasan, J. Benziger, and A. Bocarsly. “Investigation of PEMFC operation abover 100°C employing perfluorosulfonic acid silicon oxide composite membranes.” Journal of Power Sources. 2002, 109, 356-364.

105. E. Chalkova, M. Pague, M. Fedkin, D. Wesolowski, and S. Lvov. “Nafion©/TiO_2 proton conductive composite membranes for PEMFCs operating at elevated temperature and reduced relative humidity.” Journal of the Electrochemical Society. 2005, 152, A1035-A1040.

106. B. Matos, et al. “Nafion©-titanate nanotube composite membranes for PEMFC operating at high temperature.” Journal of the Electrochemcial Society. 2007. 154, B1358-B1361.

107. R. M. Lequin. “Enzyme Immunoassay (EIA)/Enzyme-Linked Immunosorbent Assay (ELISA)” Clinical Chemistry. 2005. 51:122415–2418.

108. Janta, J. “Twenty Years of Ion-selective Field-effect Transistors” Analyst. 1994. 11: 2275-2278.

109. M. S. Arnold, P. Avouris, Z. L. Wang. “Field-Effect Transistors Based on Single Semiconducting Oxide Nanobelts.” J. Phys. Chem. B 2003. 107: 659-663.

110. E. Comini, G. Faglia, G. Sberveglieri, Z. W. Pan, Z. L. Wang. “Stable and highly sensitive gas sensors based on semiconducting oxide nanobelts.” Appl. Phys. Lett. 2002, 81, 1869-1871.

111. L. L. Fields, J. P. Zheng. “Room-temperature low-power hydrogen sensor based on a single tin dioxide nanobelt.” Appl. Phys. Lett. 2006. 88: 263102-1-263102-3.

112. P. Furjes, et al. “Porous silicon-based humidity sensor with interdigitated electrodes and internal heaters.” Sensors and Actuators B: Chemical. 2003. 95, 140-144

113. Z. Rittersma, A. Splinter, A. Bodecker, and W. Benecke. “A novel surface-micromachined capacitive porous silicon humidity sensor.” Sensors and Actuators B: Chemical. 2000. 68, 210-217.

114. W. Qu and J. Meyer. “A novel thick-film ceramic humidity sensor.” Sensors and Actuators B: Chemical. 1997. 40, 175-182.

115. L. Li, et al. “High-performance capacitive humidity sensor based on silicion nanoporous array.” Thin Solid Films. 2008. 517, 948-951.

116. Q. Huang, D. Zeng, S. Tian, and C. Xie. “Synthesis of defect graphene and its application for room temperature humidity sensing.” Materials Letters. 2012. 83, 76-79.

117. M. Mundlein, et al. “Comparison of transepidermal water loss (TEWL) measurements with two novel sensors based on different sensing principles.” Sensors and Applicators A: Physical. 2008. 142, 67-72.

118. R. Ehret, et al. “Monitoring of cellular behavior by impedance measurements on interdigitated electrode structures.” Biosensors & Bioelectronics. 1997. 12, 29-41.

119. P. Gerwen, et al. “Nanoscaled interdigitated electrode arrays for biochemical sensors.” Sensors and Actuators: B. 1998. 49, 73-80.

120. C. Zhou et al. “Human immunoglobulin adsorption investigated by means of quartz crystal microbalance dissipation, atomic force microscopy, surface acoustic wave, and surface plasmon resonance techniques.” Langmuir. 2004. 20, 5870-5878.

121. M. Kitsara, et al. “Single chip interdigitated electrode capacitive chemical sensor arrays.” Sensors and Actuators B: Chemical. 2007. 127, 186-192.

122. J. MacDonald. Impedance Spectroscopy, Wiley, New York, NY. 1987.

123. R. Ehret, W. Baumann, M. Brischwein, A. Schwinde, and B. Wolf. “On-line control of cellular adhesion with impedance measurements using interdigitated electrode structures.” Medical and Biological Engineering and Computing. 1998. 36, 365-370.

124. M. Varshney, Y. Li, B. Srinivasan, and S. Tung. “Microelectrode-based impedance biosensor in combination with nanoparticles immunoseparation for detection of *Escherichia coli* O157:H7 in food samples.” Sensors and Actuators B: Chemical. 2007, 99-107.

125. G. Fiaccabrino, X. Tang, N. Skinner, N. Rooij, and M. Koudelka-Hep. “Interdigitated microelectrode arrays based on sputter carbon thin-films.” Sensors and Actuators B: Chemical. 1996. 35, 247-254.

126. O. Niwa, M. Morita, and H. Tabei. “Electrochemical behavior of reversible redox species at interdigitated array electrodes with different geometries: consideration of redox cycling and collection efficiency.” Analytical Chemistry. 1990, 62, 447-452.

127. K. Toda, Y. Komatsu, S. Gguni, S. Hashiguchi, and I. Sanemasa. “A planar gas sensor combined with interdigitated array electrodes.” Analytical Sciences. 1999. 15, 87-89.

128. K. Albert, et al. “Cross-reactive chemical sensor arrays.” Chem. Rev. 2000. 100, 2595-2626.

129. H. Kim, Y. Jeong, and K. Chun. “Improvement of the linearity of a capacitive pressure sensor using interdigitated electrode structure.” Sensors and Actuators A: Physical. 1997, 62, 586-590.

130. P. Qi, O. Vermesh, M. Grecu, A. Javey, Q. Wang, and H. Dai. “Toward large arrays of multiplex functionalized carbon nanotube sensors for highly sensitive and selective molecular detection.” Nano Letters. 2002. 3, 347.

131. J. Li, Y. Lu, Q. Ye, M. Cinke, J. Han, and M. Meyyappan. “Carbon nanotube sensors for gas and organic vapor detection.” Nano Letters. 2003. 3, 929-933.

132. J. Li, Y. Lu, Q. Ye, L. Delzeit, and M. Meyyappan. “A gas sensor array using carbon nanotubes and microfabrication technology.” Electrochemical and Solid-State Letters. 2005. 8, H100-H102.

133. C. Lam. “A review of carbon nanotube toxicity and assessment of potential occupational and environmental health risks.” Critical Reviews in Toxicology. 2006. 36, 189-217.

134. O. Varghese and C. Grimes. “Metal oxide nanoarchitectures for environmental sensing.” Journal of Nanoscience and Nanotechnology. 2003. 3, 277-293.

135. E. Traversa. “Ceramic sensors for humidity detection: the state-of-the-art and future developments.” 1995. 23, 135-156.

136. T. Sahm, L. Madler, A. Gurlo, N. Barsan, S. Pratsinis, and U. Weimar. “Flame spray synthesis of tin dioxide nanoparticles for gas sensing.” Sensors and Actuators B: Chemical. 2004. 98, 148-153.

137. Y. Liu, E. Koep, and M. Liu. “A highly sensitive and fast-responding SnO_2 sensor fabricated by combustion chemical vapor deposition.” Chemical Materials. 2005. 17, 3997-4000.

138. E. Comini, et al. “Carbon monoxide response of molybdenum oxide thin films deposited by different techniques.” Sensors and Actuators B: Chemical. 2000. 68, 168-174.

139. M. Carotta, et al. “Array of thick film sensors for atmospheric pollutant monitoring.” Sensors and Actuators B: Chemical. 2000. 68, 1-8.

140. K. Benkstein and S. Semancik. “Mesoporous nanoparticle TiO_2 thin films for conductomertic gas sensing on microhotplate platforms.” Sensors and Actuators B: Chemical. 2006. 113, 445-453.

141. E. Comini. “Metal oxide nano-crystals for gas sensing.” Analytica Chimica Acta. 2006. 568, 28-40.

142. Y. He, X, Liu, R. Wang, and T. Zhang. “An excellent humidity sensor with rapid response based on $BaTiO_3$ nanofiber via electrospinning.” 2011. 9, 1-4.

143. R. Wal. G. Hunter, J. Xu, M. Kulis, G. Berger, and T. Ticich. “Metal-oxide nanostructure and gas sensing performance.” Sensors and Actuators B: Chemical. 2009. 138, 113-119.

144. L. Francioso, A. Taurino, A. Florleo, and P. Siciliano. “TiO_2 nanowires array fabrication and gas sensing properties.” Sensors and Actuators B: Chemical. 2008. 130, 70-76.

145. M. B. Satterfield, et al. “Mechanical Properties of Nafion and Titania/Nafion Composite Membranes for Polymer Electrolyte Membrane Fuel Cells.” Journal of Polymer Science: Part B: Polymer Physics. 2006, 44, 2327–2345.

146. F. Vichi, M. Tejedor-Tejedor, and M. Anderson. “Effect of pore-wall chemistry on proton conductivity in mesoporous titanium dioxide.” Chem. Mater. 2000, 17, 1762-1770.

147. J. Kielland, “Individual activity coefficients of ions in aqueous solutions.” J. Am. Chem. Soc. 59:1675-1678, 1937.

148. D. Lide, *Handbook of Chemistry and Physics*, 81st Edition; CRC Press: New York, 2000.

149. H. Corti, F. Nores-Pondal, and M. Buera. “Low temperataure thermal properties of Nafion 117 membranes in water and methanol-water mixtures.” Journal of Power Sources. 2006. 161, 799-805.

150. S. Tiwari, S. Nema, Y. Agarwal. “Thermolytic degradation behavior of inorganic ion-exchanger incorporated Nafion-117.” Thermochimica Acta. 1998. 317, 175-182.

151. Q. Deng, C. Wilkie, R. Moore, and K. Mauritz. “TGA-FTi.r. investigation of the thermal degradation of Nafion© and Nafion©/[silicon oxide]-based nanocomposites.” Polymer. 1998. 39, 5961-5972.

APPENDIX

CHARACTERIZATION METHODS

A.1. Powder X-Ray Diffraction (XRD): Operational Description[1]

The XRD has become a multipurpose tool in the identification of crystalline compounds. Proper utilization of this equipment allows the user access to a non-destructive process for the classification of crystalline compounds from a unique diffraction pattern. Various types of identification can be translated from that information, such as the ability to distinguish between single/multiple-phase materials, determination of crystal structure, and detection of amorphous materials.

Figure A.1 identifies the schematic diagram of the powder XRD. The system consists of an X-ray tube, focus, aperture diaphragm, sample stage (attached to a goniometer), filters, and detector.

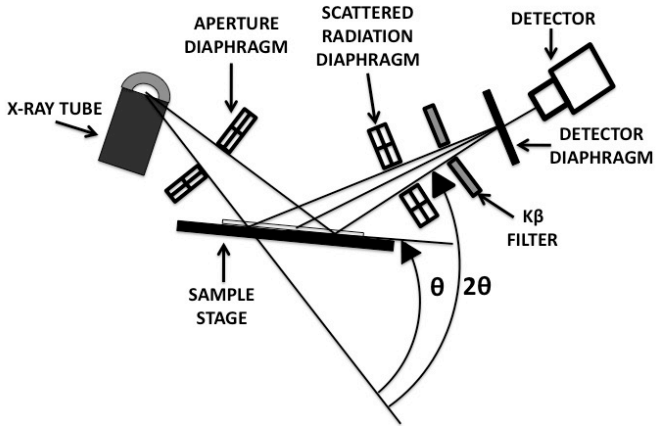

Figure A.1: X-ray Diffraction (XRD) Schematic Diagram

The X-ray tube harbored in the RIGAKUU system is copper (Cu), which is most commonly used for diffraction identification of inorganic materials. The wavelength of the Cu emitted radiation (or Kα) is approximately 1.54Å.

Once the x-ray emitted by the Cu tube becomes monochromatic (due to the aperture diaphragm), the beam strikes the surface of the sample. The θ angle (incident) is defined as that between the incident beam and that of the sample surface; whereas, the 2θ is defined as that angle between the refracted and incident level beams. The series of filters and further apertures on the diffract side is utilized to remove any unnecessary Kα beams. This way the beam becomes further confined to the sample being examined.

Once the angles of diffraction θ and 2θ have been detected interplanar spacing (d) can be measured through use of the "Bragg's Law". The diffracted beams are related to the interplanar spacings of crystalline powders according to the following mathematical relationship.

$$n\lambda = 2d \sin\theta$$

Where n is an integer

λ is the X-ray wavelength

d is the interplanar spacing Y

θ is the diffraction angle (0-180°)

The intensities and angles from the diffraction patterns are collected electronically at the detector on the diffraction side. The d-space (interlayer distance in the crystal) can be calculated using the Bragg mathematical relationship. Further, through use of the standards of the Joint Committee on Powder Diffraction Staanders (JCPDS) and International Center for Diffraction Data (ICDF), the identification of an unknown can be accomplished.

A.2. Scanning Electron Microscope (SEM): Operational Description[2]

The SEM has become one of the most valuable resources to chemists in the field of nanostructures today. The SEM offers multiple superior advancements not available to the optical micrograph. Such as, improved depth-of-field and the greater tolerance limitations of not only on resolution but also magnification (>10,000x).

The SEM is also a very versatile piece of equipment as well. Through coupling of an energy-dispersive x-ray detector (EDX) to an SEM allows the user to collect a cornucopia of other information. For example when the EDX is employed, data from simple topographic/morphologic analysis to crystallographic/compositional information can be quickly accumulated all while focusing on a minute sample area. The SEM block diagram is shown in figure A.2.

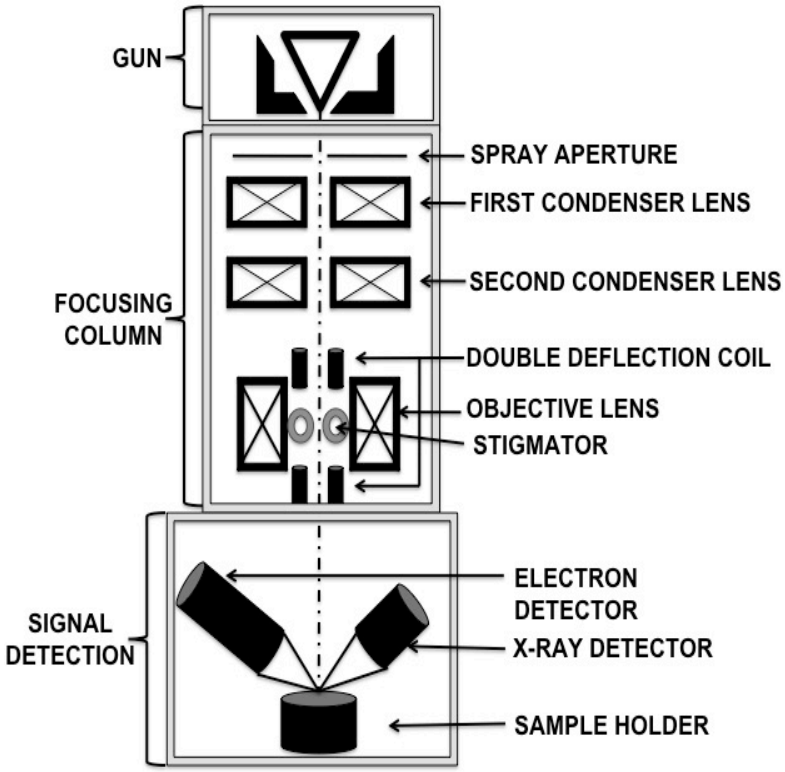

Figure A.2: Scanning Electron Microscope (SEM) Schematic Diagram

The typical SEM possesses three components: electron gun, focusing column, and signal detection. All column components and area containing the specimen are held under the constant control of a vacuum system.

As depicted in figure A.3, the electron gun is consisted of the filament (cathode), Wehnelt electrode, anodic plating, resistors, and a high voltage power supply. Overall, the gun constructs the electron beam through use of a thermionic emission. The electrons are emitted from a cathode made of a thin tungsten wire heated at a high temperature. The electrons are gathered into a beam and flow into a focusing anodic plate. In order to funnel the electron beam down the column the Wehnelt electrode is used. The placement of the Wehnelt electrode between the cathode and anode allows the path of the electrons to transverse each other. This point is called the crossover and is considered the source of the electron gun.

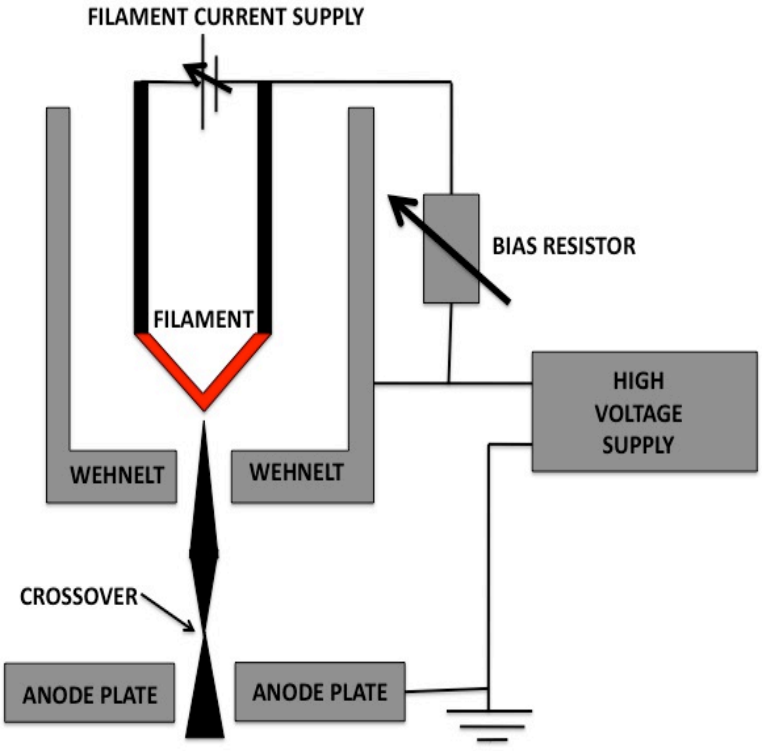

Figure A.3: Electron Gun Schematic Diagram

As the electron beam enters the column it is narrowed further at the spray aperture. The two-stage lens system (condenser and objective) the electron beam is further focused. The condenser lens uses electromagnets to concentrate the beam of electrons into a specific diameter (spot size). In order to for the electron beam to scan the sample surface deflection coils are used. The objective lens is further focused (fine focus) employs the lens current. Stigmators are used to recompense for any matching and column aberrations.

Once the electron beam has struck the sample stage both electron and photons are emitted from the sample surface. The information gathered from the emitted signals is presented in Table A.1.

Emitted Beam Type	Represented Information
X-rays	Thickness Composition
Auger Electrons	Surface Composition
Primary Backscattered Electrons	Atomic Number & Topography
Secondary Electrons	Topography
Cathodoluminescence	Internal Structure Composition

Table A.1: Emitted Beam Breakdown

Once the detector collects the emitted signals, the image can then be processed through computational software.

A.3. Energy-dispersive X-ray Spectroscopy (EDX): Operational Description[3]

The EDX is an optional feature of the SEM. The analytical techniques of the EDX are used primarily for elemental detection. EDX functionality is based upon the interaction between the electron beam and excitation of the sample surface. As discussed previously in SEM (section

A.2), x-rays are one of the emitted signals from the sample once the incident electron beam had struck the sample. These emitted x-rays indicate specific atoms due to each atom's unique structure.

Once the atom interacts with the electron beam the atom may promote an electron from the inner shells through excitation ejecting it creating an electron hole. The difference between the excited shell and the ground state energy may be released from the atom (X-rays). These X-ray signals are detected by the energy-dispersive spectrometer.

Unfortunately, EDX measurements do have analytical limitations. Accuracy of the spectrum may vary between samples. After the focused electron beam, the X-rays are released in all directions. Due to this, many emitted signals may become stymied. Detected X-ray signals depend on the sufficient excitation from the incident electron beam, amount of sample material, and coating density to allow adequate penetration to allow for emission. In order to avoid these issues, rough and non-homogeneous samples should be avoided.

A.4. Transmission Electron Microscopy (TEM): Operational Description[4]

TEM is an invaluable characterization tool for inorganic synthetic chemists. The TEM (like the SEM) allows for the determination of a sample's composition, morphology (shape/size), and crystal structure and defects with high spatial resolution. Even though the microscope may share several functional similarities with the SEM, the TEM has a greater magnification ability to allow it to view at the atomic scale.

The TEM is divided into four operating sections: electron gun, electromagnetic lens system, sample stage, and imaging system. These sections are depicted in figure A.4.

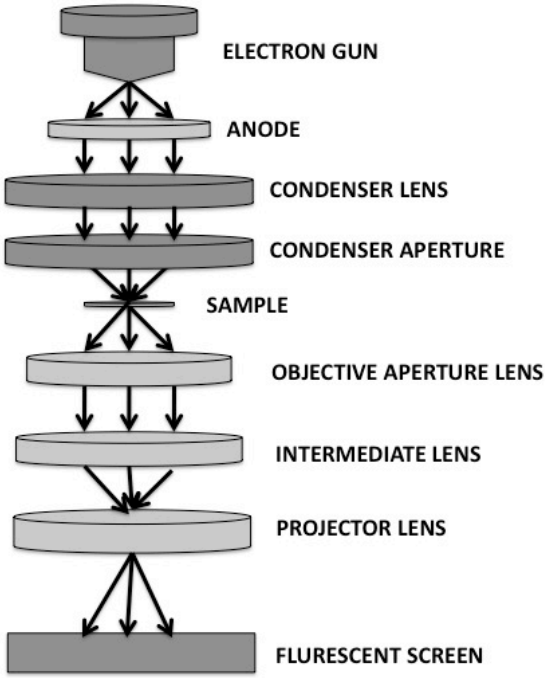

Figure A.4: Transmission Electron Microscope (TEM) Schematic Diagram

The electron gun contains the cathode and the anode. The cathode consists the tungsten filament, which emits an electron stream when a heater current is applied – 6similar to SEM operation previously described in Figure A.3. Afterwards, the beam is further confined by a negatively charged plating system (anode). The anode then accelerates the electron beam down the column.

Once the beam exits the gun, the beam is further focused through a system of electromagnetic lenses and apertures. The condenser lens is used to control the diameter of the electron beam (spot size). The overall purpose of the lens is to condense the amount of electron beam (course adjust). The condenser aperture eliminates high-angle electrons.

After the electron beam passes through the sample, it is collected at the objective system (fine adjust). The objective lens develops a distribution image of electron density. The resulting diffraction pattern is formed from the back focal plane of the objective lens. The aperture

portion of the system improves the contrast of the image. Finally, the image is enlarged using the intermediate and projector.

A.5. Thermogravimetric Analysis (TGA): Operational Description[5]

TGA determines the rate of change in a sample's mass as a function of temperature or time under a controlled atmosphere. Primarily, TGA is used to characterize a material's reactivity due to dehydration, effects of decomposition, and oxidation rating. Also, further quantitative measurements may be used to determine a sample's thermal stability (up to 1,000 °C). The TGA system is depicted in the block diagram in figure A.5.

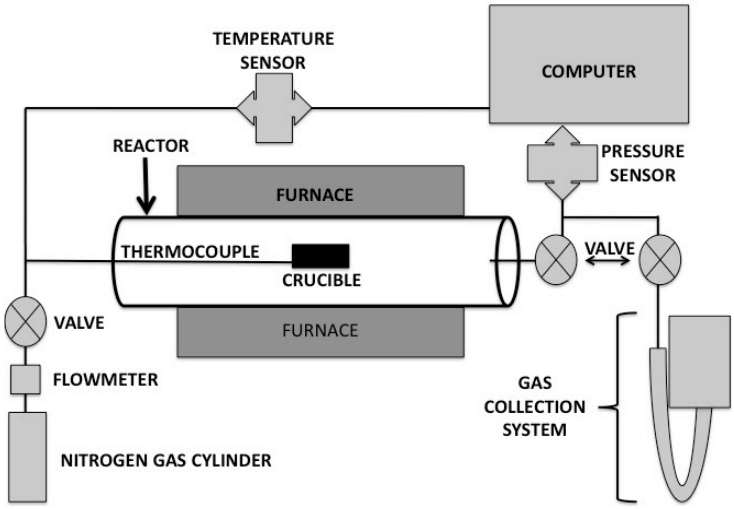

Figure A.5: Thermogravimetry (TGA) Schematic Diagram

The TGA reactor vessel contains a high-precision balance and crucible for the sample. The pan is connected to a thermocouple in which the temperature is strictly controlled through internal programming.

The highly shielded furnace has the ability to generate over 1000˚C. Inert gas (typically nitrogen) is held under specific atmospheric conditions to avoid any unwanted extraneous

oxidations from occurring. The TGA analysis was performed at an initial room temperature to a final temperature of 500 ˚C at a rate of 10 K/min under a nitrogen atmosphere.

A.6. Contact Angle Measurements: Operational Description[6, 7]

Contact angle measurements gauge the degree of hyrdophobicity or hydrophilicity a sample surface has to water. This amount is dictated by the amount a single drop of water is spread over the sample. The examination set up is shown in figure A.6.

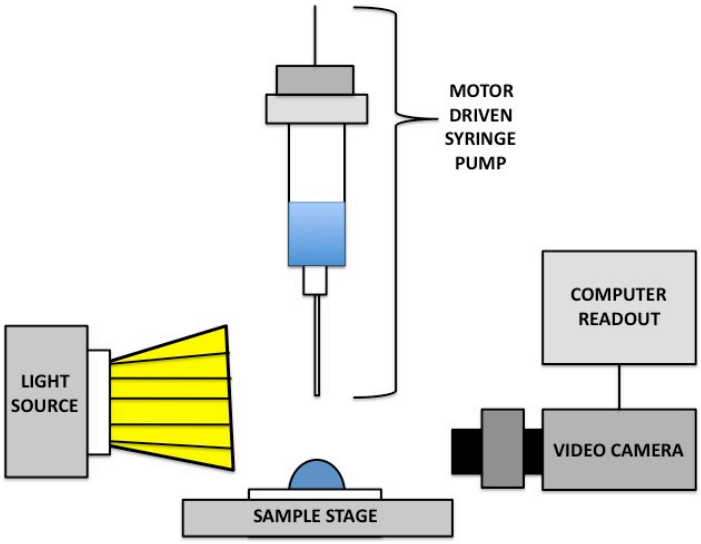

Figure A.6: Contact Angle Ginometer Schematic Diagram

The application of the droplet of water is controlled through a motor driven syringe filled with distilled water via computer software. Throughout the drop placement on the testing surface, the video camera is recording at specified increments dictated by the experimental needs.

Once the experiment is concluded, each water droplet at specific times can be further evaluated. The amount of spread encountered by the droplet allows the researcher to identify the

level of wettability the surface has. The shape of the liquid/solid interface is established by using the Young-Laplace equation in figure A.7:

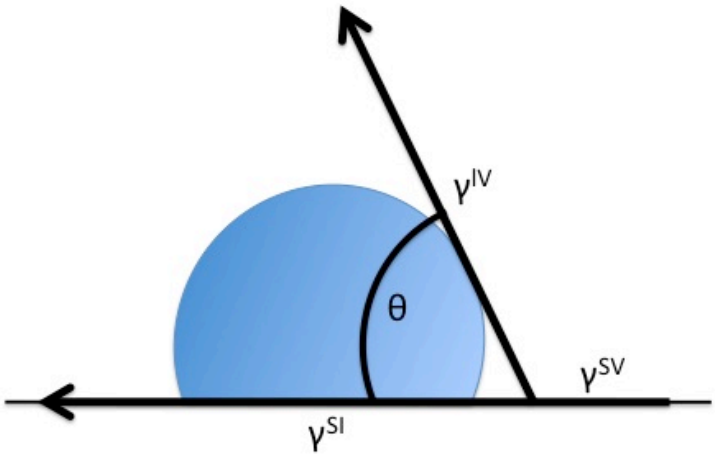

Figure A.7: Contact Angle Measurement of Water Droplet

$$\gamma^{SV} = \gamma^{SI} + \gamma^{IV}$$

Where: γ^{SV} is solid surface free energy

γ^{SI} is solid/liquid free energy

γ^{IV} is liquid surface free energy

Simply stated, the wider the θ angle is indicative of a hydrophobic surface whereas, the inverse depicts a hydrophilic one.

A.7. Electrochemical Methods[8, 9]

A.7.1. Linear Sweep Voltammetry (LSV)

Voltammetry is an important analytical method used in electrochemistry. This type of technique utilizes an electrochemical concentration cell. The experimental cell is shown in figure A.8.

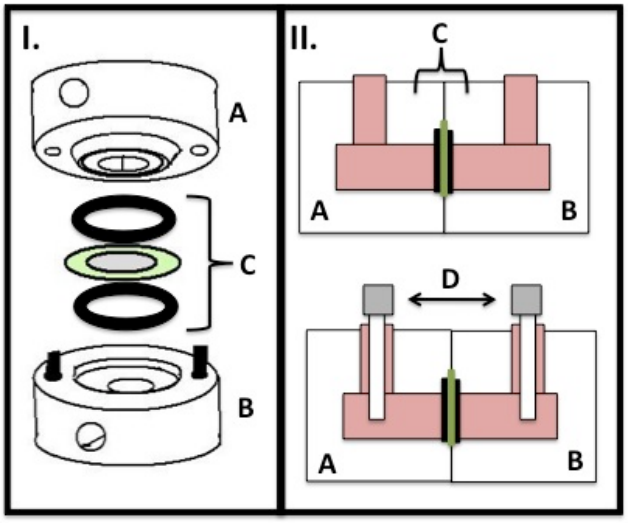

Figure A.8: Ionic Conductivity Chamber

(I.) The cell consists of Teflon outer chambers (A & B), a separation system through a pair of grommets and membrane to allow the transfer of ions (C), and a set of electrodes (D). Typically, the electrodes are placed to enable an interface where a transfer of charge can occur and be measured. (II.) The cell also indicates (in pink shading) that the internal cavity has a known volume.

The reduction/oxidation of a substance occurs on the surface of the working electrode due to an applied potential voltage. The resulting measurements are due to the mass transport of ions within the aqueous environment. In this area of electrochemical techniques, the potential of a working electrode is controlled and the current flowing through electrode is measured. The most common application of this type of technique is linear sweep voltammetry (LSV), which is further investigated.

The LSV typically uses a two-electrode system: working and reference electrode. During the testing the potential (working electrode) is examined linearly with time between two values. Unlike cyclic voltammetry (bidirectional scanning), LSV will exhibit a potential increase during the scan. The concentration cell will direct equilibrium from the higher concentration to the

lower concentration. In doing so, the cathodic current will be produced. Figure A.9 demonstrates a typical potential waveform example.

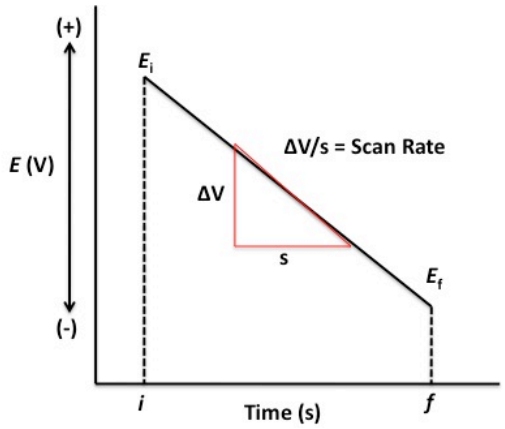

Figure A.9: Excitation Function of Linear Sweep Voltammetry (LSV)

Using this type of cell, the measured potential difference (E) is dictated by the voltage applied (V) and the difference between electrodes (d).

$$\mathbf{E = V/d}$$

In a typical experimental environment, the electrode potential (working) is variable throughout (increasing or decreasing). The current (*i*) is defined as the amount of charge passing through a cross-sectional area (A) in a given time (t).

$$\boldsymbol{i = \Delta A / \Delta t}$$

The level of capacitance (in ohms) current continues throughout.

Within the confines of a concentration cell current density and diffusion factors play a significant role in the electrogenic qualitys of a membrane being examined. Utilizing the first law of diffusion, the number of particles per square centimeter by seconds is expressed as:

$$\mathbf{\#\ of\ particles/cm^2 * s = -D * dc/dx}$$

Where D is the diffusion coefficient

dc/dx is the concentration gradient

The current density (using the first law of diffusion) can be defined as the amount of current generated at that particular cross section. The diffusion will follow in the electric field depending on the charge coupling effect. Using the current density and diffusion together now defines the transmembrane voltage generated in the concentration cell. Through exploitation of the relationship of the Goldman-Hodgkin-Katz (GHK equation) a transmembrane voltage is determined.

$$\mathbf{V_m = V_1 - V_2 = [RT/zF] \ln (C_2/C_1)}$$

Where V_m is the transmembrane voltage

V_1 and V_2 indicate the voltages measured across the given membrane

R is the gas constant

F is Faraday's constant

T is the temperature (Celsius)

C_1 and C_2 indicate the ionic concentrations of both chambers

A.7.2. A/C Impedance Spectroscopy

Electrochemical impedance spectroscopy (EIS) is a standard characterization technique for many applications (batteries, fuel cells, sensors, etc.). EIS is classified as the response of an electrochemical cell to an applied potential energy. In impedance spectroscopy, a sinusoidal wave gauged voltage is directed between designated ranges of frequencies. Due to this type of voltage wave being applied, it is an alternating current (AC) technique.

Using the AC impedance, Ohm's law is observed:

$$\mathbf{V = (i)(Z)}$$

Where, V is applied potential voltage

i is the system's resulting current

Z is the system impedance

The electrochemical station utilized measures the currents and phase angles registered from the applied potential.

From using these AC conditions, the Z can be simply worked out by setting the input voltage potential to a specific level and measuring the resulting current the system generates. The AC probe voltage conditions should be limited so the system response registered a linear correlation. This relationship allows for simple equivalent circuit modeling from the resulting phase angle between the applied potential and the current generated.

The resulting phase angle results can indicate the following correlation: 0° relates to a pure resistor, 1° to 89° is a mixture both resistance and capacitance, and 90° is a pure capacitor. Due to these tolerances between these phase angles, Bode plots are employed. A Bode plot is a plot graphical structure of log of impedance versus a function of log of frequencies. The Bode plot is used to ensure a breakdown of a wide range of frequencies and wide range of impedance gains. This allows the generation of a large amount of data with a smaller viewable area. However, using a different plot structure, Nyquist plots, conveys information to fit the data into an equivalent circuit structure. An example of Nyquist plot is shown in figure 2.10.

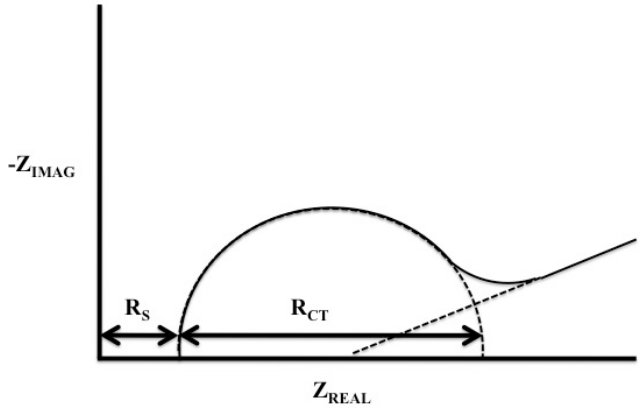

Figure A.10: Nyquist Plot Example Diagram

The graph in figure A.10 illustrates the change in system impedance (Z). R_S results are from the electrolyte resistance, and R_{CT} is due to resistance of the charge transfer. These impedance results are frequently fitted to equivalent circuits of a system of resistors and capacitors.

The most common circuit construction is called the Randles circuit shown in figure A.11. The circuit is broken down using similar characteristics derived from the Nyquist plot , figure A.10, with few additions. Z_W is the impedance from any resulting mass transfer, and C_D is due to double layering capacitance the system undergoes.

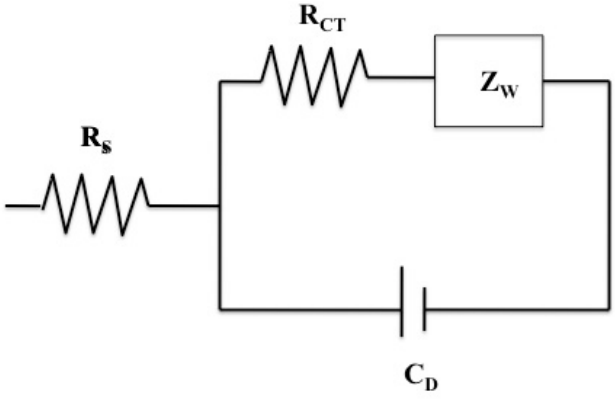

A11: Randles Circuit Example Diagram

APPENDIX REFERENCES

1. H.S. Peiser, H.P. Rooksby, and A.J.C. Wilson, *X-ray Diffraction by Polycrystalline Materials*, Physics in Industry; Reinhold Publishing Corporation, New York, 1960.

2. H. Leamy. "Charge collection scanning electron microscopy." Journal of Applied Physics. 1982. 53, R51-R80.

3. I. Sloufova, B. Vlckova, Z. Bastl, and T. Hasslett. "Bimetallic (Ag)Au nanoparticles prepared by the seed growth method: 2-dimensional assembling, characterization by energy dispersive x-ray analysis, x-ray photoelectron spectroscopy, and surface enhanced Raman spectroscopy, and proposed mechanism of growth." Langmuir. 2004. 20, 3407-3415.

4. D. Williams and C. Carter, *Transmission Electron Microscopy: A Textbook for Materials Science.* Springer Science+Business Media, LLC., New York, 2009.

5. R. Mueller, H. Kammler, K. Wegner, and S. Pratsinis. "OH surface density of SiO_2 and TiO_2 by thermogravimetric analysis." Langmuir. 2003. 19, 160-165.

6. R. Wenzel. "Surface roughness and contact angle." The Journal of Physical Chemistry. 1949. 53, 1466-1467.

7. R. Good and L. Girifalco. "A theory for estimation of surface and interfacial energies. III. Estimation of surface energies of solids from contact angle data." The Journal of Physical Chemistry. 1960. 64, 561-565.

8. J. Macdonald. "Impedance Spectroscopy." Annals of Biomedical Engineering. 1992. 20, 289-305.

9. J. Wang. *Analytical Electrocemistry*, 2nd Edition. John Wiley & Sons, Inc. New York, 2001.